DESIGN AND OPTIMIZATION OF PROTOTYPE TRIP STEEL SMART AIRCRAFT BOLT.

By: Namanyenu Sheleni Mukosa

January 2008

Submitted in fulfilment of academic requirements for the degree of Masters in Science and Engineering in the School of Mechanical Engineering at the University of KwaZulu-Natal

ACKNOWLEDGEMENTS

I would like to express my deepest gratitude to my family, my supervisors Dr Belinda Verijenko and Mr Rob Bodger for the support and encouragement thought this project. In addition, I would like to thank Professor David Jonson, Dr Nirvan K Sookay and Mr Jason Apsey for their assistance.

ABSTRACT

Aviation is known to have some of the most stringent structural health monitoring standards in the world. An example of this would be the fact that certain bolts in the aircraft assembly must be periodically removed and inspected for fatigue damage. This can be a very costly endeavour: a case in point being the Hercules C130 aircraft, which requires approximately 200 man hours of down-time for the inspection of the bolts that attach the wings to the fuselage. The substitution of TRIP (Transformation Induced Plasticity) steel bolts for the current HSLA steel (AISI 4340) from which the bolts are manufactured, allows the bolt to act in the capacity of load bearing member as well as damage detector. This unique feature is a consequence of the transformation characteristic exhibited by TRIP steels when they are strained: an irreversible change within their microstructure from paramagnetic austenite parent phase to permanent ferromagnetic state occurs in direct proportion to the peak strain. This property allows us to establish a relationship from which the service life of the component can be determined. A prototype of a smart aircraft bolt and washer system has been developed, where the bolt acts as damage detector and the washer effectively examines the health of the bolt by reading the changing magnetic susceptibility of the bolt.

This study presents both material development and product development phases of the Smart Aircraft Bolt prototype. A prediction of transformation characteristic due to deformation is carried out using finite element analysis (mechanical model) and a constitutive model (strain-induced martensitic transformation kinetics) to predict the best situation for the smart washer. In addition, experimental work is performed in the form of cyclic temperature testing (with and without external loading) and tension-tension fatigue testing. For both sets of experimental testing, two positions of washer placement are tested. A correlation between volume fraction of martensite present and remaining life, is therefore possible.

TABLE OF CONTENTS

LIST OF FIGURES

Chapter1

Chapter 4

Chapter 5

LIST OF TABLES

Chapter1

Chapter4

INTRODUCTION

The development of a sub scaled prototype TRIP steel (strain memory alloy) smart aircraft bolt, presented in this dissertation, is designed to provide an improved safety inspection time and to address some of the increasingly high costs associated with threaded fasteners used for mounting wings of a C130 cargo plane to its fuselage (at the wing roots). Currently the bolts are manufactured from 4340 high strength low alloy steel, but due to the stringent safety standards of the aviation industry, these must be removed periodically and inspected for damage. At present this process involves jacking the wings up and removing all the bolts for inspection, an operation that takes approximately 200 labour hours. If the bolts could be reliably inspected in situ, this would not only dramatically reduce the amount of time spent on safety inspection, but would also reduce the wear and tear associated with the process of jacking up wings and removing the bolts. A likely candidate for a self-damaging assessing material that fits the mechanical materials property requirements is a high strength Transformation Induced Plasticity (TRIP) steel.

TRIP steels have a unique ability to be utilized as a structural load-bearing component and at the same time as a self-sensing mechanism that returns critical damage data requiring minimal external data capturing equipment. This is achieved through an irreversible transformation that occurs within the material's crystal structure, in proportion to the peak strain experienced by the material. This irreversible transformation can be measured as the change in magnetic susceptibility, since the material transforms from a paramagnetic austenite parent phase to a ferromagnetic martensite phase, producing a correlation back to the peak strain/damage within the material, and thus an indication of remaining component life. The transformation is also responsible for the high values of strain-hardening observed within these steels, which produces little or no necking at the point of fracture.

Substantial work has been done in the field of TRIP steels, and subsequently several components using the smart nature of TRIP steels have been developed, including a smart mining bolt, a bridge load cell, and smart composite laminates, but a smart aircraft bolt poses some unique material requirements both in terms of strength and transformation characteristics. The ultra high strength required by this component means that the material will have to undergo what is known as warm working, which is generally in the range of 450°C to 550°C. This temperature range is below the recrystallisation temperature, but above the temperature at which strain-induced maretensite would form (known as the M_d temperature), meaning that the rolling/extrusion/forging operation increases the dislocation density, thereby increasing yield

strength, but also has the effect of destabilizing the austenite with respect to transformation (making it transform more readily). To achieve an early warning of damage within the bolt material it is vital that the material transforms before the yielding point. In addition, passive sensor design must take into account (at material development stage), a means of interrogating the sensor (in this case the bolt) in situ. The research may therefore be considered to consist of two parts: material development and product development. The material development can only be achieved through an in-depth literature survey to illuminate the effect of alloying chemistry on the material properties and transformation characteristics. Subsequently, candidate alloys can be formulated and destructively tested in tensile, compression and impact modes. Because of the nature of aircraft flight, the temperature range can fluctuate from +40°C down to -50°C in the course of a single flight. The low temperature performance characteristic was therefore also of interest. The results presented in this dissertation from the material developing testing stages and tensile testing of the smart bolt (product development phase) were conducted in conjunction with Dr J M Vugampore [61], hence they are presented from a personal point of view.

Tensile testing formed the first set of testing carried out; this was such because it was important to determine the most important mechanical characteristic: strength - the pre-eminent military specification for threaded fasteners. The magnetic susceptibility was monitored during the same set of testing as this will provided the transformation characteristics of the material with respect to peak strain. Alloys meeting these criteria in terms of strength and transformations were then tested in compression, impact and low temperatures. Hence the best material with the best mechanical and transformation characteristics was deduced in this manner, but this was only the beginning of finding a smart solution for this application, from which the more difficult task of product development commenced.

Product development consisted of several phases, including design of bolt geometry to include the interrogation method: that is, a method of monitoring the strain-induced transformation in situ. At least three possible smart bolt prototypes are proposed and their designs evaluated on the feasibility with respect to meeting the military standards; as well as practical viability, i.e., do the designs perform the duty of early-warning? These evaluations involved physical testing of smart prototypes in fatigue mode as well as cyclic temperature testing and, in addition, modelling of the mechanical response of the material. Smart prototypes were tested in fatigue mode to determine whether the very small amounts of martensite (which will be produced ahead of any crack propagation) can be detected by the interrogation system (also used to evaluate the SMART washer concept). In addition, it was vital to determine whether the interrogation system (evaluation of SMART washer's concepts) could withstand the operation temperature range of the bolts, hence the cyclic temperature testing.

A technique for simulating the mechanical response model and magnetostatic response model is presented in this dissertation by using Finite Element Analysis (FEA) and Finite Element Methods Magnetism (FEMM). This powerful modelling package offered versatility and flexibility in modelling a vast array of complicated geometries and materials definitions. The aim here was to integrate the models generated in FEA and FEMM, to encompass smart prototypes based on the axial loading of the smart aircraft bolt (strain memory alloy). The prediction of martensite nucleation as a function of applied strain was based on previously developed transformation kinetic models that incorporate the mechanical parameters of the smart bolt as a result of volume fraction martensite. Several transformation kinetic models are documented in chapter 3

The technique implemented for simulating the mechanical response model and magnetostatic response models is presented in two parts (most of the work presented in this dissertation makes use of work conducted by Dr David J Jonson [77]). The first part deals with creating a slightly altered 19 mm diameter smart aircraft bolt geometry based on actual bolt geometry, defining the mechanical properties (stress-strain) of the TRIP steel alloy, then simulating where the martensitic nucleation will occur and the quantity of martensite precipitated as a function of applied loading through the use of transformation kinetic models for TRIP steel alloys. Finally the model will be executed as a nonlinear material analysis using the transformation kinetic model for TRIP steels. The output mechanical model from FEA will essentially be used as a base input model for magnetostatic response model (FEMM), the second part of modelling. The base model will then have to be modified in order to integrate the magnetic permeability of the TRIP steel smart bolt material, which will have to be adjusted for each loading increment and for the corresponding calculated amount of martensite precipitated within any point in the smart aircraft bolt. The magnetostatic models will be analysed as simple linear formation.

The results from both the mechanical response model and the magnetostatic will aid in determining the best locating position of martensitic nucleation and finally the best sites for positioning the interrogating system (SMART washers). A comparison test will then be conducted between the results obtained from tensile and fatigue tensile testing and those obtained from the mechanical response model and magnetostatic model in order see if the results are identical to the bolt tensile and fatigue test results.

CHAPTER 1

TRIP Steel as Strain Memory Alloys

1.1 Introduction

Transformation Induced Plasticity (TRIP) alloy steels were originally developed as ultra-high strength steels with better toughness than high strength, low-alloy (HSLA) steels (AISI 4340) generally used for aircraft landing gear and similar applications. TRIP steels display a solid-state, strain dependent phase transformation from a metastable, austenitic (Face-Centred Cubic crystal (F.C.C) structure) parent phase to thermodynamically stable, Body-Centred Cubic (B.C.C) martensitic product phase. TRIP steels are the only class of materials, which have the cited characteristic that can be used (replacing AISI 4340 steel) for the manufacture of smart aircraft bolts. The special characteristics of these materials enable TRIP steels to have a dual function, acting both as a load bearing member as well as having self-damage assessment ability. TRIP steels are also referred to as strain memory alloys. Strain memory alloys measure and memorize the peak strain induced in the material during service, but vary tremendously in composition, strength and material processing. TRIP steels are a class of high strength strain memory alloys that have been warm worked to increase their strength.

The high levels of ductility and strain hardening observed in these steels are due to strain induced phase transformation. An incremental increase in applied strain is directly proportional to strain-induced matensitic nucleation (change in magnetic property of material). The fracture of the tensile specimens displays very little or no necking. The levels of ductility of TRIP steels in comparison to those of high strength steels were much higher and their elongations typically range from 10% to 15% [1-50]. The strain-induced martensitic phase transition phenomenon became the focal point for the research investigation conducted on TRIP steels in the 1970's [15, 39-41, 45, 46, 49, 50]. The early work conducted in this area also focused on the associated changes in mechanical behaviour accompanying the phase transition with regards to ausforming, a thermo-mechanical fabrication process of TRIP steels (that is, metastable austenite was warm-rolled at a temperature above that necessary to cause any strain-induced

phase transformation. This resulted in an increase in the yield strength of the material due to the high dislocation density) [52, 3, 6, 7, 17, and 18].

Apart from the stated structural properties mentioned above, the transformation from an austenitic face-centered cubic (FCC) crystal structure parent phase to a metastable body-centred cubic (BCC) product phase also results in a change in the magnetic properties (one extra characteristic) of the alloy, which provides the foundation for the self-damage assessment of TRIP steels, making them an inherently SMART material class, i.e., strain memory alloy. The magnetic signature of the steel is therefore dependant on the fraction of martensite present, which is proportional to applied strain [2] as shown in Figure 1.1.

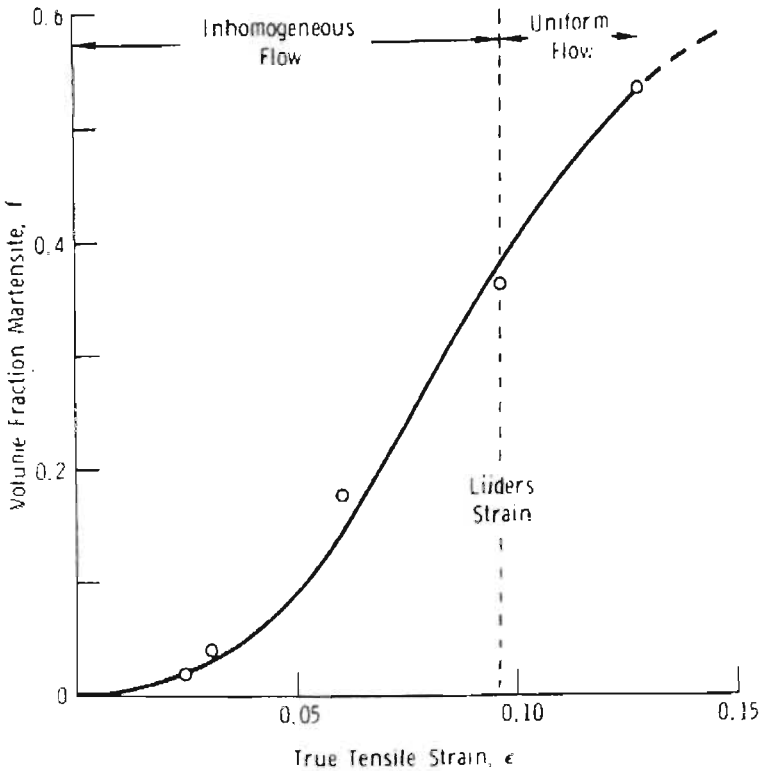

Figure 1.1: Martensite volume fraction vs. applied strain [15, 61]

1.2 Chemistry of the TRIP Steels

The transformation curve and the level of incubation strain which triggers the transformation as well as the mechanical properties of TRIP steels can be tailor-made. The sensor material can be altered to produce the optimised transformation behaviour by adjusting the chemical

composition. For the particular application at hand, the TRIP steels were tailored to operate within a temperature range of -50°C to 50°C as per SPS-B-640 military standard for AC 130 aircraft. The Schaeffer-de Long Diagram, Figure 1.2 and 1.3 displays a visual scenario in which the alteration of the different alloying elements governs which phases will be present in the alloy, that is, whether the alloy will display the matensitic phase or austensitic phase or a combination of ferrite, martensitc and austenite phases. The Schaeffer-de Long diagram is also used to deduce the nickel and chromium equivalents for the desired chemical composition of the SMART aircraft material. This is illustrated in Figures 1.2 and 1.3. The chromium and nickel equivalents are calculated as follows:

$$\text{Chromium equivalent } (C.E) = \%Cr + \%Mo + 1.5\%Si \tag{1}$$

And

$$\text{Nickel equivalent } (N.E) = \%Ni + 30\%C + 0.5\%Mn + \%Co + 25\%N \tag{1.1}$$

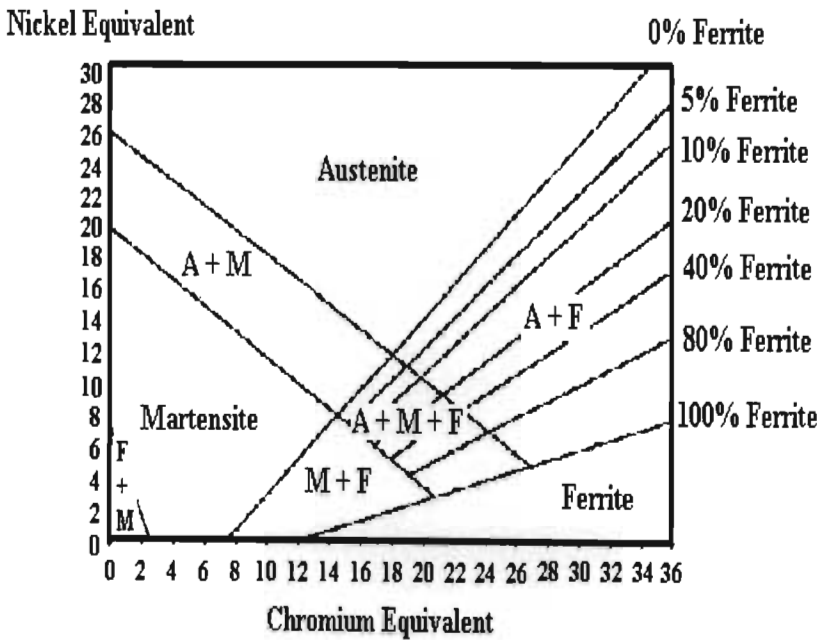

Figure 1.2: **The Schaeffer-de Long diagram used for the prediction of the phase that will be predominant in the alloy [24, 61]**

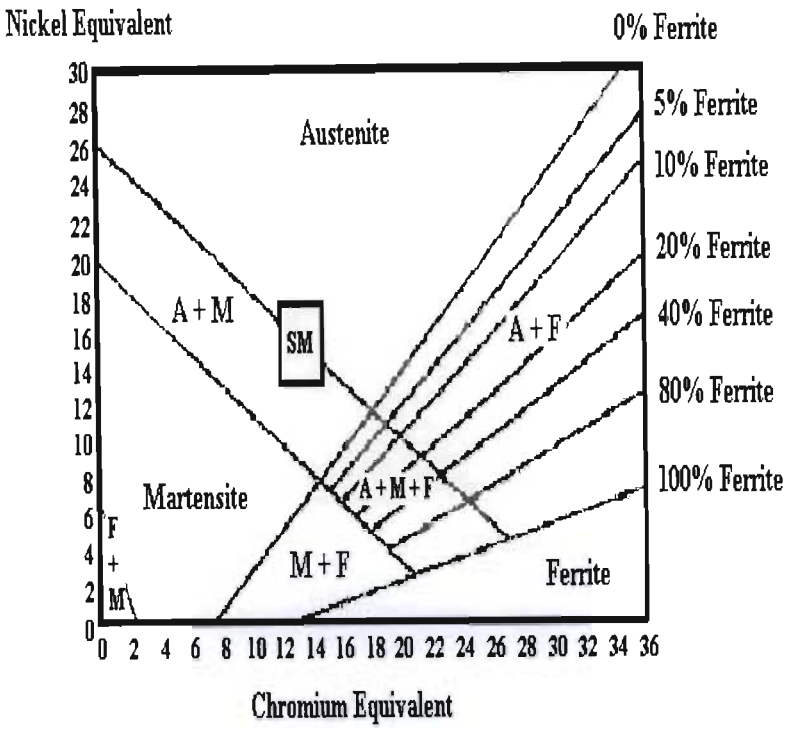

Figure 1.3: Schaeffer-Dde Long diagram shows an approximated region (SM) were TRIP steel or Smart are situated [24, 61]

The alloy elements form the fundamental basis for the stabilisation of the austenite at room temperature. For the application at hand the most frequently utilised alloying elements were Fe, C, Cr, Ni, Mn, Si, N, Mo, and P. Furthermore an equilibrium state of the austenitic stabilizers and ferrite stabilizers must be met in order for the austenite to remain stable at the stated service temperatures. Nevertheless, it should be destabilized by the lattice perturbation and duly precipitate precipitation of martensite [41-42, 61]. Strain memory alloys use an iron matrix as a base material (which is of great importance to the magnetic properties that make the material smart). The influences of every element utilized for the chemical formation of the alloy chemical composition are described in Table 1.1.

Table 1.1: Effects the various alloying elements have on the properties of TRIP steel.

	Promotes	Effect on properties
Cr	Ferrite	Improves general corrosion resistance and resistance to oxidizing environments and lowers the Stacking Fault Energy (SFE)
Ni	Austenite	Improves general corrosion resistance and resistance to reducing environments.
C	Austenite	Increases strength, decreases corrosion resistance.
N	Austenite	Increases strength and pitting resistance, raises SFE.
Mn	Austenite	Improves hot cracking resistance, increases solubility of nitrogen, austenite stabilizer, and lowers SFE.
Mo	Ferrite	Improves pitting and service corrosion resistance, increases work hardening, lowers SFE
Nb	Ferrite	Forms stable carbonitrides to resist sensitization, grain refinement
Si	Ferrite neutral	Improves wetting and flow, improves high temperature oxidation and carburization resistance and improves the stability of austenite at low temperature ranges
Ti	Ferrite	Forms stable carbonitrides to resist sensitization
Al	Ferrite	Improves high temperature oxidation and decarburization resistance
Cu	Austenite (weak)	Improves resistance to reducing environments. and precipitation hardening
S	Neutral	Improves machinability, promotes hot cracking
F	Ferrite	Increases strength, promotes hot cracking

1.3 The Thermo-Mechanical Processing Of TRIP Steels

Generally TRIP steels are cast into ingots under vacuum inert conditions, from which the alloys undergo further processing (hot rolling) to eliminating any casting imperfections. In addition, the alloys are then further processed to increase their yield strength, and/or destabilise their austenitic structure, which makes them more sensitive to strain-induced transformation. Usually steels are strengthened (apart from the strength imparted by the alloying itself) by one of two means: either they are heat treated using the classical γ/α transformation which was not applicable in this case, since the alloys were required to remain austenitic stable at temperatures ranging from 50°C to -50°C; or the material can be cold-worked, thereby increasing the dislocation density which in turn increases the yield strength. This approach is also not

applicable for this class of materials, because cold working entails deformation, which would immediately trigger the strain-induced martensitic transformation and this was highly undesirable in a material for strain monitoring application such as the SMART aircraft bolt. It therefore becomes necessary to look more closely at the transformation characteristics of this particular class of materials, in order to obtain a means of increasing yield strength without actually creating martensite.

Two methods are frequently utilized for improvement of the yield strength of the TRIP steels. These are ausforming [43-44] and cyclic heating treatment [45].

1.3.1 Ausforming

Ausforming is a process which utilizes the metastable bay (on the TTT curve shown in Figure 1.4) in the region of 400°C - 500°C to impact the work without producing any transformation. This "bay" is produced by manipulating all chemistry of the alloy. The TRIP steel chemistry, as noted above consists of several alloying elements required to meet the operating parameters of the SMART aircraft bolt. The TTT diagram illustrates the isothermal transformation as a function of temperature and time dependence. The classic martensitic precipitation takes place due to decreasing temperatures from martensitic start (M_s) temperatures to martensitic finishing temperatures (M_f), which forms the typical γ/α heat treatment. As noted above the γ/α heat treatment was not ideal for SMART material. However, the proximity of M_s-M_f temperature range has inherent effects on the strain-induced martensite nucleation. Strain-induced martensite stops precipitating above a temperature, M_d, which supports martensitic nucleation [24], which must be determined experimentally for a specific chemical composition, which also could be altered for other structural engineering applications [2, 4, 11, 27, 38, 52, 48-49, 56, 61]. Figure 1.4 below shows a TTT curve engineered for a specific chemical composition. It illustrates a bay, within which the material is engineered [43].

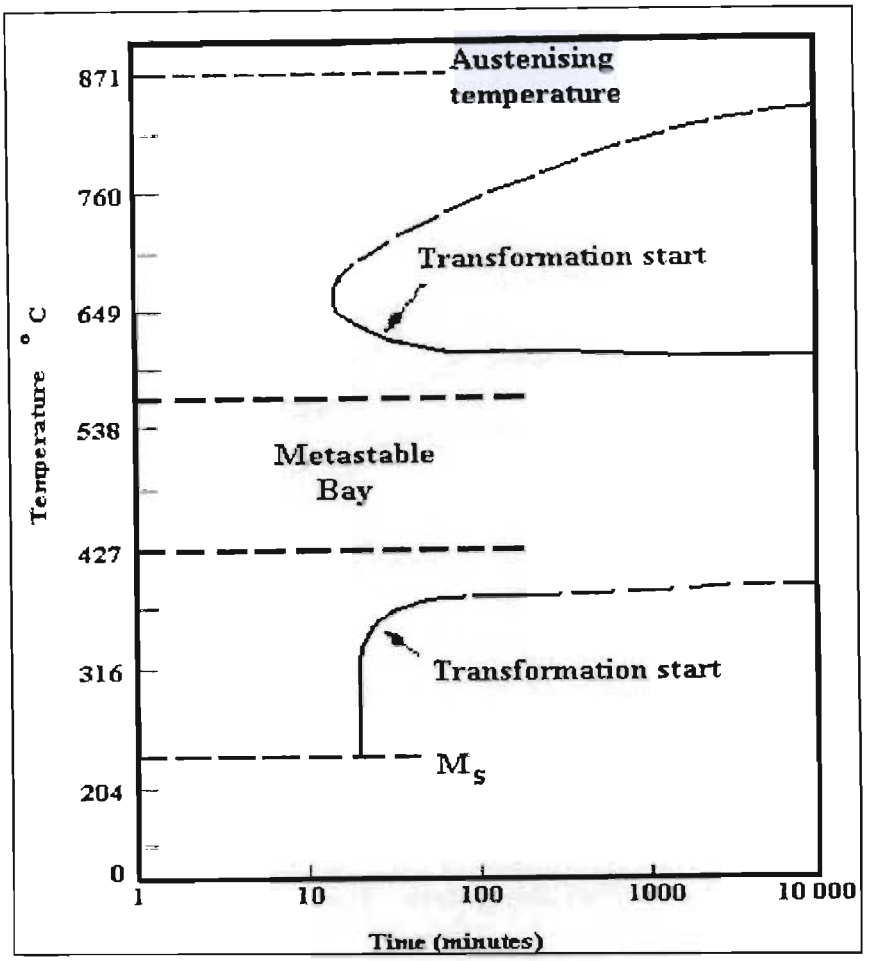

Figure 1.4: MetasTable austenitic bay engineered into the TTT curve by alloying chemistry [43, 61]

Ausforming increases the strength of the material due to the fact that the metastable bay falls below the recrystallization temperature. This warm work process can be carried out in a variety of ways, such as rolling, extrusion, forging etc. Figure 1.5 shows the effect of 0%, 20%, 40%, 60%, 80% PDA (curves /0, /1, /2, /3 and /4 respectively), on the stress-strain curve of a typical metastable alloy. Prior Deformation of Austenite (PDA) is a classic method of increasing the strength of metastable alloys.

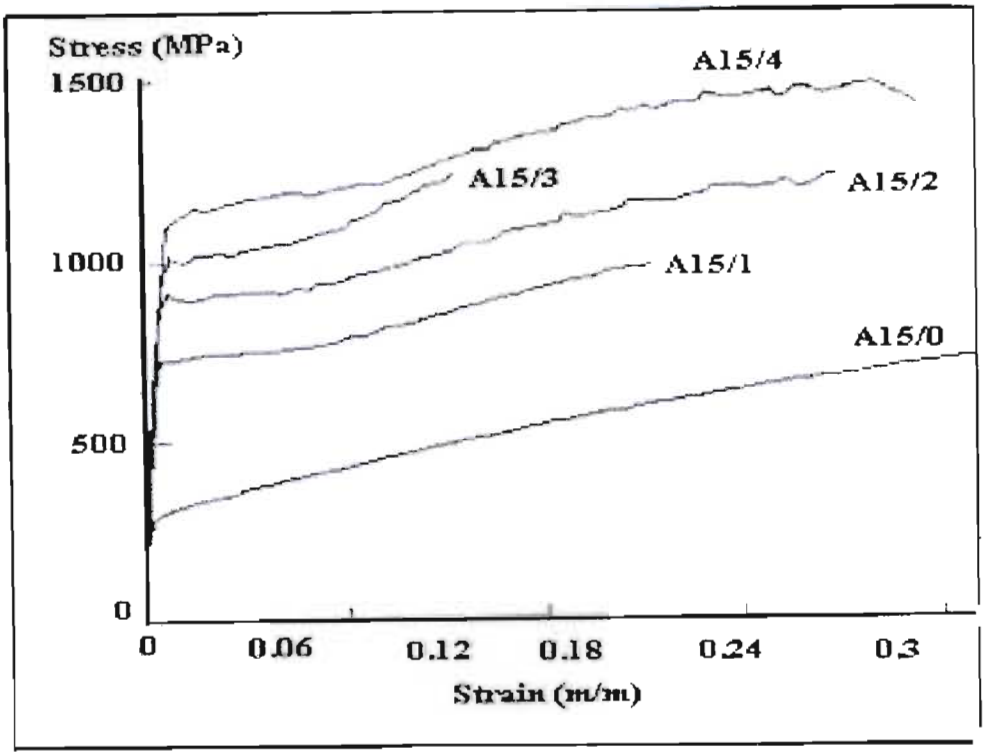

Figure 1.5: Incremental increase in PDA resulting in an increase in strength of metastable alloy [107].

Furthermore if the PDA is conducted above the M_d temperature, this results in the creation of a high dislocation density in the metastable alloy and therefore increases the number of nucleation sites for martensite. This also results in the change in the chemical compositions on a microscopic level and destabilization due to the precipitation of carbides and the austenitic stabilizers from the austenite matrix respectively [3]. Therefore, further destabilizing the austenite. At any given strain the matensitic volume fraction produced at a given strain measurement is directly dependant on the amount of PDA and the temperature at which the PDA is put into the material. Figure 1.16 shows the influence that the % PDA has on the rate of the induced transformation. It demonstrates clearly that the greater the amount of work done, the steeper the transformation rate, and therefore the more destabilized the austenite becomes.

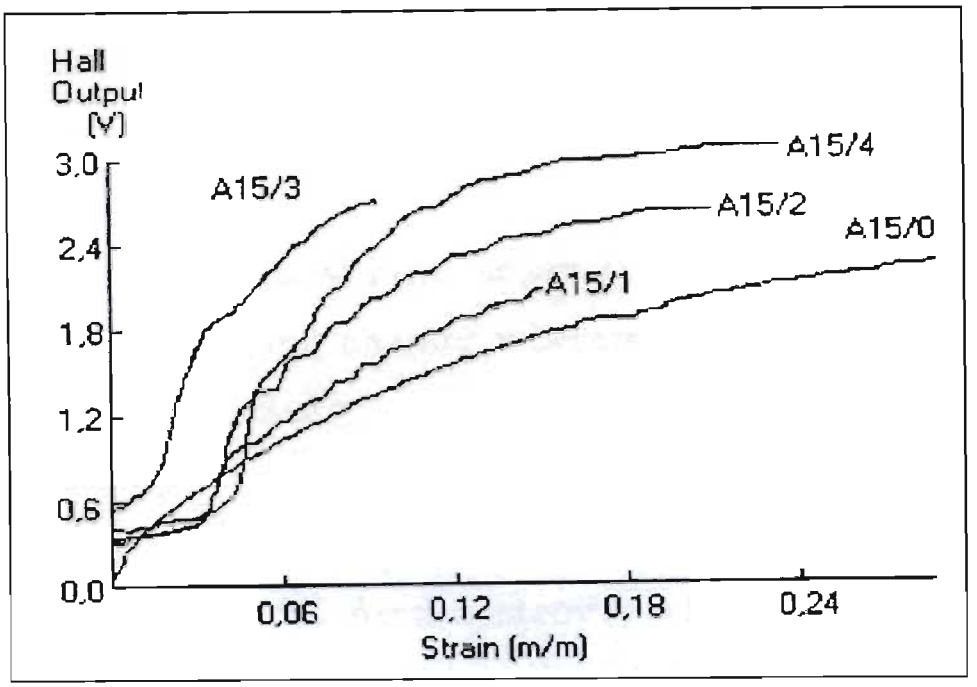

Figure 1.6: The influence of % PDA on austenitic strain-induced transformation [52, 77]

The closer the PDA temperature comes to the M_d temperature the better the strength levels and strain-induced transformation levels that are achieved. It was noted that higher values of PDA temperature results in a lower M_d temperature [52]. Therefore it was deduced that martensitic nucleation was heavily influenced by the chemistry of the alloy, the processing history, the environmental temperature to which the material is subjected, the strain rate and the loading conditions [24]. In addition, the martensitic product phase is affected by the PDA, the martensite precipitated from non-worked austenite is coarser than that found in the worked austenite [43]. The reason could be due to the following facts:

- Distorted austenite grain boundaries were more effective at limiting the size of martensite plates.

- The twisting of the austenite lattice could have restricted the martensitic shear to shorter plate lengths.

- The incremental increase in grain boundaries means that the probability for a site for martensite to nucleate is higher.

- The advancing martensitic plates are blocked by heavily worked slip bands [46].

1.3.2 Transformation Kinetics

The movement of atoms along the slip plane (along the grain boundaries) during cold working results in the destabilization of the austenitic crystal structure in its metastable parent state, i.e., the stabilizing alloying elements are leached out of the austenite martrix, which results in acute localized nucleation sites for martensite along the slip planes [40, 51, 50-51]. Stacking Fault density and the dislocation density of the substructure are factors that also affect the kinetics of transformation. Other factors have already been mentioned in the previous section.

Martensite formed due to localized nucleation along the slip planes differs from that precipitated in martensitic stainless steels. Martensitic nucleation produced due to strain effects has a varying crystal structure lattice (either BCC or Hexagonal Close Packed (HCP)), low carbon content but still produces a tougher material. This was because localized matensite precipitated at these nucleation sites and inhibited the further movement of atoms along the slip plane, thus making the material stronger, harder and resistant to further distortion due to cold working.

Scientific data gathered by various researchers shows that austenitic steels displayed a certain degree of ferromagnetism, which is dependent on the alloy chemical composition and the amount of cold working. Research has also been conducted on the evaluation of the behavioural patterns of Fe-Mn and Fe-Mn-Cr (though not TRIP steels in true essence) austenitic stainless steels (AISI300 series) simultaneously. It is deduced that the transformation exhibited was from austenitic BCC to HCP to BCC [60] (or B.C. tetragonal depending on carbon content of the strain-induced martensite). Fe-Mn alloys containing the following elements; C, Cr, Ni and Co exhibited the transitional HCP phase. However, it is noted that the percentage composition of carbon has the greatest effect on the strain-induced martensitic nucleation, which declined at both the M_s and M_d level for the particular TRIP alloy.

Previous research has shown that transformation occurred inhomogeneously along the gauge length of a tensile specimen (uniaxial tensile testing) such that the region where martensite had formed becomes stronger than the rest of the gauge length and so necking, that is, the mechanical instability which concentrates subsequent plasticity in the neck, is delayed. Once the transformation has occurred to a significant extent along the entire gauge length the specimen deforms homogeneously throughout the gauge length until failure. The increased

uniform plastic deformation observed in these steels corresponds to the increased levels of energy absorption capacity [81, 83-84, 15, 46, 65-66]. The magnetic response of the TRIP steel could then be monitored by the use of a hand held magnetic meter.

1.3.3 Temperature Effects on the Ferromagnetic Response of Strain Memory Alloy Sensor

The phase transformation from the metastable austenitic parent phase to thermodynamically stable, matensitic product phase is assumed to occur due to Gibb's free energy change (The balance between the contributions from the enthalpy and entropy terms to the free energy of a reaction depends on the temperature at which the reaction is run.) that occurs due to transformation, which varies as a function of deformation temperature. Research data has shown that more martensite is precipitated (increase in ferromagnetic response) with decreasing temperature. The temperature exhibited the greatest influence on the strain-induced martensitic transformation at temperatures above M_s temperature. This was also found to be in agreement with the behaviour documented by TRIP steel Researchers [2, 7, 16, 25, 27-29, 41, 47, 67-68]. Figure 1.7 shows the temperature variation of the response of a mestastable sensor alloy (Fe-18 Mn- 13Cr-1Ni sensor alloy).

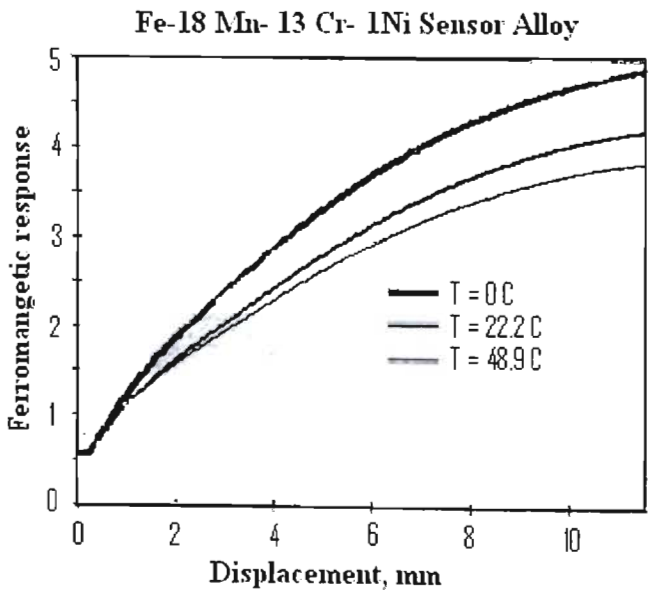

Figure 1.7: **Ferromagnetic response curves of Fe-18Mn -13Cr-1Ni sensor alloy at three temperatures [108]**

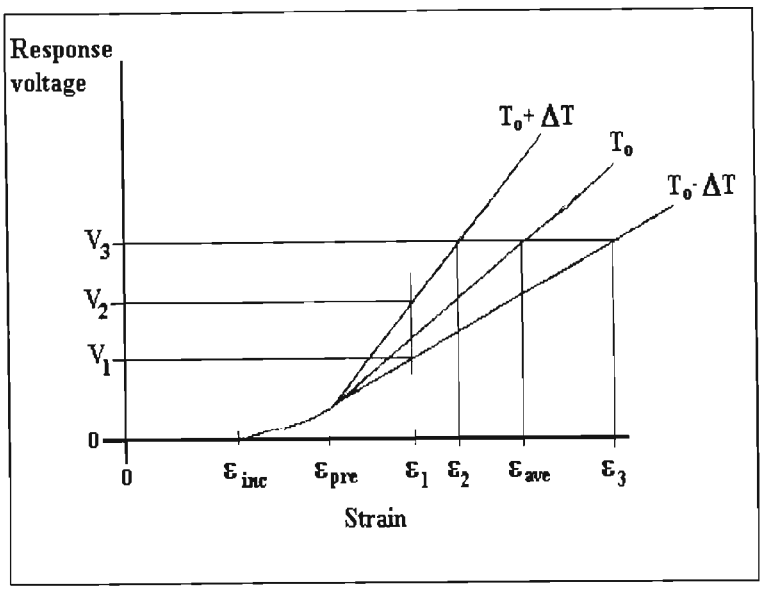

Figure 1.8: Possible error in reading on strain memory sensor due to the temperature dependence of martensite formed in normal strain memory alloy [108]

The temperature dependence on the ferromagnetic response greatly affects the response of strain memory alloy. Figure 1.8 illustrates that the error introduced by the temperature dependence increased with the incremental increase of martensitic precipitation. The sensor specimen in this case was pre-strained (ε_{pre}) to a level ε_{pre} (where ε_{pre} >incubation strain (ε_{inc})). A set reference point was then established from which response readings where measured. Any deformation, i.e., further plastic strain of the specimen results in increased martensitic precipitation. The additional martensite depends on the deforming temperature and strain at that particular deforming temperature. If the additional straining produced a total strain of ε_1, then the corresponding ferromagnetic response in terms of measured voltage lay between V_1 and V_2. The actual strain is made possible by assuming that the deformation occurs at a constant or average temperature during the last inspection period and the present inspection. For the particular case the average temperature was assumed to be the same as that of the installation temperature T_o. The error bar on the strain measurement would then extend to ε_2 and ε_3

The most feasible solution to the temperature dependence problem is identifying the most suitable alloy chemical composition that has little or no temperature dependence.

Fe-Mn-Cr alloys are found to be least affected by temperature. This is due to the fact that the intermediate phase, ε (epsilon) martensite forms prior to the stable, ferromagnetic, ά (alpha prime) martensite. The ε martensite formed at the intersecting bands parallel to the {1 1 1}

plane in the austenite. The ά martensite is considered to nucleate at the ε martensite band intersection, which makes the probability of effectively controlling the amount of ά martensitic nucleation greater, i.e., this is achieved by altering the ε bands density within the austenite, which in turn assumes that the amount ά martensitic nucleation is constant regardless of temperature variation during service, and that the lowest service temperature above the temperature where the precursor ε bands are formed.

1.3.4 Effects of Strain Rate on the Phase Transformation Kinetics

Documented work conducted by researchers has concluded that the speed at which the testing of the TRIP steel material specimen took place had a profound effect on strain-induced phase transformation on austenite stainless steels. However, much emphasis is attributed to the work conducted by Bressanelli and Moskowitz [68-75] as it is most relevant to the subject.

Research data deduces two opposing points with regards to the effect of test speeds on strain-induced phase transformation of tensile specimens. The first one is that the tensile strength decreased rapidly due to increased tensile testing speeds, resulting from the specimen heating up. This meant that lesser and lesser martensite yielded with respect to increased test speeds. The second reason is that the effect of incremental test speeds results in the decrease of tensile elongations [8, 27-28, 47, 66-68 and 81]. In both points cited above the decrease in strength has been readily explained, but not the decrease in elongation, meaning that the effect on elongation is beneficial due to martensitic precipitation during straining, which contradicted Cohen's assertion. Form and Baldwin research data on the effects of speed during testing of test specimen on the phase transformation could not account for the effect of strain rate on strain-induced phase transformation.

Research conducted by Bressanelli and Moskowitz on the effects of test speed on completely austenitic steels prior to tensile testing, helped in understanding the influences on tensile elongation, the effects of the chemical composition and that of temperature. The outcome of their research predicted that slower test speeds yielded greater martensitic volume fractions for a given strain (elongation) as opposed to higher test speeds [75], which is depicted in Figure1.9 below. The alloy subjected to heat A yielded a lower volume fraction of martensite compared to the alloy subjected to heat B.

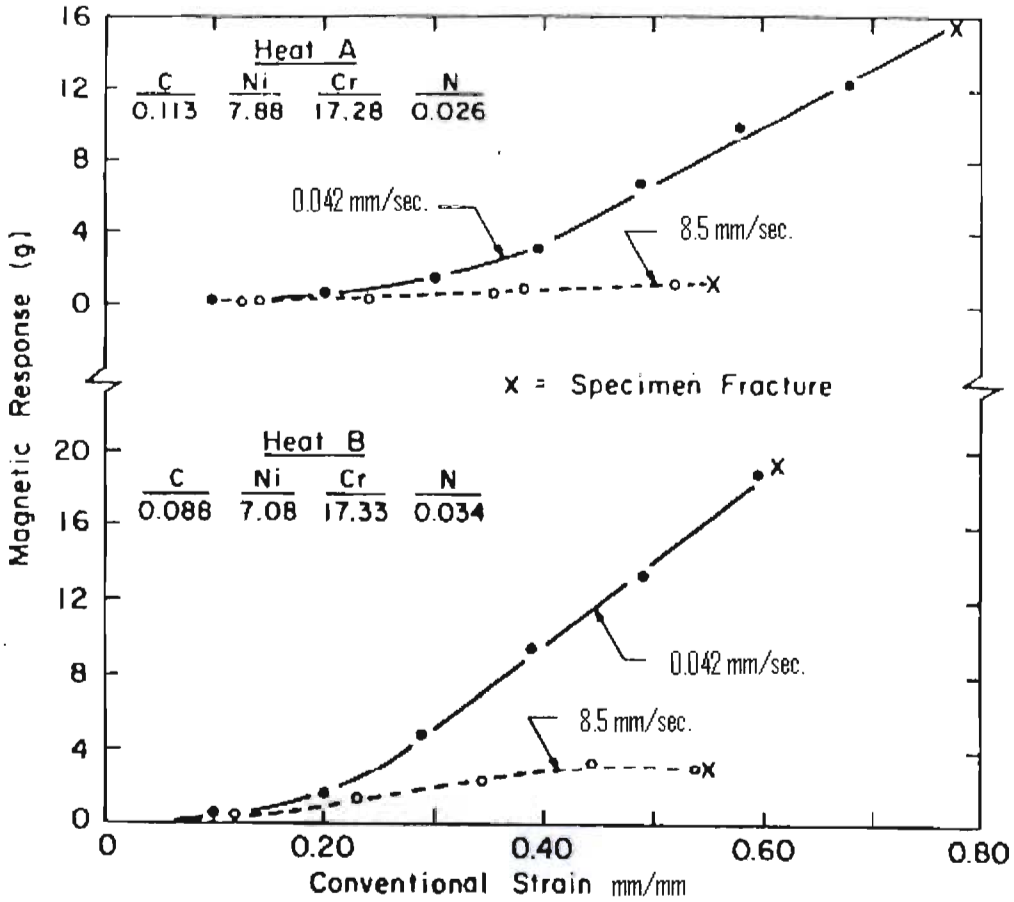

Figure 1.9: Influence of test speed and temperature on the response for the strain memory alloys [75].

Figure 1.10 shows that regardless of the test speed, either high or low, the temperature dependence as cited before has an adverse affect on the strain-induced phase transformation. The ferromagnetic response of the test specimen tested in water was much higher that that tested in normal air (room temperature). From Figure 1.10 the ferromagnetic response was constant throughout the speed range. There was practically no change in elongation and tensile strength of the material.

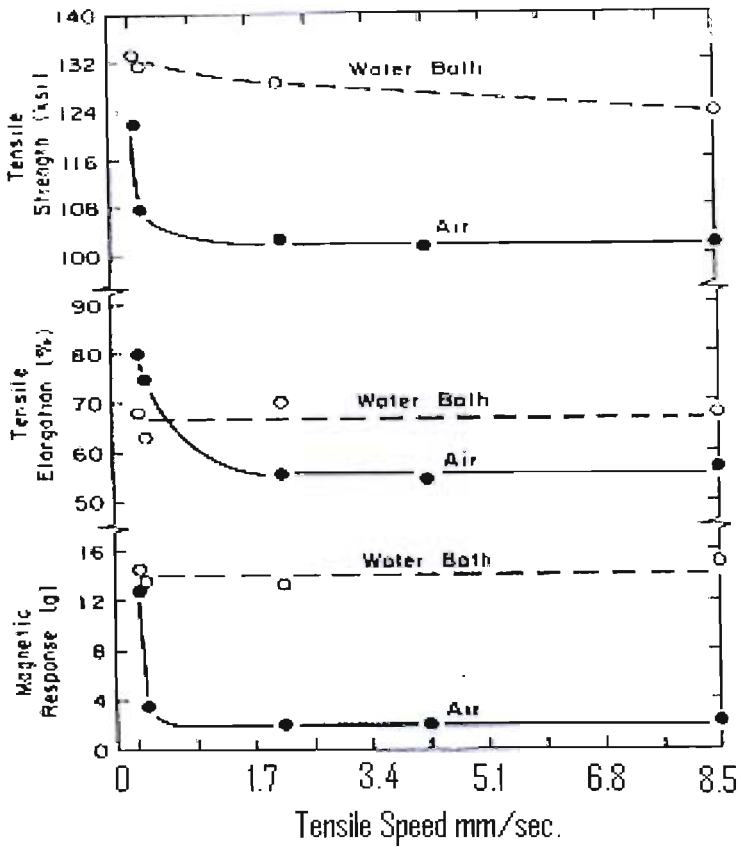

Figure 1.10: Comparison of tensile and ferromagnetic properties of specimens tested at different speeds and temperatures [75].

Bressanelli and Moskowitz finally therefore asserted that the decline in tensile strength and strain hardening (hardening) of metastable austenitic stainless steel was due to increasing test speeds resulting from the decrease in yield quantities of the martensite. This is as a result of increasing temperature depicted by Figure 1.10.

1.4 Fracture Mechanics of TRIP steels

Work has been conducted by researchers such as Chanani, Antolovich, and Gerberich [85], Antolovich and Singh [86], Antolovich, and Fahr [84] on fracture toughness of TRIP steel with regards to temperature, effects on chemical composition and austenitizing temperature, i.e., the degree of warm working. The processing treatment for a set of TRIP steel is displayed in Tables 1.2 and 1.3 below [84].

Table 1.2: Compositions of alloys used [84]

Alloy designation	Nominal composition (wt. per cent)						
	Fe	Cr	Ni	Mo	Mn	Si	C
610*B*	73·7	10·0	6·0	5·0	1·5	3·5	0·29
683-18*A*,*B*	Bal	9·0	8·0	4·0	1·0	2·0	0·26
683-19*A*,*B*	Bal	9·0	8·0	4·0	1·0	2·0	0·24

Table 1.3: Processing Treatment [84]

Alloy designation	Forging temp °C	Aust. temp °C	Initial sample size (in.)	Reduction schedule at 460°C	Initial time at 460°C (hr)	Heating time between steps (min)
610*B*	1200	1200	0·5–0·7	Reduced to 0·5 in. in one step	1·0	0
			0·7–1·0	Reduced to 0·5 in. in 3 equal steps	1·0	10·0
			1·0–1·7	Reduced to 1·0 in. in 100 mil steps Reduced to 0·7 in. in 50 mil steps Reduced to 0·5 in. in 20 mil steps	1·0	10·0
683-18*A*	1080	1080		Processing schedule at 460°C depends only on initial sample size and not on alloy designation and is as given for alloy 610*B* above for all alloys		
683-18*B*	1200	1200				
683-19*A*	1080	1080				
683-19*B*	1200	1200				

Alloys 683-18 and 683-19 in condition A and condition B are considered as a function of the amount of deformation at 460°C for both room and liquid nitrogen test temperatures. The austenite stability is measured by the yield strength and is approximately constant for all amounts of deformation. The constant yield is attributed to two competing factors. These were

- The mechanical working of the austenite tends to stabilize it against transforming to martensite by strengthening the matrix, thus requiring a larger external stress to form martensite due to this effect [84].

- The mechanical working within the 460°C temperature range results in the stabilization of the austenite, which in turn results in the destabilization of the austenite chemistry. Thus this effect results in less dependence on higher stress levels required for martensitic precipitation. Therefore the constancy of the yield stress with increasing deformation at 460°C is due to the mechanical stabilization that is offset by the chemical destabilization [84].

In addition, the incremental ultimate strength is affected by two other factors. These are

- The thermo-mechanical working increased the hardening of the material.
- The incremental increase in martensitic volume fraction during straining.

The fracture toughness represented for the two different conditions (conditions A and B) varied considerably, the square boxes on the line data excluding the solid points (specimen that were pressed at 460°C). Antolovich and Fahr asserted that the fracture toughness increased with yield strength, more so for materials that were tested in condition B, which is displayed in Figure 1.11. The yield data lies on the single scattered band whose mean is represented by a horizontal line.

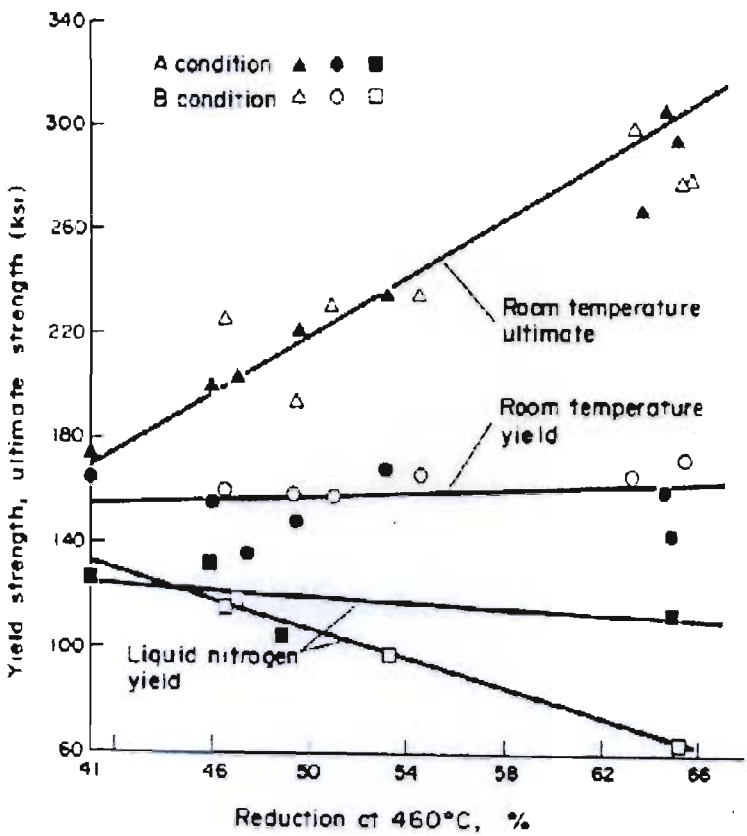

Figure 1.11: Yield strength and ultimate strength of alloys 683-18 and 19 in both the A conditions and B conditions as a function of the deformation at 460°C [84].

Results [97] obtained from fatigue tests carried out using liquid nitrogen at a temperature of -195.8°C in the cryostat by Antolovich and Fahr showed that no martensite was detected, i.e., no ferromagnetic response was detected, suggesting that no spontaneous martensite occurred. However, in both the A and B conditions, there is a significant decrease in the toughness. Figures 1.12 and 1.13 show the variation in fracture toughness of the two different conditions, with alloys in the B condition proving to be significantly tougher than those in the A condition.

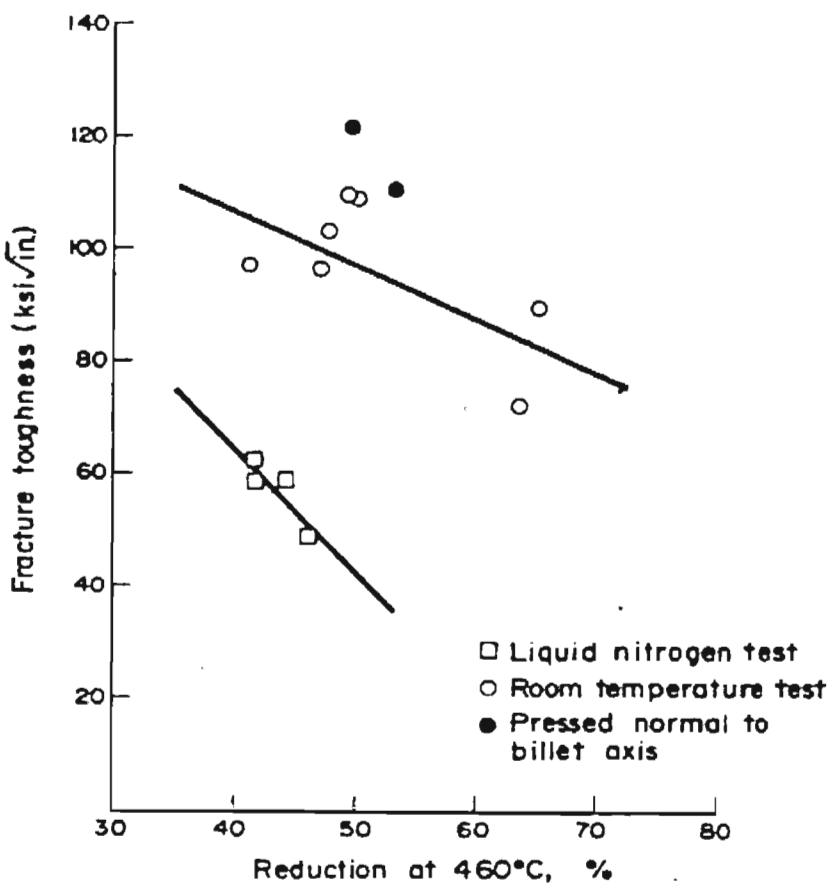

Figure 1.12: **Fracture toughness vs. percent reduction at both room temperature and liquid nitrogen temperatures for alloys 683-18 and 19 in conditions A (austenitized at 1080°C) [84]**

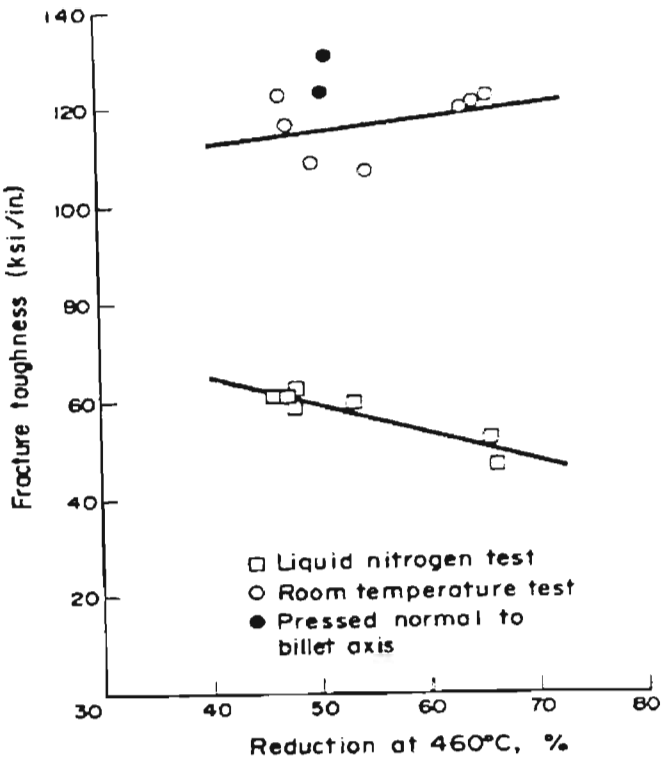

Figure 1.13: Is the same as that of Figure 1.2 except that show the fracture toughness increased at room temperature in the B conditions (austenitized at 1200°C) [84]

Three factors contributed to the decrease in toughness, these are

- The stability of the austenite decreases due to the decrease in temperature, i.e., the free energy of the austenite relative to martensite increased when compared to results at room temperature. This is evident from the decrease in the stress required for the necessary precipitation of martensite (M_s Temperature was approached) which is illustrated in Figure 1.12. This meant that the strain-energy absorption capacity of the transformation decreased since the stress at which it took place was lowered.

- The plasticity of the austenite is not fully utilised at room temperature. Since austenite is F.C.C material, its yield strength is not temperature dependant and even at low temperature it was not expected to be tough.

- Martensite, at low temperature is a brittle material. This is due to its B.C.T crystal structure. The thermal activation energy or lack of it strongly affected the plasticity,

and at low temperature martensite does not dissipate energy readily by plastic deformation.

Antolovich and Fahr enhanced the fracture toughness of TRIP alloy by further improving the stabilization of the austenite stability (by increasing the percentage silicon content in alloy 610, chemical composition given in Table 1.12), where the alloys were subjected to high stress at low temperatures, preferably within the plastic range of the austenite required for martenite formation. The austenite plasticity is then fully utilized and the TRIP reaction dissipates a significant amount of energy per crack advancement. The improvement in stability of the austenite matrix results in the retardation of the precipitation of carbides during the pressing at 460°C by decreasing the diffusion rate and as a result the stability of austenite increased against any amount of pressing at 460°C. Figure 1.14 shows the same low toughness variation in terms of fracture toughness at room temperature as that of the other alloys in B condition. This is because transformation does not take place at room temperature; the toughness of austenite decreases with increasing pressing at 460°C. A combination of mechanical working at 460°C and low test temperature decreased the austenite stability to a point where the TRIP reaction took place and increased the fracture toughness with increased processing.

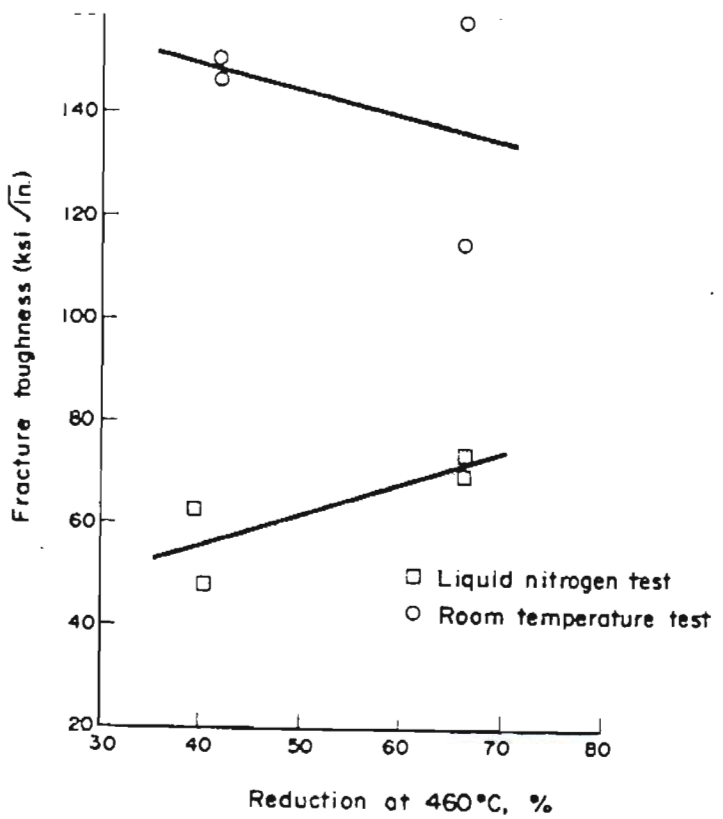

Figure 1.14: Fracture toughness increase at sub zero temperatures in liquid nitrogen, in B condition [84]

Antolovich and Singh [86] were first to assert that the transformation from austenite to martensite, the phase transition absorbed the strain energy that would otherwise be available for crack propagation, thus resulting in a higher fracture toughness at a low temperature regime than that at room temperature, which confirmed the assertions of Antolovich and Fahr [97] and Chanani, Antolovich, and Gerberich [98]. Secondly the plane fracture toughness of TRIP steels as a function of temperature for the two distinctive regimes, concluded that at high temperatures (100°C to 200°C) no martensite precipitated thus there was no ferromagnetic response as opposed to low temperature testing (-196°C to 20°C) where a ferromagnetic response was detected. This is illustrated in Figure 1.15.

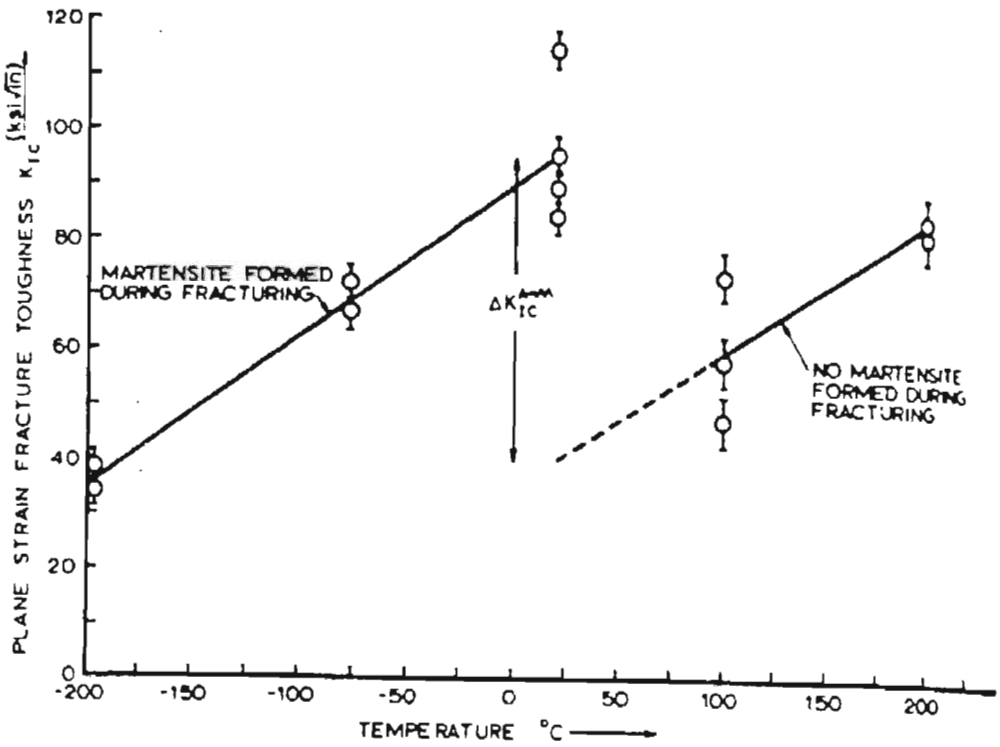

Figure 1.15: Variation in fracture toughness to temperature for two distinct regimes, a low temperature and high temperature for alloys deformed 75% at 460°C [86]

CHAPTER 2

Mechanical Modelling using Finite Element Analysis (FEA)

2.1 Introduction

Finite element analysis (FEA) is a numerical method that uses a numerical rather than an analytical approach to obtain an approximated solution for any complex geometric problem or engineering application. The use of FEA allows for greater accuracy in the solutions to engineering applications, which is achieved either by stating assumptions that are simplified making it easier to work out the solutions to the problems, or by approximating a solution through a numerical approach while maintaining the complexities of the problem. Several techniques exist that can be utilized to solve problems, however the most common technique utilized is the typical finite difference method [77, 87-88], which gives a step by step approximation to the solution for a given set of governing equations that are improved upon by the adding together of more points, thus giving it the ability to handle reasonably complex problems. The finite difference method is inadequate for modelling irregular geometries with complex boundary conditions. Therefore problems which involve the modelling of irregular geometry are best carried out using Finite Element Analysis, FEA, by looking at the solution region in terms of many separate, interconnected sub-domains or elements.

2.2 The Theory of the Finite Element Analysis

The finite element method takes the entire structural problem and then divides it into region of elements which contain their own formulated unique functions. It then sums up all the individual functions of every element to create an approximated final solution for the entire problem. The approximated functions are defined at particular sites, commonly referred to as nodes, which are situated at the beginning and end of the elements. In some cases they are also placed at the centre of the element. The accuracy of the solution depends largely on the element sizes, type of elements to be used and the number of elements together with their specified interpolation functions. These functions are specifically chosen so that their derivatives are continuous across adjoining element boundaries [77].

The steps listed below illustrate the techniques utilized to apply finite element analysis to an engineering problem.

- Discretisation: This is a process by which the entire solution to the problem is divided up into regional elements. The advantage of this is that one can define the number and type of elements in specified areas of interest, which is crucial in improving the accuracy of the final solution.

- Selection of the Interpolation Function: nodes are assigned to each element, after which the type of interpolation function required to represent the variation of the solution region over the element is implemented. Polynomials are commonly utilized to represent the interpolation function for the solution region because they can be easily differentiated and integrated [77].

- Definition of element properties: This is the stage at which the matrix equations are determined to express the properties of individual elements, once the modelling of the geometry has been completed. This is also carried out only after the type and size of the element and interpolation function have been selected for the particular model.

- Assembly of the element stiffness matrices: The stiffness matrices of the elements are combined to express the behavioural pattern of the elements which in turn represents the final behaviour of the structure in terms of its solution, for example, the element stiffness matrix can relate the nodal displacement to the applied loads at the nodes[77].

- Solution of the system of equations is calculated to obtain the final solution of the entire problem.

As mentioned above, the accuracy of the solution for any irregular geometry is greatly affected by the type and size of elements (spacing of the nodes) to be implemented. For irregular geometry, it has been found that the triangular type element gives the most flexible solution in modelling irregular structural shapes relative to rectangular shaped elements. Areas of steep stress gradients can be accurately modelled by altering the sizes of the triangular elements to give a detailed representation of what is happening in these regions. Finite element analysis can also model structural elements with anisotropic and non-homogeneous properties. Various boundary conditions can be applied as well as different types of loading systems. The types of boundary conditions and loading conditions are entirely subjective to the engineering problem

and engineer's discretion. In addition, finite element analysis can also carry out non-linear analysis of structures that have materials exhibiting non-linear properties [77].

2.3 Finite Element Problem Definition

Problem domains in finite element analysis are characterised through processes such as continuum or Eulerian techniques by the field quantities, which are defined at every point in space. Field quantities such as acoustic potentials, mass concentration, temperature, electromagnetism, stress and many more are defined as continuum problems. Finite element analysis approximates the solutions to these problems by solving their partial differential equations with respect to a given set of boundary conditions. The solutions are normally derived within the given boundary conditions. The boundary conditions are classified into two types; the closed loop boundary conditions and open loop boundary conditions. In closed loop boundary conditions the finite element method approximates the solution of the problem up to and along the entire boundary parameters.For the open loop boundary conditions the solution to the problem is approximate to the point where the boundary equals infinity. However no boundary conditions exist at infinity [77, 89].

2.4 Problem Definition

To approximate the solution for non-linear and linear boundary problems that can range from an entirely analytical to numerical solution, a technique such as the variational approach with respect to finite element analysis is normally used.

2.4.1 Variational Method

The variational technique seeks to find the unknown function or functions that make the stationary function such as $I(\phi)$ or a system of functionals that are subjected to the same boundary conditions while other techniques such as the differential equation formulation involves the integrations of a differential equation or set of differential equation for a given set of boundary conditions.

The application of the variational technique to continuum problems has proved to be a much better technique than the use of the differential equation formulation. This is because,

1. The variational technique is more flexible in dealing with extremely complicated boundary conditions, i.e., it treats the complicated boundary condition as normal boundary conditions.

2. The functional utilized for the variational principle (representing a physical quantity) contains derivatives of an order lower than that used by a differential operator. This also means that an approximate solution can be deduced for huge and complex sets of functions.

3. The variational technique can be utilized to prove the validity of the solution by the use of variational calculus.

4. For problems that have reciprocating variational formulations, i.e., one function maximized and the other function minimised, the variational function is better suited because of its flexibility.

Continuum problems are generally expressed in the form of a variation function. This is also generally expressed in the form of a Ritz approach, which is essentially a unique case of the finite element analysis, since both the Ritz Method and Finite Element Analysis utilize interpolation functions to satisfy continuity requirements [77].

2.4.1.1 Comparison of the Finite Element method to The Ritz Method

Both the Ritz Method and Finite Element Method utilize a set of linear or nonlinear trial functions at a reference point for approximating a solution for a particular problem. In addition, the approximation of the solution improves with an increasing number of trial functions and increasing the number of adjustable parameters, which converge to give a more realistic solution to a problem [77, 90, 94].

The main difference between the Finite Element Method and the Ritz Method is that in the finite element method, a given domain is represented (discretized) by a collection of geometrically simple shapes (elements), and on each element of the collection, the governing functions is formulated using any variational method. The trial functions are systematically

generated for each element (typical) elements using essential boundary condition. The elements are connected together by imposing the continuity of variable across the interelement boundaries. Also in the Finite Element Methods a combination of different boundary conditions can be implemented that do not need to suit specific continuity conditions. Whereas the Ritz method employs trial functions that are defined for the whole domain which makes them applicable only to simple geometric structures. This limitation is also present in the Finite Element Method. It exists in the form of what type of element shape is to be used for the meshing of complex geometries. However due to the fact that there are options for different shapes of element in Finite Element Methods that can be employed within any region, this gives the Finite Element Method more flexibility to optimally use the finite element available. This makes the Finite Element Method more versatile than the Ritz Method [77, 94].

2.4.1.2 Element definition

Elements are regions of space where a field variable exists. Elements are interconnected in space to one another at set points called nodes, which are situated at the element's boundary surfaces. The elements are then meshed together to create a spatial subdivision rather than a material subdivision and solution domain [77, 91]. The approximated solution as stated in the theory of finite element analysis is the summation of each unique field function for each individual element. These functions are known as interpolation function, shape function or field variable model.

2.4.1.3 Element Functions using Variational Principle

The approximated solution of the element is achieved by determining the value of the field variable at the element nodes, at which point the functional $I(\phi)$ is made stationary. For $I(\phi)$ is expressed as follows [77]

$$\partial I(\phi) = \sum_{i=1}^{n} \frac{\partial I}{\partial \phi_i} \delta\phi_i = 0 \tag{2.1}$$

where n is the total number of discrete values of field variables, ϕ_i, assigned to the solution variable. The $\delta\phi_i$ terms are independents, thus equation (2.1) is satisfied when

$$\frac{\partial I}{\partial \phi_i} = 0 \qquad I = 1, 2, \ldots, n \tag{2.2}$$

Therefore the sum of individual element functionals defined for all elements within solution domain may be expressed as

$$I(\phi) = \sum_{e=1}^{M} I^{(e)}(\phi^{(e)}) \tag{2.3}$$

The constant M represents the total number elements and superscript e denotes an element. Equation (2.3) can be written as

$$\delta I = \sum_{e=1}^{M} \delta I^{(e)} = 0 \tag{2.4}$$

The variation of $I^{(e)}$ is taken only with respect to the nodal values associated with the element (e). Equation (2.4) is rewritten as

$$\frac{\partial I^{(e)}}{\partial \phi} = \frac{\partial I}{\partial \phi_i} = 0, i = 1,2,....,r \tag{2.5}$$

where r is the number of nodes assigned to the element (e) and characterizes the behaviour of the element (e). Equation (2.5) can be rewritten in terms of a square matrix and the field variable may be stated as

$$\frac{\partial I^{(e)}}{\partial \phi} = K^{(e)}\phi^{(e)} - F^{(e)} = 0 \tag{2.6}$$

where $K^{(e)}$ is a square matrix of constant coefficients $\phi^{(e)}$ is the column vector containing nodal values of the field variable and {F} is the vector of resultant nodal action. Thus the overall form of the equation (2.6) may be expressed as [77]

$$\frac{\partial I}{\partial \phi_i} = \sum_{e=1}^{M} \frac{\partial I^{(e)}}{\partial \phi_i} = 0, i = 1,2,...n \tag{2.7}$$

or

$$\left(\frac{\partial I}{\partial \phi}\right) = 0 \tag{2.8}$$

Therefore equation (2.7) gives an approximated solution for n nodal values of ϕ. If the solution domain consist of q nodes where ϕ is specified by boundary conditions, n-q equations will be formulated to solve for n-q unknowns.

2.4.1.4 Interpolation Functions and Mesh Generation

Interpolation functions must satisfy a set of prescribed conditions at a finite number of points. In FEA, the points are nodes of an element, and the prescribed conditions are nodal values of a field variable; as mentioned before interpolation functions are generally polynomials. The accuracy of an approximated solution increases by increasing the number of elements used to model a problem of a given domain in finite element analysis. A convergence test is carried out so that the right numbers of elements are used to model a fairly accurate approximation for the solution. For convergence (fine tuning the element mesh density) to occur, the mesh requirement must be made in regular fashion so as to satisfy the following factors [77, 92-93]

- All previous meshes will be contained in the current refined mesh.
- The geometric size of the element is always made smaller so that the solution domain exists within the element
- The same order of the interpolation function should be retained through all the stages of the refinement process.

The interpolation functions of each element are normally combined together so that monotonic convergence is assured. The general form for the interpolation functions $N^{(e)}$ is defined as follows:

$$\phi^{(e)}[N^{(e)}]\{\phi\}^{(e)}, e = 1,2,\ldots\ldots,M \tag{2.9}$$

where $N^{(e)}$ and $\{\phi\}^{(e)}$ parameters represent the row vector of interpolation functions of the nodal coordinates and column vector respectively. The two parameters are heavily influenced by two factors, which they are required to satisfy. These are [77]

1. All uniform states of ϕ and its partial derivates up to the one order less than the highest order derivatives appearing in $I(\phi)$ should have representation in $\phi^{(e)}$ when, in the limit, the element size shrinks to zero.

2. The field variable and any of its spatial derivatives up to one order less than the highest order derivatives appearing in $I(\phi)$ must be continuous at the element boundary [77, 92-93].

It is also required that the field variables (interpolation functions) of the elements are not altered during linear transformation from one coordinate system to another. Elements that satisfy the first factor are known as complete elements and elements that satisfy the second factor are referred to as compatible elements.

The degree of continuity of a field variable at the element interfaces are expressed as C^0 and C^1 continuity for field variables that are continuous for the first derivatives. This also follows for a second order derivative, which is expressed in terms of C^2. Therefore functions of the element equations may have derivatives up to $(r+1)^{th}$ order. In addition, the completeness and compatibility requirements must be fulfilled to guarantee convergence as the element size decreases. These requirements are applicable and satisfied for element equations whether they are derived for the variational method or any other method [77, 92-93].

2.4.2 Element Shapes

The solution domain of any engineering problem can be accurately modelled in finite element analysis by the combination of a volume of uncomplicated element shapes. If a one-dimensional problem, which consists of one independent variable, is considered, the elements generally used are line segments and the number of nodes allocated to a particular element depends on the type of nodal variables, the type of interpolation function together with the level of continuity required. However, one-dimensional elements can also be integrated to two or three dimensional elements representing a complex two-dimension problem. For instance, in elasticity problems one-dimensional elements can be represented as spars, generally used as

stiffness. For two-dimensional elements, three node flat triangular elements are most commonly utilized elements because of their flexibility. Triangular elements are the easiest elements that can be used to represent a two dimensional continuum or solution domain of any geometric shape. Other two-dimensional elements exist such as four node rectangular elements that are the easiest to construct due to their standard shape. However they are less user friendly when it comes to modelling curved boundaries as opposed to three node triangular elements. For three dimensional problems that possess axial symmetry in cylindrical coordinates, axisymmetric or ring-type triangular elements are normally utilized. Nevertheless, these elements are defined in terms of one or two independent variables [77].

2.5 Mechanical Response Modelling For Solid Mechanics

The application of finite element methods to any solid mechanics problem usually involves the application of the variational method that is required for generating the necessary elemental functions. There are three types of variational methods that are widely used, firstly the Minimum Potential Energy Technique; to which the field variable is defined in terms of a displacement field variable within each element, secondly the Complementary Energy Method (also known as the Equilibrium Method or Force Method), which utilizes the stress field as a field variable and thirdly, the Reissner's principle [77, 109].

2.5.1 Small Deformation of Two-dimensional Elastic Problems

If a two-dimension elastic object is acted upon by extension forces on a body in equilibrium, the potential energy $\prod$ may be expressed in the form [77, 93]

$$\Pi(u,v) = \frac{1}{2}\iint(\tilde{\delta} B^T C\delta - 2\tilde{\delta} B^T C\varepsilon_o)tdA$$
$$- \iint_A F\tilde{\delta}tdA - \int_{s_1} T\tilde{\delta}ds \qquad (2.10)$$

where C contains material stiffness coefficients that are consistent with the constitutive stress-strain relationship. Its form is problem dependant, $t = t(x, y)$ is the thickness of the body, ε_o the column vector of initial strain which could as a result of shrink fits, non uniform temperature distribution etc, $T = [T_x, T_y]$ are the boundary traction components that are defined per unit

length for a unit thickness and F = [X, Y] are the body force components due to gravity, centrifugal action etc.

The matrix $\tilde{\delta}$ that represents the displacement field measured form a reference point is given by

$$\tilde{\delta} = \begin{Bmatrix} u(x,y) \\ \upsilon(x,y) \end{Bmatrix} \tag{2.11}$$

In addition, the **B** components are derived from the strain-displacement relationship which is expressed in the from

$$B = \begin{bmatrix} \delta/\delta x & 0 \\ o & \delta/\delta y \\ \delta/\delta x & \delta/\delta y \end{bmatrix} \tag{2.12}$$

However, the initial quantities of the body force, F, the initial strain ε_o and boundary traction components, T are usually stated. The displacement field (u, υ) that exist in the body during a state of equilibrium is defined such that the total system potential energy assumes a minimum value. The variational method is normally applied to the problem to discretize (divide) the elastic continuum domain into a series of elements of the some shape depending on the problem which a particular type of displacement function is assigned over each element [77].

2.5.2 Displacement Interpolation Functions

The potential energy field is defined in terms of the displacement file variable which has been explained. The potential energy is defined as the summation of each element's potential energy for a given area A of a problem domain Ω, which has been divided into M discrete elements. In addition, the completeness and the compatibility requirements must be fulfilled for the displacement interpolation functions of each individual element, which would also guarantee that convergence would occur as the elements mesh size decreases. The potential energy may then be stated as [77]

$$\Pi(u,v)=\sum_{e=1}^{M}\Pi^{(e)}(u,v) \tag{2.13}$$

For three-dimensional problems such as elastic problems, plane strain and plane stress problems, the polynomial interpolation function must consist of a combination of linear terms and a minimum of one constant to meet the compatibility and completeness requirements.

As indicated before, the potential energy function is expressed in terms of discrete values of the displacement field, under the assumption that the displacement field is approximately related to the nodal values of all r interpolation functions $N_i(x, y)$ for each element containing r nodes. Therefore distributed displacement field, $\delta^{(e)}$, may be expressed as [77]

$$\delta^{(e)}=\begin{Bmatrix}u(x,y)\\ v(x,y)\end{Bmatrix}^{(e)}=\begin{Bmatrix}\sum_{i=1}^{r}N_i(x,y)u_i\\ \sum_{i=1}^{r}N_i(x,y)v_i\end{Bmatrix}=\begin{Bmatrix}Nu\\ Nv\end{Bmatrix}^{(e)}=N\delta^{(e)} \tag{2.14}$$

where $\delta^{(e)}$ represents the element nodal displacement

2.5.3 Element Stiffness Equations

The potential energy functions of the elements (e) are expressed in terms of interpolation functions and unknown displacements in a discretised form as shown below [77, 93]

$$\Pi^{(e)}(\delta^{(e)})=\frac{1}{2}\iint_{A^{(e)}}[\delta^{(e)}B^{T(e)}C^{(e)}B^{(e)}\delta^{(e)}-2\delta^{(e)}B^{T(e)}C^{(e)}\varepsilon_0{}^{(e)}]t^{(e)}dA^{(e)}$$
$$-\iint F^{(e)}\delta^{(e)}t^{(e)}dA^{(e)}-\int_{\Gamma_1^{(e)}}T^{(e)}\delta^{(e)}dS^{(e)} \tag{2.15}$$

The potential energy of the system will have a minimum value that occurs when the first variation of the function disappears, i.e., the potential energy function is equated to zero and may be expressed in the form.

$$\delta\Pi(u,v)=\sum_{e=1}^{M}\delta\Pi^{(e)}(u,v)=0 \tag{2.16}$$

where

$$\delta\Pi(u,v) = \sum_{i=1}^{r} \frac{\delta\Pi^{(e)}}{\delta u_i} \delta u_i + \sum_{i=1}^{r} \frac{\delta\Pi^{(e)}}{\delta v_i} \delta v_i = 0 \tag{2.17}$$

Parameters δu_i and δv_i are independent variables. Then equation (2.17) is only satisfied when

$$\frac{\delta\Pi^{(e)}}{\delta u_i} = \frac{\delta\Pi^{(e)}}{\delta v_i} = 0, i = 1,2,....,r \tag{2.18}$$

for every element (e) of the equation. In matrix form

$$\left[[k]^{q1} [k]^{q2} ... [k]^{qp} ... [k]^{qr} \right] \begin{bmatrix} u_1 \\ v_1 \\ \vdots \\ u_q \\ v_q \\ \vdots \\ u_r \\ v_r \end{bmatrix} = F^q, q = 1,2,..., r \tag{2.19}$$

where p = 1, 2,...., r and r is the number of element nodes. A 2 x 2 matrix $[k]^{qp}$ denotes the stiffness relationship between nodes q and p. $\mathbf{F}^q$ is the resultant external load vector at node q.

$$\frac{\delta\Pi^{(e)}}{\delta u_q} / \frac{\delta\Pi^{(e)}}{\delta u_v} = 0 = \iint_{A^{(e)}} B_q^{T(e)} C^{(e)} B_p^{(e)} \delta^q t^{(e)} dA^{(e)}$$

$$- \iint_{A_{(e)}} B_q^{T(e)} C^{(e)} \varepsilon_{0q}{}^{(e)} t^{(e)} dA^{(e)}$$

$$- \iint_{A^{(e)}} N_q F_q^{(e)} t^{(e)} dA^{(e)} - \int_{C_i^e} Nq T_q^{(e)} dS_q^{(e)} \tag{2.20}$$

where

$$\delta^q = \begin{Bmatrix} u_q \\ v_q \end{Bmatrix} \tag{2.21}$$

denotes the column vector of the two displacement components at node q. $B_q^{(e)}$ in equation (2.20) is the strain- displacement matrix, which is expressed in matrix form as

$$B_q^{(e)} = \begin{bmatrix} \delta N_q / \delta x & 0 \\ 0 & \delta N_q / \delta_y \\ \delta N_q \delta_y & \delta N_q / \delta x \end{bmatrix} q = 1,2,...r \tag{2.22}$$

The definition of the strain-displacement matrix for a two dimension elastic problems stated above is derived from the definition of the three non-zero strain components ε_x, ε_y and ε_{xy}. The last term in equation (2.20) is only considered when elements (e) are positioned at the point or site where the traction vector T (which is normally a boundary a parameter) is specified.

In addition, equation (2.20) incorporates the force-displacement relationship for nodes q, which is expressed in matrix notation by the following relationship

$$k^{qp}\delta^q = F_0{}^q + F_B{}^q + F_T{}^q = F^q \tag{2.23}$$

where

$$k^{qp} = \iint_{A^{(e)}} B_q^{T(e)} C^{(e)} \varepsilon_{0_q}{}^{(e)} t^{(e)} dA^{(e)} \tag{2.24}$$

is the initial force vector at node q, Therefore, the nodal body force is defined by the following expression

$$F_B{}^q = \iint_{A^{(e)}} N_q(x,y) F_q^{(e)} t^{(e)} dA^{(e)} \tag{2.25}$$

Finally the resultant external load at node q may therefore be expressed as

$$F_T{}^q = \iint_{C_1^{(e)}} Nq(x,y) T_q^{(e)} dS_q^{(e)} \tag{2.26}$$

.

The 2 x 2 stiffness matrix for an element with r nodes is given by

$$k^{(e)} = \begin{bmatrix} k^{11} & k^{12} & \cdots & k^{1r} \\ k^{21} & k^{22} & \cdots & k^{2r} \\ \vdots & \vdots & \vdots & \vdots \\ k^{q1} & k^{q2} & \cdots & k^{qr} \\ \vdots & \vdots & \vdots & \vdots \\ k^{r1} & k^{r2} & \cdots & k^{rr} \end{bmatrix} \tag{2.27}$$

where the column matrix of discrete nodal displacement for the elements (e) due to the way the terms in the element stiffness matrix are defined, may be stated as

$$\delta^{(e)} = \begin{Bmatrix} \delta^1 \\ \delta^2 \\ \vdots \\ \delta^r \end{Bmatrix} = \begin{Bmatrix} u1 \\ \upsilon_1 \\ u2 \\ \upsilon_2 \\ \vdots \\ u_r \\ \upsilon_r \end{Bmatrix} \tag{2.28}$$

The force-displacement equation for the elements in matrix notation is also expressed as

$$K^{(e)}\delta^{(e)} = F^{(e)} \tag{2.29}$$

where

$$F^{(e)} = \begin{Bmatrix} F^1 \\ F^2 \\ \vdots \\ F^q \\ \vdots \\ F^r \end{Bmatrix} \tag{2.30}$$

2.5.4 Overall System Equations

The overall form of the entire system equation for a two dimensional elastic problem when discretised may be expressed in terms of matrix notation [77]

$$K^{(2m\times 2m)}\delta^{(2m\times 1)} = F^{(2m\times 1)} \tag{2.31}$$

where the parameter m represents the total number of the nodes allocated to the elements, **F** is the column vector of the resultant nodal forces and **δ** in the column vector of the nodal displacement components for the entire system, As previously stated the initial strain or body force are normally known quantities. However, if the body force and initial strains are assumed to be non-existent, then the force vector **F** is assumed to be zero except where the nodes are subjected to specific external load or displacement. The strain-stress and strain-displacement relationships are derived once the entire system equations for nodal displacement have been solved. The stress components, including those due to displacements and initial strains, may be given as [77, 93]

$$\sigma^{(e)} = C^{(e)}B^{(e)}\delta^{(e)} - C^{(e)}\varepsilon_0{}^{(e)} \tag{2.32}$$

Note: if any initial stress is present, they must be factored in.

Therefore the geometric model becomes a mathematical model whose behaviour is described or approximated by the summation of every interpolation function for every element mesh density, loading and boundary conditions. These equations (interpolation functions consisting of polynomials) depending their particular form, may incorporate restrictions such as homogeneity or isotropy material properties and either plane strain elements or axisyymetric volume element properties. Thus FEA is applied to the mathematic model to simulate what would occur, giving a close approximation of a solution to the problem in virtual reality.

2.6 Finite Element Methods Magnetism (FEMM) Applied To Linear Magnetostatic Problems

Finite Element Methods Magnetism, FEMM, provides a relatively user-friendly platform for solving magnetostatic problems through the implementation of Finite Element Analysis. FEMM achieves this by the utilization of an axisymmetric formulation in terms of a modified vector potential. The advantage of a modified vector potential is that the closed-form expression for each element in the element matrices can be formed. In addition, the average flux density associated with each element can be deduced [100].

2.6.1 Application of Finite Element Methods Magnetism

The magnetostatic response modelling for problems where the magnetic field ais time invariant is better suited to the present application at hand. In this case the magnetic intensity (H), the current density and flux density (B) obey a subset of Maxwell equations [77,100]

$$\nabla \times H = J \tag{2.33}$$

$$\nabla \cdot B = 0 \tag{2.34}$$

Subject to a constitutive relationship between B and H for each material

$$B = \mu H \tag{2.35}$$

If the material is non linear, the permeability (μ) is defined in terms of B and H as follows

$$\mu = \frac{B}{HB} \tag{2.36}$$

FEMM derives a field that satisfies (2.33)-(2.35) via the use of the magnetic vector potential approach. The flux density is written in terms of the magnetic vector potential, A. The first step in the solution for a particular application requires defining the μ = 1 everywhere within the domain of the problem Ω. The field intensity H that satisfy this case and the governing equations is given by [100]

$$H_s = \frac{1}{4}\pi \int_{\Omega} \frac{J \times (r - r')}{(r - r')^T (r - r')} d\Omega \tag{2.37}$$

where r defines the coordinates of the problem domain Ω. Therefore total field strength is defined as

$$H = H_s + H_m \tag{2.38}$$

H_m takes into account the contribution of the areas where the permeability is not equal to one. Thus substituting equation (2.38) into equations (2.23, 2.34 and 2.35) yields relationships of the form

$$\nabla \times H_m = 0 \tag{2.39}$$

$$\nabla^T \times B = 0 \tag{2.40}$$

$$B = \mu(H_s + H_m) \tag{2.41}$$

Incorporating the magnetic vector potential, A, as

$$H_m = \nabla \times A \tag{2.42}$$

and defining the flux density, B, that will always satisfies (2.24). Equation (2.33) may be rewritten as

$$\nabla \times \left(\frac{\nabla \times A}{\mu \cdot B} \right) = J \tag{2.43}$$

Therefore the resultant Maxwell function may be expressed as

$$\nabla^T \cdot \mu \nabla A + \nabla^T \cdot \mu H_s = 0 \tag{2.44}$$

Substituting equations (2.47) into the field intensity H_s yields a varialtional functional that satisfies the original governing equations

$$\Pi = \frac{1}{2} \int_{\Omega} (\nabla A) \mu \nabla A d\Omega + \int_{\Omega} A \nabla \mu H_s d\Omega \tag{2.45}$$

The vector potential is assumed to have the form

$$A = \sum N_i a_i = Na \tag{2.46}$$

where N is the vector of the appropriate shape functions. The variation equation may then be stated as

$$\int_{\Omega}(\nabla N_i)^T \mu \nabla d\Omega + \int_{\Omega} N_i \nabla^T \mu H_s d\Omega = 0 \tag{2.47}$$

which may be represented as a standard set of discrete equations in the form of

$$Ka + f = 0 \tag{2.48}$$

with

$$Kij = \int(\nabla N_i)^T \mu \nabla N_j d\Omega \tag{2.49}$$

$$f_i = \int_{\Omega} N_i \nabla^T \mu H_s d\Omega \tag{2.50}$$

2.6.2 Boundary Conditions

Three sets of boundary conditions exist that are implemented for magnetostatic modelling. They are classified as follows [77,101]

- Dirichlet Boundary Condition: For this type, the value A is clearly defined on the boundary, e.g. A = 0. Normally the boundary condition is define as the vector potential, A, which is normally equated to zero along the boundary in order to keep the flux density from crossing the boundary. This technique is also utilized to simulate symmetric conditions.

- Neumann Boundary Condition: This defines the normal derivative of A along the boundary. Usually, $\partial A / \partial n = 0$ is defined along the boundary to force the flux density to pass the boundary at exactly 90° angle to the boundary. This allows for consistent and accurate modelling of interfaces between materials with varying high permeabilities.

- Robin Boundary Condition: this integrates the Dirichlet and Neumann boundary conditions, prescribing a relationship between the value magnetic vector potential, A, and its derivatives at the boundary. An example of this boundary condition is

$$\frac{\partial A}{\partial n} + cA = 0 \tag{2.51}$$

This boundary condition is most often used by the FEMM in eddy current problems on the interface with bodies with small skin-depth eddy currents. However, for axisymmetric problems, A = 0 is enforced on the linear r = 0 resulting in a valid solution without explicitly defining any boundary conditions, as long as part of the boundary of the problem lies along r = 0.

Note for the technique used for model the FEMM model, a combination of asymptotic boundary conditions and Kelvin transformation are considered due to their relevance.

2.6.3 Open Boundary Problems

Generally finite element methods are best suited to problems with well defined, closed solution regions. Thus with respect to magnetostatic problems, the most feasible solution is to define a boundary sufficiently far enough from the areas of interest, resulting in large solution domain which in turn correspond to large solution times, i.e., the realistic representation of the boundary condition is assumed to occur when A = 0 at $r = \infty$. However finite element by nature implies a finite domain. A number of finite element methods exist that can be applied to get the solutions that closely approximate the open boundary, which are explained below [100].

2.6.3.1 Asymptotic Boundary Conditions

The asymptotic technique offers a suitable way of approximating an open boundary. Special emphasis is placed on specifying the parameter for a Robin boundary condition [100].

Consider a two-dimension planar problem (circular shell) in polar coordinates of radius r_0 in an unbounded region. As $r \rightarrow \infty$, the magnetic vector potential A goes to zero. On the surface of the circle, the vector is a prescribed function of θ and has an analytical solution of the form

$$A(r,\theta) = \sum_{m=1}^{\infty} \frac{a_m}{r^m} \cos(m\theta + \alpha_m) \tag{2.52}$$

where the a_m and α_m parameters are chosen so that the solution matches the prescribed potential of the outer surface of the circle. The open field solution for large, but not infinite value r is closely described by

$$A(r,\theta) \approx \frac{a_n}{r^n}\cos(n\theta + \alpha_n) \tag{2.53}$$

differentiating with respect to r yields

$$\frac{\partial A}{\partial r} = -\frac{na_n}{r^{n+1}}\cos(n\theta + \alpha_n) \tag{2.54}$$

Solving for a_n in equation (2.54) and substituting into equation (2.54) results in

$$\frac{\partial A}{\partial r} + \left(\frac{n}{r}\right)A = 0 \tag{2.55}$$

Now equation (2.52) is the same form as that of the Robin boundary condition supported by FEMM. If the outer edge of the solution domain is circular and the outer finite element boundary is somewhat removed from the area of primary interest, the open domain solution can be closely approximated by applying equation (2.52) to the circular boundary. The asymptotic boundary conditions for this case may be defined as follows [100]

$$c_0 = \frac{n}{\mu_o r_o} \tag{2.56}$$

$$c_1 = 0 \tag{2.57}$$

2.6.3.2 Kelvin Transformation

The Kelvin transformation technique provides a good approach to open boundary problems which have been extensively discussed in the context of computational magnetics in [97, 98,100]. The strengths of the technique are

- The effects of the exterior region are, in theory, exactly modelled by this approach.
- A sparse matrix representation of the problem is retained (unlike finite element methods, FEM, or BEM methods, which give the same exact solution but densely couples together the boundary nodes).

- Require no special features in the finite element solver to implement the technique, other than the ability to apply periodic boundary conditions.

The far field region of the material is typically homogeneous (e.g. air). The differential equation that describes the magnetic vector equation A is the Laplace equation expessed as

$$\nabla^2 A = 0 \tag{2.58}$$

In polar notation, A is described by

$$\frac{1}{r}\frac{\partial}{\partial r}\left(r\frac{\partial A}{\partial r}\right)+\frac{1}{r^2}\left(\frac{\partial^2 A}{\partial \theta^2}\right)=0 \tag{2.59}$$

assuming that the near-field region of the problem can be contained in the circle of radius r_0 centred at the origin. The far-field region is then everything outside the circle. The unbound region can be mapped onto a bounded region making it easier to solve the problem. This is achieved by defining another variable, R, which is related to r by [100]

$$R = \frac{r_o^{\,2}}{r} \tag{2.60}$$

Then the differential equation may be written as

$$\frac{\partial}{\partial r} = \frac{\partial}{\partial R}\left(\frac{dR}{dr}\right) = -\frac{\partial}{\partial R}\left(\frac{R}{r_0}\right)^2 \tag{2.61}$$

Note $r = R = r_0$

$$\frac{\partial A}{\partial r} = -\frac{\partial A}{\partial R} \tag{2.62}$$

Therefore the differential equation can be written as

$$\frac{1}{R}\frac{\partial}{\partial R}\left(R\frac{\partial A}{\partial R}\right)+\frac{1}{R^2}\frac{\partial^2 A}{\partial \theta^2}=0 \tag{2.63}$$

Thus the transformation equation for the outer region has exactly the same form as the inner region, only in terms of R rather than *r*. This implies that for two-dimension planar problems, the exterior can be modelled simply by creating a problem domain consisting of two circular regions. That is the region that contains the area of interest and the additional circular region representing the far field. Then, periodic boundary conditions are to be applied to the corresponding edges of the circle to enforce the continuity of A at the interface of the two regions.

CHAPTER 3

Modelling the Kinetics of Strain-Induced Nucleation

3.1 Introduction

The martensitic nucleation due to strain-induced transformation provides a platform for correlating the strain with applied load, i.e., the modelling of the volume fraction of martensite as a function of applied load with respect to strain would give the ability to measure and monitor the damage (stress levels) incurred in the SMART aircraft bolt. For this particular application the transformation kinetics limited to strain-induced nucleation, which involves the production of a new nucleation site due to plastic deformation. Several transformation model methods have been discussed by other authors, G B Olson and M Cohen, "Kinetics of Strain-Induced Martensite Nucleation", Metallurgical Transactions, vol. 6A 1975 [101], L Kuafman and M Cohen, "Thermodynamic and Kinetics of Martensite Transformation", Prog in Metal Physics, 7, 165, 1958 [102], J A Vanables ,' Phil. Mag, 7, 35, 1964 [103],Y Tomita and T iwamoto, "Investigateion on Deformation mode dependence of Strain-Induced Martensitic Transformation in TRIP steels and Modelling of Transformation kinetics', Int J Mech. Sci, 40 173,1998 [104]. However, in this dissertation only the Olson and Cohen transformation model is presented due to it's relevance in terms of plastic strain and strain rate.

3.2 Olsen-Cohen Transformation Model

Olsen and Cohen asserted that the shear-band intersection in metastable austenite were the most effective strain-induced martensitic nucleation sites. The operative shear band can be in the form of έ (HCP) martensite, mechanical twins, or dense stacking-fault bundles, which are all promoted by low stacking-fault energy. Martensitic nucleation is based on three factors. These are the course of shear-band formation, the probability of the shear-band intersections, and the probability of the intersection generating a martensitic embryo.

Olsen and Cohen asserted that the incremental increase in the number of shear-band intersections as a function of plastic strain, ε, in the untransformed austenite and assumed that

the shear band constitute a certain fraction of plastic deformation at low strains, but a progressively smaller fraction as the shear-band free energy volume is consumed. The volume fraction of shear band in austenite ($\int^{sb}$) was related to the plastic strain by a relation of the form [101]:

$$\frac{d\int^{sb}}{1-\int^{sb}} = \alpha d\varepsilon \tag{3.1}$$

Alternatively, upon integrating:

$$\int^{sb} = 1-\exp(-\alpha\varepsilon) \tag{3.2}$$

where **α** is a strain-independent constant that represents the rate of the shear-band formation ($df^{sb}/d\varepsilon$) at low strains. The α parameter is however dependant on the stacking-fault energy and strain rate, increasing with decreasing fault energy and increasing strain rate, since both of these factors tend to favour the shear-band mode relative to deformation by slip.

If the shear-band has constant average volume, v^{-sb} the number of shear-bands per unit austenite volume, N_v^{sb} is given by

$$N_v^{sb} = \int^{sb} / v^{-sb} \tag{3.3}$$

N_v^{sb} , therefore increases linearly with strain at low strains and approaches a saturation value at high strains. N_v^{sb} is taken to include shear-bands of all type (ε martensite, twins and stacking-fault bundles)

Next Olson and Cohen suggested that the number of shear-band intersections per unit austenite volume, N_v^I, could be related to number of shear-bands by a simple expression of the form

$$N_v^I = K(N_v^{sb})^n \tag{3.4}$$

where K and n are constants. In this case the shear-band will be randomly oriented for $K = \Pi^2 a^2/16$ and n = 2. However, in general the shear-bands will never be arbitrarily

oriented but tend to be initially parallel until the second order shear system begins to operate, producing an additional shear-band. Thus the numbers of shear band intersections are expected to be initially low and begin to rise rapidly, which is reflected for n values greater than 2 [101].

Since every shear-band intersection has the potential to initiate the nucleation of martensite transformation reaction, an incremental increase in the number of ε martensitic embryos produced per unit austenite volume, $dN_v^{\alpha'}$, with respect to the increase in shear-band intersections is given by an expression of the form:

$$dN_v^{\alpha'} = pN_v^I \tag{3.5}$$

The probability constant p reflects the probability that a shear-band intersection site will generate a martensitic embryo. If the probability is defined in terms of potency value (the minimum chemical driving force required to promote nucleation), then the probability, p, that an intersection will produce an embryo is defined as a Gaussian cumulative frequency function with respect to chemical driving force. Olsen and Cohen further considered the entropy change of transformation to be constant over the temperature range of interest, from which the chemical driving force would be a linear function of temperature and a probability that could be expressed as a Gaussian function of temperature.

It was observed that the growth of martensitic units during strain-induced transformation was confined to the actual shear-bands intersection. The average volume per martensitic unit was considered to be constant, and then the incremental increase of volume fraction of martensite per total volume of alloy was related to the increase in the number of embryos per unit untransformed austenite volume by:

$$\frac{d\int^{\alpha'}}{1-\int^{\alpha'}} = v^{-\alpha'} dN_v^{\alpha'} \tag{3.6}$$

substituting the previous expressions into equation (3.6) and integrating yields the relationship between the volume fraction of martensite and plastic strain as

$$\int^{\alpha'} = 1-\exp\{-\beta[1-\exp(-\alpha\varepsilon)]^p\} \tag{3.7}$$

where

$$\beta = \frac{p\nu^{-\alpha'} K}{\left(\nu^{-sb}\right)^{n}} p \tag{3.8}$$

The α parameter is temperature sensitive through its dependence on the stacking-fault energy. The β is proportional (geometric factors are taken to be insensitive to temperature) to the probability that an intersection will form an embryo and n is a fixed exponent [101].

CHAPTER 4

Material Development And Product Deveolopment

4.1 Introduction

The material development stage took place in several stages. The first stages dealt with the manufacture of TRIP steel alloys for aircraft applications. Four alloys each with their unique chemistry were then tested to establish which alloy composition (material) out of the four alloys possesed the best material properties in terms of material strength as per SPS-B-640 military specifications and ferromagnetic response (transformation characteristics). Subsequently, candidate alloys formulated were destructively tested in tensile, compression, and impact modes. In addition, because of the nature of aircraft flight, the temperature range fluctuates from +40°C down to -50°C in the course of a single flight, thus low temperature performance characteristic were investigated (impact testing). The alloy(s) that achieved the best material results was discovered in this manner. However, this was only the beginning of discovering a smart solution for this application. Further testing of the best candidate alloy was conducted and the results are presented in the product development test results.

4.1.1 Manufacture of TRIP Steel Alloy

The development of a smart aircraft bolt began with the formulation of five different candidate compositions in search of a TRIP steel candidate with the required strength and transformation characteristics. The alloys were manufactured using a 5kg inductance furnace. Plate ingots 68mm thick were cast and allowed to solidify. These were then soaked at 1200°C for a period of one hour.

The ingots were then hot forged down to 37mm thick plates, after which they were again soaked at 550°C for an hour. The 37 mm thick ingot plates where then subjected to a consecutive set of 4% rolled reduction at a temperature of 550°C applied at 5 minute intervals until plates of 600mm x 65mm x 10mm were acquired, representing a 75% warm rolled reduction at 550°C [61]. However, due to the warped geometry of the plates, more work was

required to straighten them. Figures (4.1), pictures I and 2 respectively clearly illustrate how warped the plates were.

Figure 4.1: Warped plates before been straightened

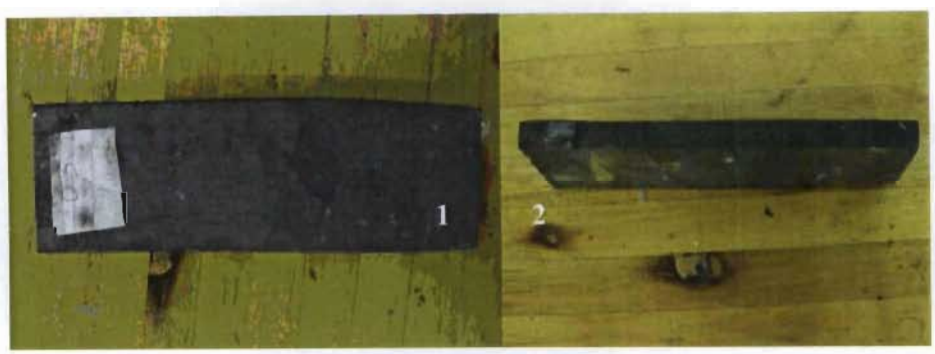

Figure 4.2: Straightened plates that are then cut into strips via laser cutting

The plates were then straightened by warm pressing: the plates were heated at 550°C in the furnace, then removed and placed on blocks which were also heated to 550°C (simply supported with point load applied along the span). A hydraulic press was employed to achieve the straightening of the plates, Figure 4.2. The process was repeated several times along the span of the plate until plate were straightened.Warm pressing was utilized rather than either cold or hot pressing due to the fact that cold pressing would have precipitated phase transformation thus giving a magnetic signature. This would have been a severe disadvantage because this thermal effect would have to be "calibrated" out, requiring substantial data manipulation to obtain a correct damage assessment. The utilisation of hot pressing (above the recrystallisation temperature) would have resulted in a loss of strength as well as transformation characteristics. Once the plates where straightened, they were sent for laser cutting into strips or rectangular bars, which were then machined into the tensile specimens as per SABS standards shown in Figures 4.3 and 4.4 below.

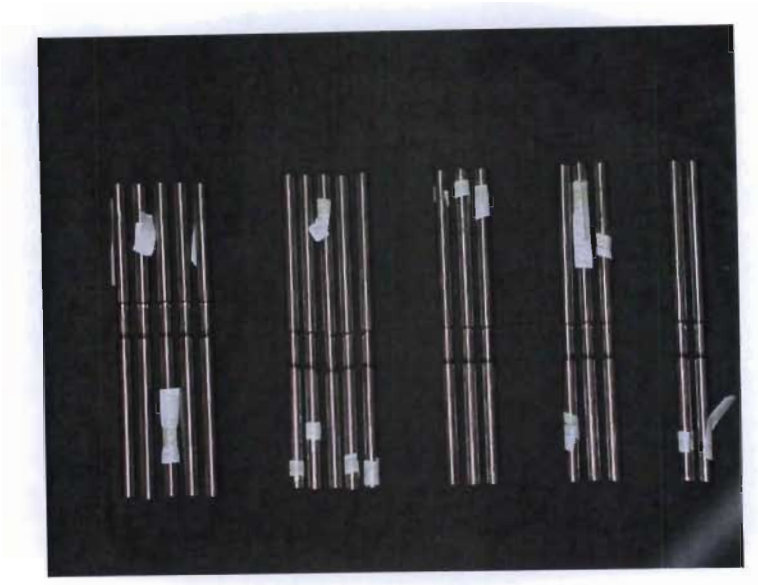

Figure 4.3: Machined tensile test specimens [61]

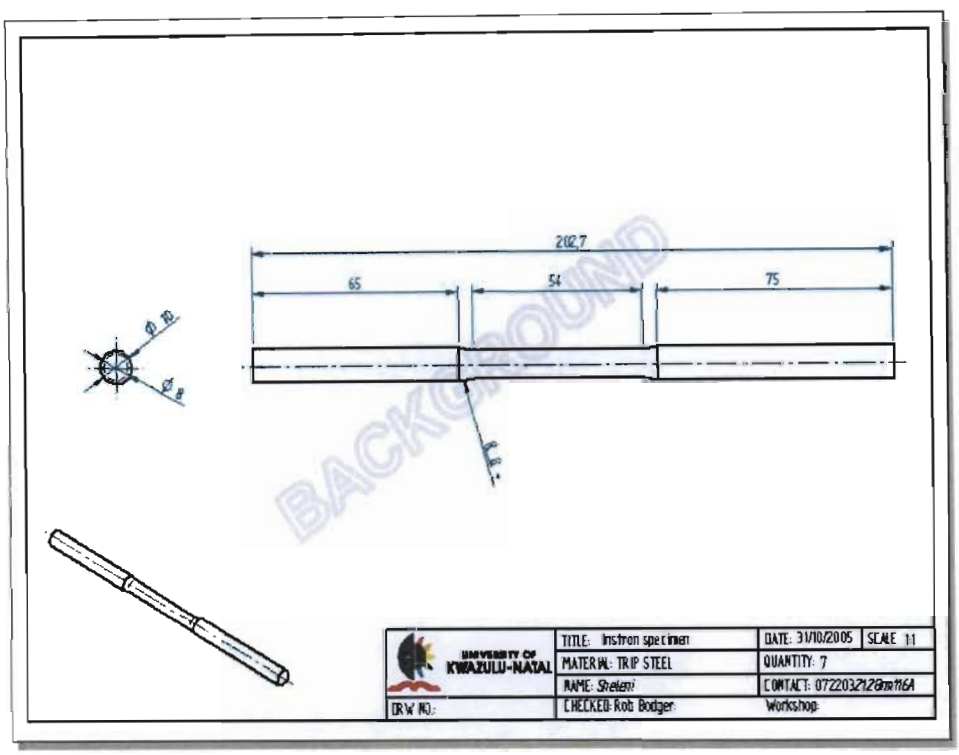

Figure 4.4: Line drawing for a tensile specimen [61].

The magnetic susceptibility of the alloy plates was measured both before the warm pressing and after the pressing process. This was also done for both the laser and machining processes as shown in the Table 4.1 below.

Table 4.1: Comparison of magnetic susceptibility between alloys [61]

Alloy ID	Before Warm Pressing (μH/m)	After warming (500°C)Pressing (μH/m)	After laser Cutting (μH/m)
Alloy 1 Sample 1	0.560 - 0.650	0.500 - 0.640	0.270
Alloy1 Sample 2	0.040 - 0.070	0.065 - 0.075	0.070
Alloy 2 Sample1	0.330 - 0.350	0.240 - 0.075	0.150
Alloy 2 Sample 2	0.077 - 0.085	0.095 - 0.099	0.099
Alloy 3 Sample 1	0.090 - 0.140	0.080 - 0.090	0.090
Alloy 3 Sample 2	0.030 - 0.039	0.031 - 0.034	0.034
Alloy 4 Sample 1	0.000 - 0.052	0.000 - 0.052	0.053
Alloy 4 Sample 2	0.036 - 0.046	0.039 - 0.041	0.041

4.1.2 Chemical Analysis

Several melts for each alloy composition were proposed. The difference between the proposed percent mass chemical compositions and that of actual percentage mass chemical composition are shown in Table 4.2 below for both the 2nd and 3rd generation melts conducted by Scooby laboratory (appendix C). Note that the carbon content for the third generation were much better than the second generation which was attributed to vacuum melt employed.

Table 4.2: Illustrates the difference in the chemical composition between the proposed target, 2nd and 3rd generation melt of TRIP steels alloys [61]

	Alloy1			Alloy2			Alloy3			Alloy4		
Element	Target	2nd	3rd	Target	2nd	3rd	Target	2nd	3rd	Target	2nd	3rd
C	0.35	0.16	0.3	0.3	0.21	0.33	0.25	0.19	0.2	0.35	0.29	0.35
Mn	3.5	4	3.86	2.1	2.57	2.63	10	10.5	10.14	1	1.13	1.64
S	0	0.007	0.015	0	0.006	0.016	0	0.01	0.014	0	0.007	0.012
P	0	0.005	0.011	0	0.005	0.013	0	0.005	0.011	0	0.005	0.011
Si	0.5	0.53	0.61	0.5	0.6	0.44	0	0.08	0.068	0.5	0.56	0.58
Cr	9	8.14	9.09	8.5	8	8.75	12	11.6	9.66	12	11.6	11.95
Mo	0	0.03	0	2	1.91	1.7	0	0.03	0.013	0	0.01	0.002
Ni	8	8.31	6.3	8.4	8.91	8.49	1.5	1.33	1.86	9	9.48	8.89
Cu	0	0.01	0	0	0.01	0	0	0.01	0	0	0.033	0
Al	0	0.014	0	0	0.015	0	0	0.031	0	0	0.000	0
V	0	0	0	0	0	0	0	0	0	0	0	0
Nb	0	0	0	0	0	0	0	0.026	0	0	0.025	0
B	0	0	0	0	0	0	0	0	0	0	0	0
Ti	0	0	0	0	0	0	0	0	0	0	0	0
Fe	Matrix	Matrix	Matrix	Matrix	Matrix	Matrix	Matrix	Matrix	Matrix	Matrix	Matrix	Matrix

4.1.3 Mechanical Testing of Aircraft Materials for Candidate Smart Bolt

The first criteria that any material for an aircraft bolt must meet, is that of strength. For a smart bolt, the additional factor of the transformation characteristic must be considered. The first set of tests to which the material was subjected, were therefore the tensile test coupled with magnetic susceptibility monitoring to ascertain the transformation onset point as well as the rate of transformation.

4.1.4 Tensile Testing

The phase change from paramagnetic state (parent phase) to ferromagnetic state (martensitic product phase) was monitored and recorded by a GMS-2 magnetic susceptibility meter. The meter was designed for geological purposes to measure the magnetic susceptibility of rocks and drilled core. An evaluation test was conducted to see whether the meter would pick up the magnetic reading for tensile specimens and how far apart the meter had to be from the specimen. It was noted that the effectiveness of measuring susceptibility decreased with increasing distance from specimen gauge length, as seen in Figure 4.5 below.

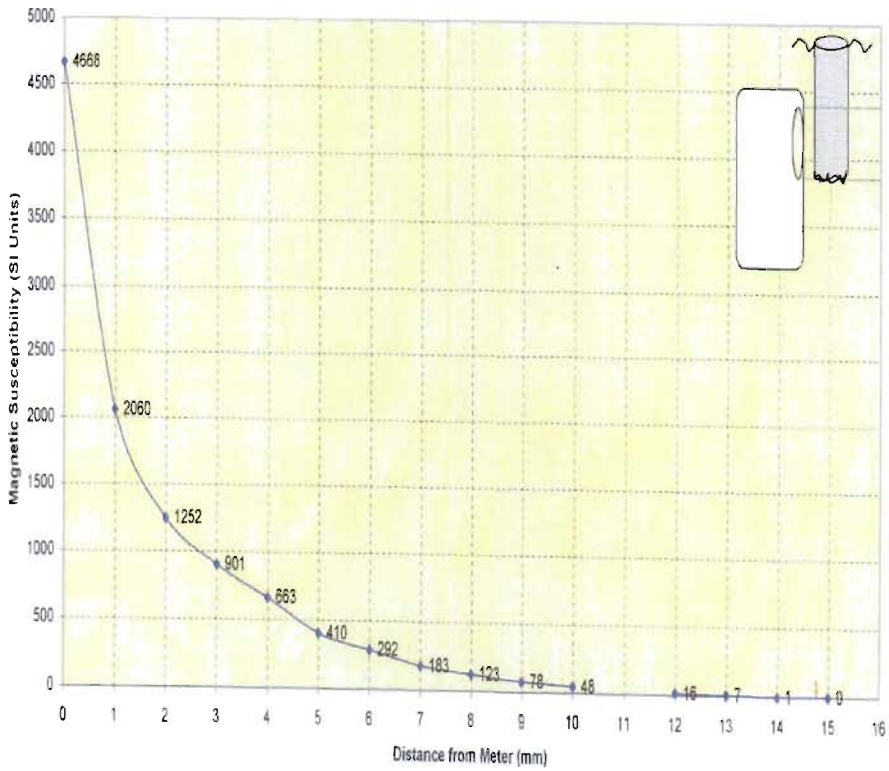

Figure 4.5: Illustrates the effect distance has on the magnetic susceptibility sensitivity

To overcome the problems of effective reading with regard to distance a clamp was designed onto which the GMS meter was mounted on, as close as possible to the central region along the gauge length (prismatic section) of the specimen. The bracket was mounted at the bottom of the crosshead, which held the meter in a permanent position so that accurate and non-diverging readings of susceptibility were recorded. Data was captured by the host computer in real time through the integration of the susceptibility meter and a desktop computer by a RS-232 serial port. The magnetic susceptibility was recorded for every 0.001 unit of strain reading. Figure 4.6 below shows how the susceptibility meter is mounted near the prismatic region, together with the extensometer between the test grips.

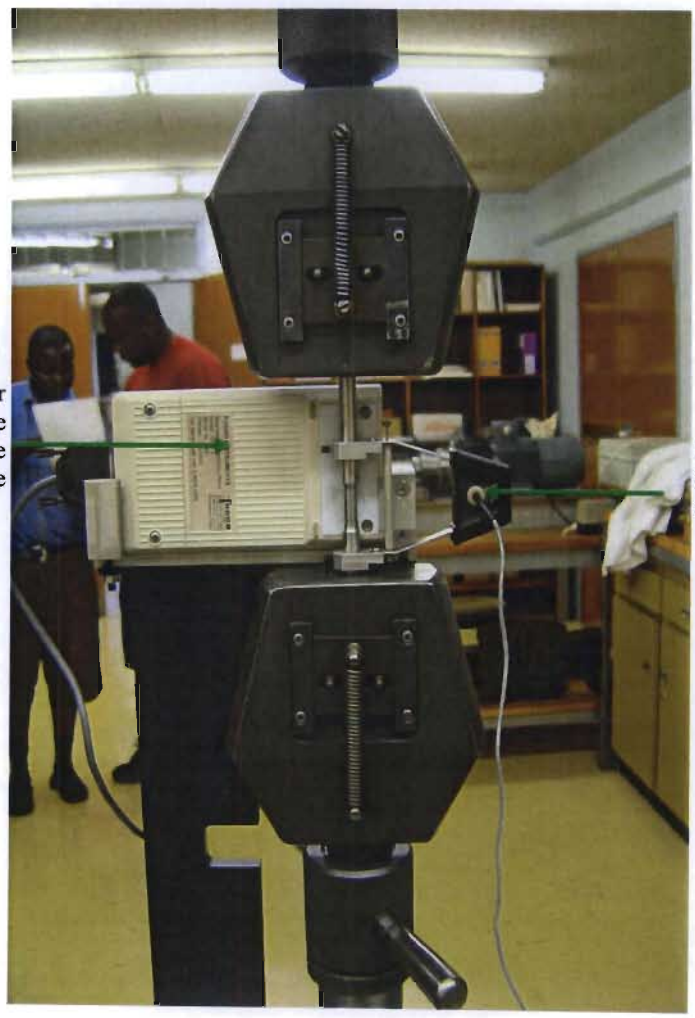

Figure 4.6: Setup of the extensometer, magnetic susceptibility and the tensile test specimen in between the Instron test grips.

The Instron test rig model 5555R was used to determine the tensile properties of the TRIP steel materials. It operated with a 100kN load cell, with frame structure rated at 80kN, the data recording and the test parametric setting (test speed of 0.5mm/min, specimen geometric

dimensions, recalibration of load cells and extensometer) were all carried out from the computer integrated with the Instron through a PLC. Figure 4.7 depicts the full specimen installation in between the two test grips (also shown in Figure 4.6), the magnetic susceptibility meter mounted on the bracket, which is clamped securely by two bolts at the bottom of the Instron crosshead and control panel used to jog the cross head up or down during specimen installation, together with an emergency button to abort testing in the event of a catastrophe.

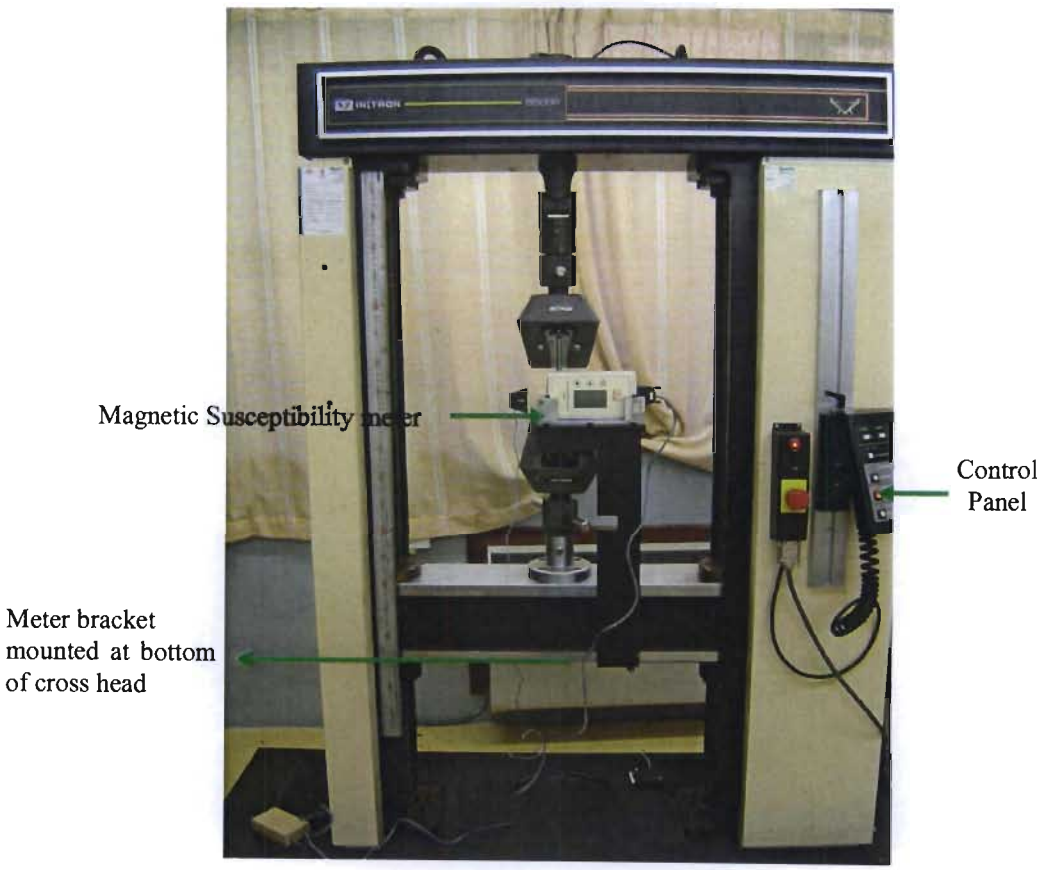

Figure 4.7: Full specimen installation configuration on the Instron testing machine

The magnetic susceptibility was then correlated to the strain, which in turn gave an indication of how much damage was induced in the specimen.

4.1.5 Impact Testing

Once the tensile testing was completed, the material that met the strength criteria as well as displaying transformation within the elastic strain range (and therefore possessed the inherent ability to detect damage before yielding) were then subjected to impact testing to deduce the energy absorption ability of the TRIP steel alloys.

A set of Charpy test specimens were machined from successful alloys according to SABS 056-1973 standard. These were then impact tested through a temperature range of negative 50°C to positive 50°C, as this is the range in which the aircraft bolts typically operate, stipulated by SPS-B-640 military standard for AC 130 aircraft. The first three specimens from each alloy were subjected to -50°C impact testing and later three were tested at room temperature 20°C. The charpy specimens were tested for their magnetic susceptibility prior to and after testing. It was clear from the result that martensite nucleated due to impact at both temperatures. It was however important to determine whether this martensite nucleated spontaneously (at sub zero temperatures due to normal thermal transformation) or whether the impact was the sole cause of martensic nucleation, and a further set of experiments was designed.

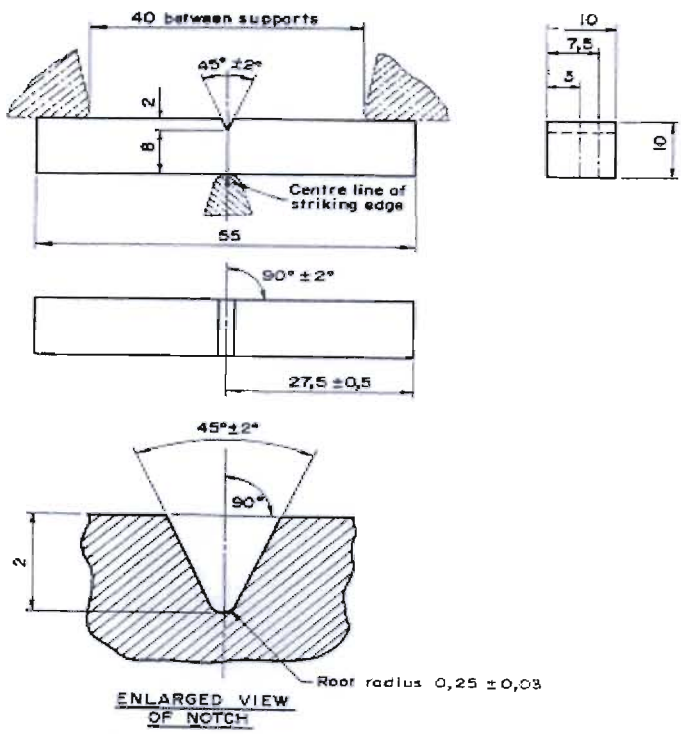

Figure 4.8: Drawing of an Impact test specimen as per SABS 056-1973 Standard

Further analysis was carried out on another set of specimens to determine whether the alloys transformed, by testing them with dry ice (cooling the specimen from 20°C to -85°C). Again the magnetic susceptibility was recorded at various temperature levels. These results are presented in the next chapter.

4.1.6 Metallurgy and Microscopy

A microstructure analysis was carried out to correlate magnetic susceptibility readings with the volume percentage matensite. The cutting of plate and tensile samples for micro-structural analysis was achieved with an Imptech Europe Abrasive cutter fitted with a soft silicon carbide abrasive cutting wheel, to avoid any influence on transformation kinetic from austenite to martensite due to work hardening that would be associated with ordinary cutting operations.
A set of unstressed machined samples were then subjected to Rowell C hardness tests and Vickers hardness tests. The hardness results obtained were used to deduce the appropriate metalog (grinding and polishing) method to be utilized. The (Struers) Metalog Method D was recognized to be the best method to use and the specimens were then mounted in a multi fast phenolic hot mounting resin using a Struers Labopress 3 mounting machine. The mounted specimens were ground and afterwards polished using the Motopol 2000 machine. The grinding of the samples was carried out as follows.

The samples were ground using a 6 μm diamond abrasive paper, which had a MD-piano 160 surface. Water was utilized as a lubricant and the machine was run at 300 rpm using a force of 180N applied for four minutes. The some procedure was repeated with minor changes such as the MD-piano 160 surface was replaced by Nap-less Nylon Cloth, which was used with a 1μm grain size diamond paste and blue lubricant instead of water. The polishing was conducted in a similar format; the first polishing stage utilised medium nap cloth and a colloidal silica or alumina (Al_2O_3) suspension of 3μm grain size at a speed of 150 rpm at force of 180N for a 4 minutes period. During the second stage of fine polishing the force and time period where reduced to 90N and 2 min respectively. At each polishing interval the samples were washed with soap, running water then rinsed with Methanol. This prevented water staining.

The polished samples were then etched using either Kalling, 1 solution (1.5g $CuCl_2$. 33ml Ethanol, 33ml HCl and 33ml H_2O) or a solution mixture of Vilella's reagent, picric acid 1g and 1-2 drops of Nitric acid. This was conducted at room temperature for a 10 second period. Once this was done the samples were microscopically examined to deduce whether martensitic nucleation occurred at the shear band intersections, as this is the most likely site for the development of an active martensitic nucleus/embryo.

The polishing and etching methods presented here were used for all the test specimens presented in this thesis. The results are presented in sections 4.2 and 4.4.

4.2 Material Development Experimental Test Results

The selection of the chemistry for the four alloys was based more importantly on their strength criteria and transformation characteristics required for material required to act as a strain memory alloy. Other factors such as corrosion, impact resistance, oxidation resistance, decarburization resistance and temperature effect were considered. The selections of the chemistry of the four alloys have been documented by Dr B l Verijenko and Dr J M v Vugamporee [52, 61]. The proposed targets for each (chemical composition) alloy were based on the following:

For alloy 1, whose chemical composition, **Fe-9.00Cr-8.00Ni-3.50Mn-0.50Si-0.35C**, was calculated to have a chromium equivalent, C.E equal to 10 and a nickel equivalent N.E equal to 20. Therefore from the Schaeffer-de Long diagram Figure 4.9, it was clearly noted that alloy 1 was situated in the austenitic region which meant that alloy 1 had an austenite parent phase and would be metastable after the alloy was warm-worked but would still be able to phase transform. The high content of 0.35%C and 0.5%Si would ensure that the alloy had a high strength and corrosion as per SPS –B-640 military standards for aircraft fasteners [61].

Alloy 2: chemical composition **Fe-8.5Cr-8.4Ni-2.10Mn-2.0Mo-0.5Si-0.3C** was calculated to have a chromium equivalent, C.E equal to 11.3 and a nickel equivalent, N.E equal to 18.4.This meant that from the Schaeffer- de Long diagram alloy 2 was also an austenite based alloy in its parent phase before transformation. From figure 4.9 it can be seen that the alloy is situated in austenite region close to the SM region, as indicated in chapter 1, Figures 1.2 and 1.3. The %C, %Cr and %Ni content where all reduced by 0.05%, while the %Mn was reduced by 1.4%. However, the %Mo was increased by 2%. (this is generally a strengthener and ferrite stabilizing element).The 0.30%C, 2%Mo and 0.50%Si would be enough to give alloy 2 a higher possibility for transformation to occur and high strength criteria for a material required to manufacture an aircraft bolt [61]

Alloy 3: chemical composition **Fe-12.00Cr-1.50Ni-10.00Mn-0.25C** was calculated to have chromium equivalent, C.E, equal to 12, and nickel equivalent, N.E, equal to 14 which placed it in the austenite region seen from the Schaeffer-de Long diagram, Figure 4.9. Like the previous alloys, alloy 3 should be metastable in its parent austenite phase and should readily undergo phase transformation under straining and meet strength criteria required as per SPS –B-640 military standards for aircraft fasteners. In addition, alloy 3 has a higher % Cr, 12% Cr and a low 1.5% Ni added to avoid any stress assisted transformations. However alloy 3 is manganese

based alloy and manganese tends to support cracking in metals during warm working and cold working operations. This would make it difficult to machine [61].

Alloy 4: chemical composition **Fe-12.00Cr-9.00Ni-1.00Mn-0.50Si-0.35C** is calculated to have chromium equivalent (C.E) equal to 13 and a nickel equivalent (N.E) equal to 20. Thus from the Schaeffer-de Long diagram, it was deduced that the alloy was situated in the austenitic region above SM region. Therefore alloy 4 would have a metastable austenite parent phase and be able to transform to the martensitic product phase. The high percentage chromium of 12%C ensures that the alloy has a high degree of corrosion resistance and the content of 0.35%C and 0.5%Si should give alloy 4 a good material strength capability. Figure 4.9 below displays the. Schaeffer-de Long diagram used to deduce the alloys parent phase

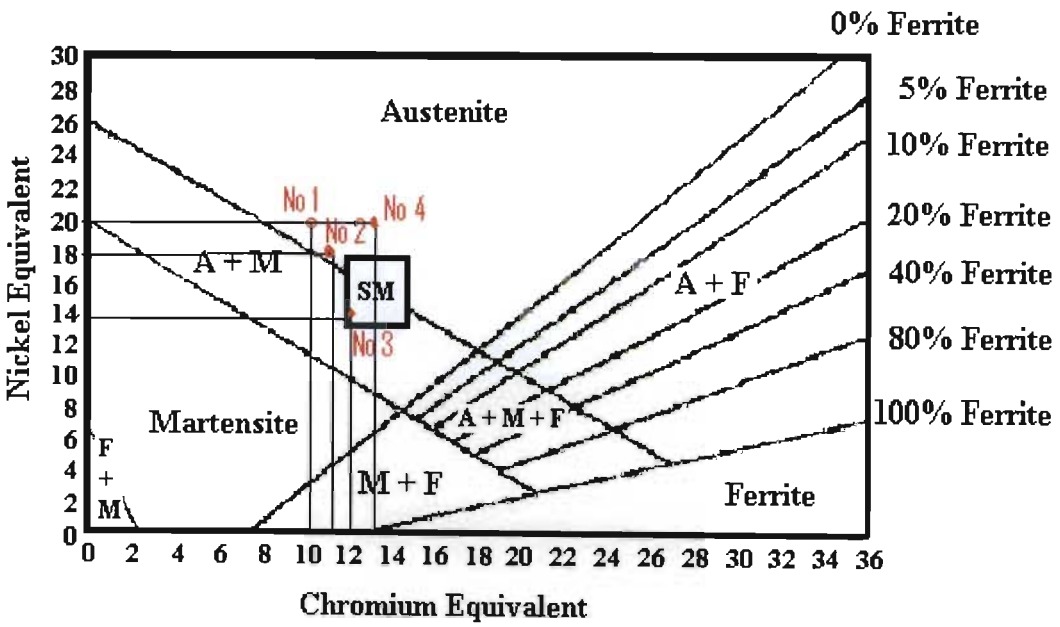

Figure 4.9: Schaeffer de Long diagram showing location of selected strain memory alloys [61]

The selection of the candidate alloy or alloys for the smart aircraft bolt was based on the overall performance displayed by the best of the four different TRIP steel alloys [61]. Each alloy had a unique chemical composition, which gave them their distinctive mechanical and transformation (ferromagnetic response) properties under tensile, compression, fatigue and temperature loading conditions. Tables 4.1 and 4.2 revealed the divergence of the actual chemical composition of each alloy (2nd and 3rd generation) from the desired formulated target. The carbon content for all

the alloys was lower than expected. Each generation of material was subjected to exactly same the testing procedure, be it tensile testing or fatigue testing.

The results obtained from the experimental testing of each alloy are presented for both the second and third generation [61]. The martensite precipitated due to strain-induced martensitic transformation is represented by the ferromagnetic response of material, i.e., the ferromagnetic response was defined as the degree of magnetism present within the material, which was measured using a magnetic susceptibility meter or inductance meter. The graphs below show the relationships that have developed between the stresses (represented by blue curves) and magnetic susceptibility (represented by the purple curves) with respect to strain, for any strain level. The same method of displaying results is continued throughout section 4.2

The brown straight line that intersects the stress and magnetic susceptibility curves at a specific strain shown in the graphs illustrates the point at which the yield strength of the materials was reached. Also at this point any change in strain-induced phase transformation, that is, the ferromagnetic response of the material that occurred was recorded. This helped to differentiate the transformation that occurred before elastic yield point and after plastic yield. The results from the experimental tensile tests are expressed in the graphs below:

4.2.1 Experimental Test Results for Alloy 1

Table 4.3 : Differences in % chemical; composition between the desired target, 2nd generation and 3rd generation TRIP steels for alloy 1 [61]

Element	C	Si	Mn	P	S	Cr	Mo	Ni
Desired target	0.35	0.5	3.5	0	0	9	0	8
Alloy 1, 2nd	0.16	0.53	4	≤0.005	0.007	8.14	0.03	8.31
Alloy 1, 3rd	0.3	0.61	0.86	0.011	0.015	9.09	0	6.3

The ferromagnetic response behaviour for both the 2nd and 3rd generations are presented in Figures 4.10 and 4.11. Table 4.4 below gives an overview of the mechanical properties and the ferromagnetic response (magnetic susceptibility) of the TRIP alloys.

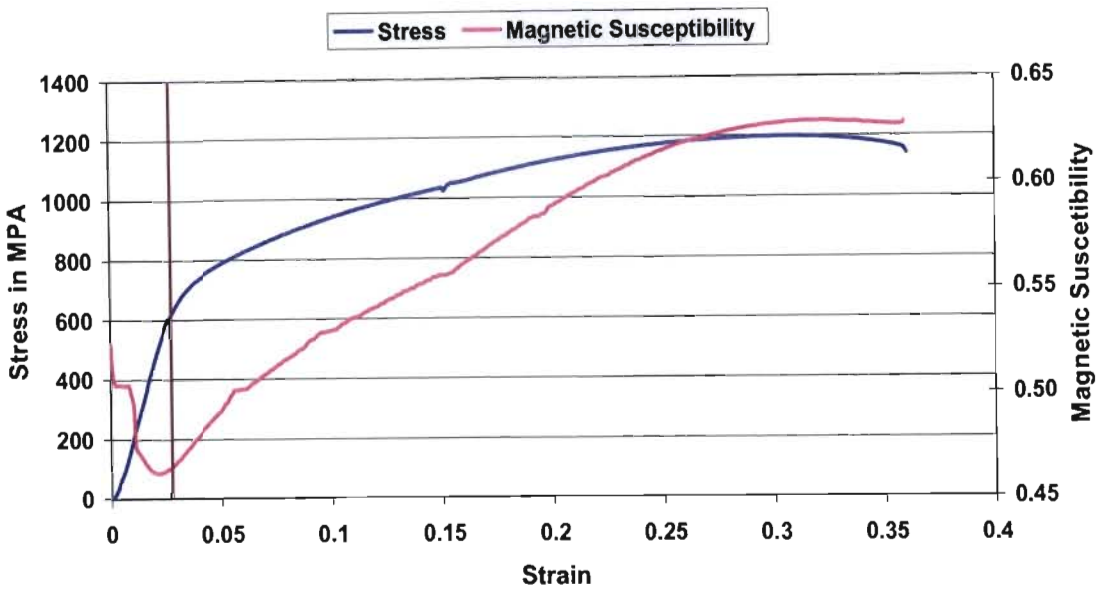

Figure 4.10: A typical example of a stress-strain curve and magnetic susceptibility-strain curve for the 2nd generation of alloy, tensile tested sample 3 [61]

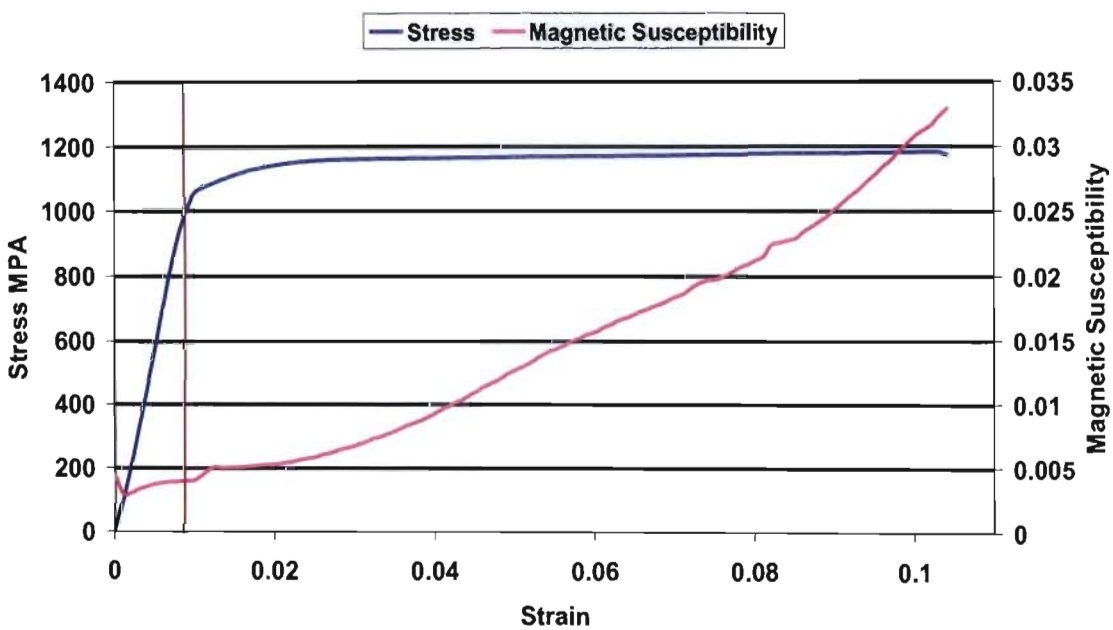

Figure 4.11: Typical example of a stress-strain curve and magnetic susceptibility-strain curve for the 3rd generation of alloy, tensile tested sample 3 [61]

Table 4. 4: Overview of the mechanical properties and the ferromagnetic response (magnetic susceptibility) of the TRIP alloys [61]

Melts NO:	75% Reduction	Tensile Yield Strength MPa	Ultimate stress MPa	% Elongation	Initial magnetic Susceptibility	Final magnetic Susceptibility
2^{nd}	75	790	1190	36	0.525	0.625
3^{rd}	75	1072	1181	10.5	0.001	0.006

Samples were cut off the tensile tested specimen in areas close to where the fracture of the tensile specimen occurred. The specimens were then ground, polished and finally etched using kalling 1 for a 10 second period and the microstructure was analysed. Figure 4.13 shows the microscopic structures of the 2^{nd} and 3^{rd} generation melts taken at 400X optical magnification. The SEM image of the 2^{nd} generation alloy in picture A shows elongated dark strip regions representing the martensitic regions, while the very light grey represents retained austenite. Picture B in Figure 4.13 displayed dark brown strip regions of martensite along slip planes of the 3^{rd} of alloy 1. In addition, the microstructure of Figure 4.13 displays similar elongation of the martensitic and austenitic grains along slip planes, oriented to the same direction as that of the rolling direction which in turn revealed strain-induced transformation occurred for both the 2^{nd} and 3^{rd} generation alloy 1, also taken at 400X optical magnification, left to right respectively [61]. The results of the metallographic analysis of the microstructure for each tested specimen for both generations are represented in Figures 4.12 to 4.13 below

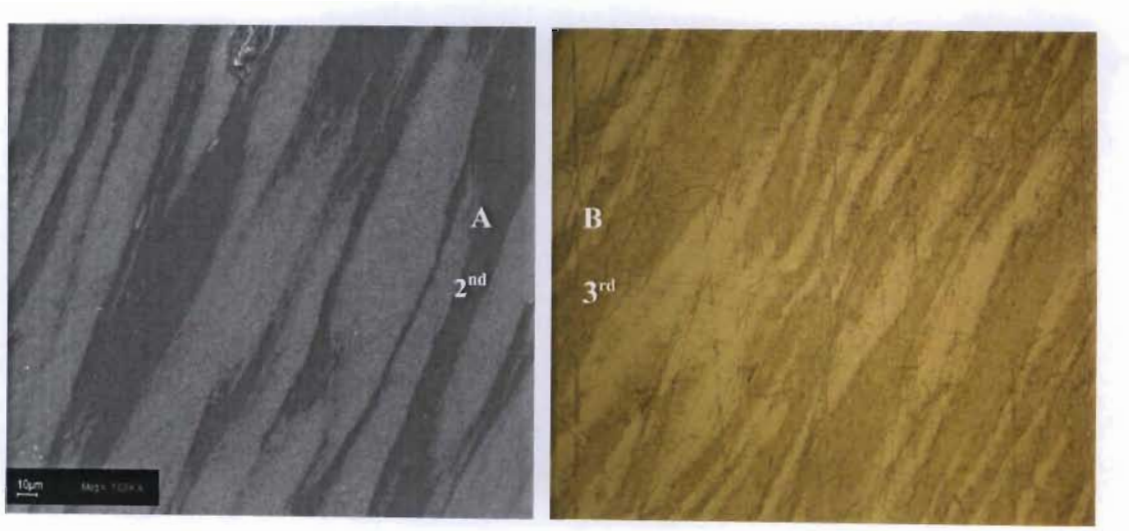

Figure 4.12: Microstructure for 2^{nd} and 3^{rd} generation melts of alloy 1 (400X) magnification, martensitic precipitation along grain boundary with return austenite, left to right respectively [61]

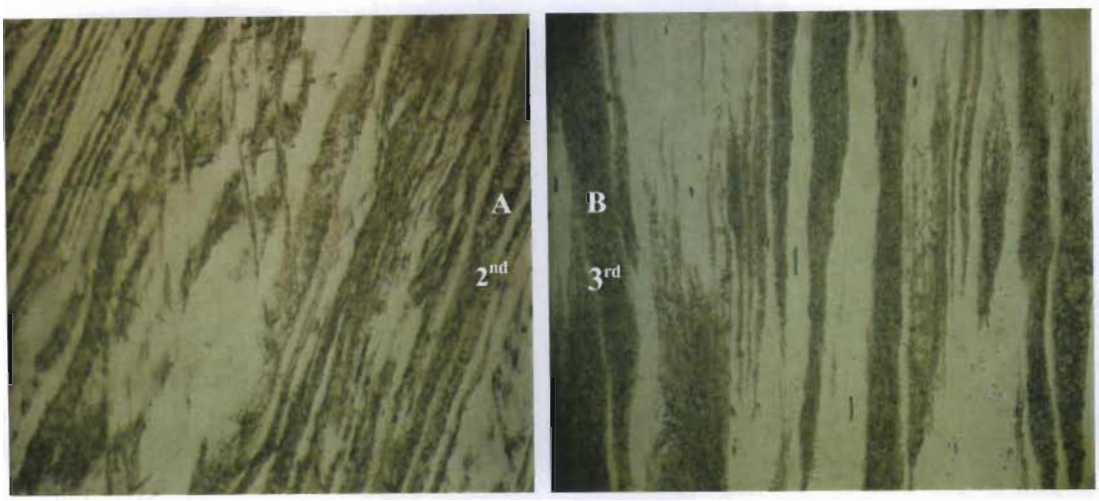

Figure 4.13: Microscopic structures of both the 2nd and 3rd generation melts show elongated darkish black strip regions represent the martensitic regions, with retained austenite, light grey areas tensile tested specimen [61]

4.2.1.1 Conclusion

The experimental data from the tensile testing of the 2nd generation for alloy1 showed that the yield strength level registered was below that required for an aircraft wing bolt application and the material did not display any form of strain hardening. The magnetic susceptibility registered due to strain-induced martensitic transformation was also observed to be lower and was initiated at a strain level which corresponded to a region around the elastic limit and in some instance the phase transformation occurred only when the material experienced plastic deformation. This meant it would always be difficult to accurately detect any form of initial damage (for instance any form of initial crack initiation due to fatigue); this meant that 2nd generation alloy 1 was not favourable as a smart strain memory structural sensing component. In addition, from Table 4.3 the percentage carbon content in the alloy 1, 2nd generation of 0.16 was less than that proposed by required target (0.35). The low percentage carbon content meant that in general the material was weaker in terms of strength. This was initially attributed to the decarburization of the material from the thermo-mechanical processing of the TRIP steel alloy material. Table 4.3 further illustrated that there was little strain-induced martenstic precipitated, represented by the small difference between final magnetic susceptibility and the initial magnetic susceptibility reading.

Results for the 3rd generation differed from those of 2nd generation in that the yield strength of the material was higher, which meant that the 3rd generation was much stronger (Table 4.4). This was due to the carbon content being only slightly less than the stipulated target. This also meant that the chemical composition was not heavy affected by the thermo-mechanical processing, but rather by melting conditions. From Figures 4.10-4.11 it was clear that phase transformation (magnetic susceptibility vs. strain) occurred within the elastic region. However, most of it took place in the plastic deformation region. The results deduced from metallographic analysis revealed that the 3rd generation material had a better ferromagnetic response as shown in the Figures 4.12 to 4.13 where the much darker regions of martensite precipitated along the slip planes implied a greater precipitation of martensite than that noted for the 2nd generation melt. However, the transformation characteristics combined with insufficient yield strength precluded the use of alloy 1 as a candidate and it was eliminated from further testing.

4.2.2 Experimental Test Results for Alloy 2

As for alloy 1, the second generation melt of alloy 2 displayed considerably depleted carbon content with the third and target chemistries. Figures shows typical stress-strain and strain susceptibility relationship for the 2nd and 3rd generation melts of this alloy

Table 4.5: Differences in % chemical; composition between the desired target, 2nd generation and 3rd generation TRIP steels for alloys 2 [61]

Element	C	Si	Mn	P	S	Cr	Mo	Ni
Desired target	0.35	0.5	3.5	0	0	9	0	8
Alloy 2, 2nd	0.21	0.60	2.57	0.005	0.006	8.00	1.91	8.91
Alloy2, 3rd	0.33	0.44	2.63	0.013	0.016	8.75	1.70	8.49

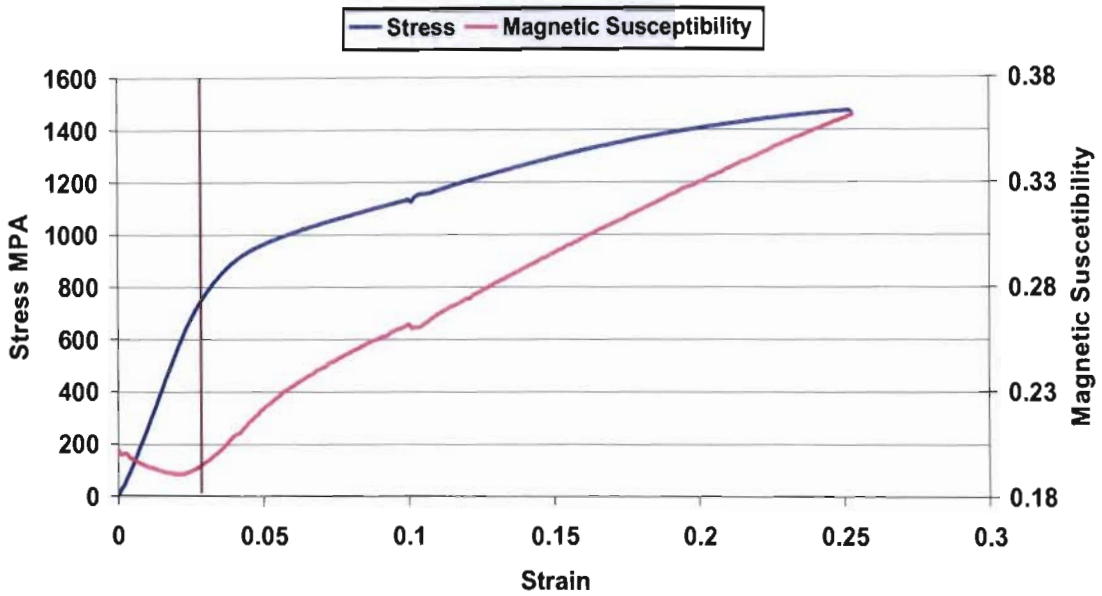

Figure 4.14: **Stress-strain and magnetic susceptibility-strain of the 2nd generation melt 2 [61]**

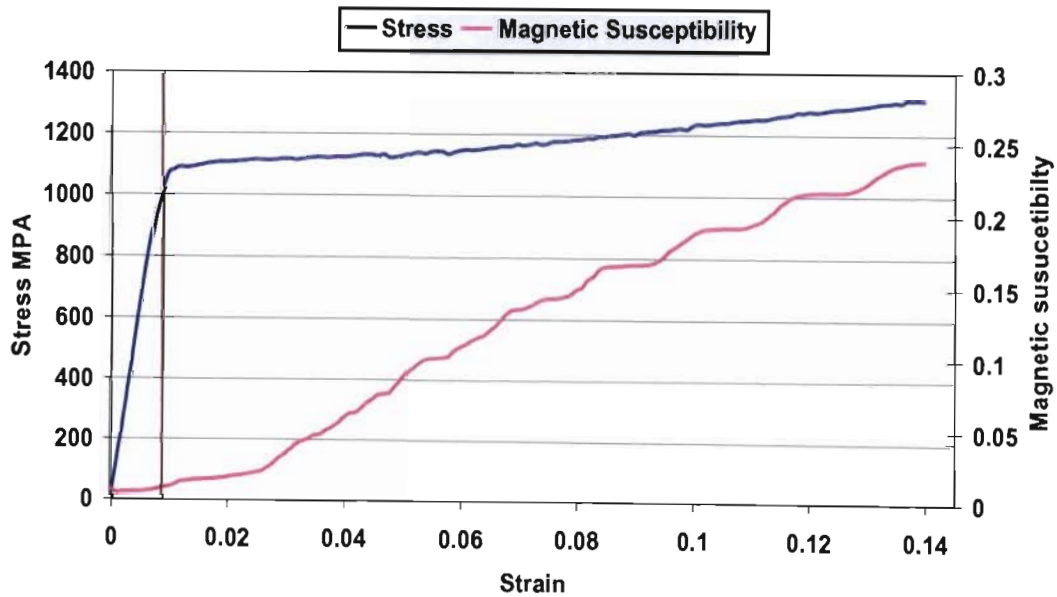

Figure 4.15: **Stress-strain, magnetic susceptibility-strain curve for the 3rd generation alloy 2 [61]**

Table 4.6: Mechanical properties and the ferromagnetic response (magnetic susceptibility) of the TRIP alloys 2 [61]

Melt NO:	75% Reduction	Tensile Yield Strength MPa	Ultimate stress MPa	% Elongation	Initial magnetic Susceptibility	Final magnetic Susceptibility
2nd	75	900	1500	25	0.175	0.375
3rd	75	1100	1315	14.5	0.00	0.025

Figure 4.16 displays no form of localised necking along the prismatic region of both the unfractured tested specimen of the 2nd generation of alloy 2 and the fractured sample of the 3rd generation in pictures, A, and B respectively.

Figure 4. 16: No form of localised necking along prismatic region for both 2nd and 3rd generation TRIP steel alloys [61]

The encouraging results from tensile testing (good yield strength. UTS and elongation) coupled with the good range of change in magnetic susceptibility prompted further testing of alloy 2. Figure 4.17 illustrates the correlation developed between magnetic response and applied varying stress loads, for the compression test specimen of the 2nd generation alloy material. Like the tensile test results acquired in terms of ferromagnetic response to stress, the phase transformation from parent paramagnetic austenite to a metastable product ferromagnetic martesitic phase was reached well within the elastic region.

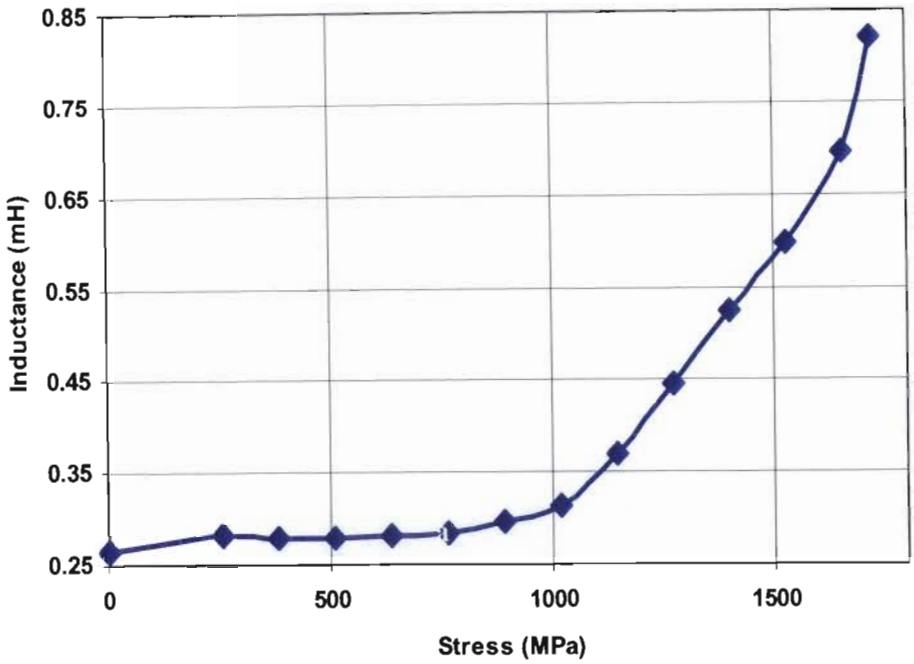

Figure 4.17: illustrates the correlation developed between the Inductance and stress of the compressed specimen of the 2nd generation of alloy 2 [61]

Samples were then cut off each tested tensile specimens (2nd and 3rd generation alloys) from which their microstructure was deduced. Figure 4.18 shows an SEM image of the microstructure of the 3rd generation alloy material taken at 400 X magnification. Picture B. clearly displays elongated darkish strip regions representing the austenite regions, while the very pale grey regions represent the martensitic region. Picture A in Figure 4.18 shows dark brown strip regions of martensite with retained light brown regions of austenite for 2nd generation alloy 2. The Figure 4.19 shows the two microscopic structures for specimens for both the 2nd and 3rd generations taken at 400X magnification, represented by the pictures, A, and B respectively. The pictures clearly indicated martensitic and austenitic elongations along the slip bands, oriented in the same direction to that of the rolling direction, which confirmed that transformation occurred. The microscopic structures for both generations are presented as follows:

Figure 4. 18: Microscopic structures of both the 2nd and 3rd generation for both compressed specimen and tensile tested specimen in pictures, A, and B respectively, taken at a magnification of 400 X [61]

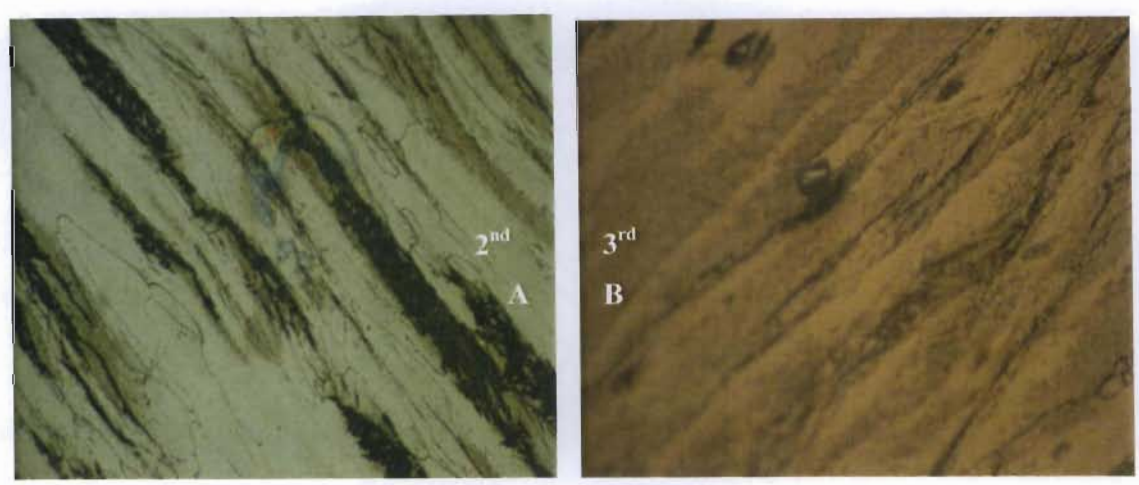

Figure 4. 19: Microscopic structures of both 2nd and 3rd generation alloys showing dense dark strips of martensitic precipitation, with retained austenite for tensile tested specimens [61]

The results obtained from both tensile and compression testing revealed that both magnetic susceptibility-strain responses and stress-strain relationships ranked this alloy as a very promising candidate material for the smart aircraft bolt application. Impact testing was carried out on 2nd generation alloy through a temperature range of 70°C (20°C to -50°C) and the magnetic susceptibility was measured before and after testing. The results of these are presented in tables 4.7 and 4.8.

Table 4.7: Fracture toughness of the 2nd generation alloy [61]

ID	Lateral Expansion		Shear	%	Fracture	Toughness J
	20°C	At -50°C	20°C	At -50°C	20°C	At -50°C
2nd Alloy 2	0.43	0.18	100	100	50	88
	0.48	0.27	100	100	60	78
	0.61	0.33	100	100	62	87

Table 4.8: Ferromagnetic response in terms of magnetic susceptibility at varying temperature [61]

Magnetic Susceptibility before Impact (20°C)	Magnetic Susceptibility before Impact (-50°C)	Magnetic Susceptibility after Fracture (20°C)	Magnetic Susceptibility after Fracture (-50°C)
0.009298	0.01883	0.01484	0.02545
0.00636	0.0226	0.01010	0.02929
0.00397	0.02212	0.08876	0.03006

Figure 4.20 displays two photographs. In picture A the fracture that was displayed was pure shear at room temperature. At sub zero temperatures (-50°C) the fractures surfaces of the specimen displayed a massive v- notch brittle fracture failure.

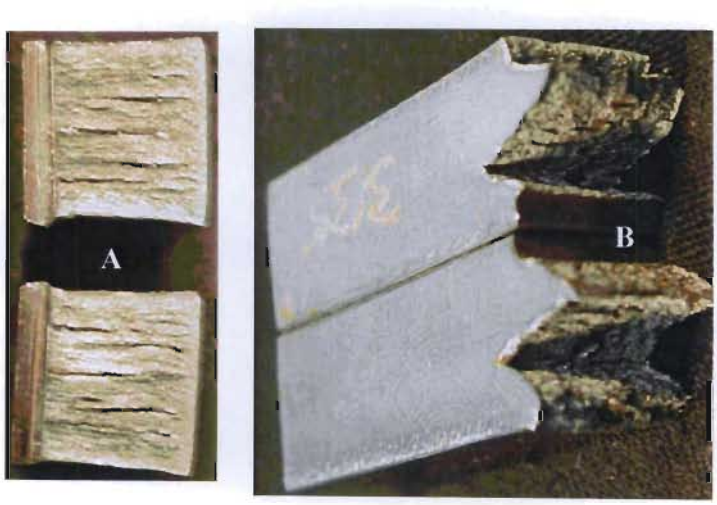

Figure 4.20: Shear failure in picture, A, at room temperatures, while at sub zero temperatures (-50°C) test specimen displayed a brittle failure mode shown in picture B, of the 2nd generation alloy material [61]

It is important to ascertain whether the usual athermal martensitic precipitation reaction occurs in this alloy within the service temperature range of -50°C (maximum altitude) to +50°C (sitting on the runway). If the athermal martensite does precipitate spontaneously, this would obviously severely complicate the correlation between the magnetic susceptibility and the strain induced damage. Further testing was therefore conducted to learn what the effects of temperature changes will have on an aircraft bolt material, particularly at sub zero temperatures for the bolts that were to be used to attach the aircraft wing to fuselage during taxing, in flight-service and landing. Further testing was conducted on two test specimens cut from the 2nd generation alloy 2 material. These samples where labelled A and B respectively and the test was conducted using dry ice. This was done in order to deduce the transformation characteristics (magnetic susceptibility) of the material at subzero temperatures in dry ice, which is illustrated by Figures 4.21 and 4.22 respectively.

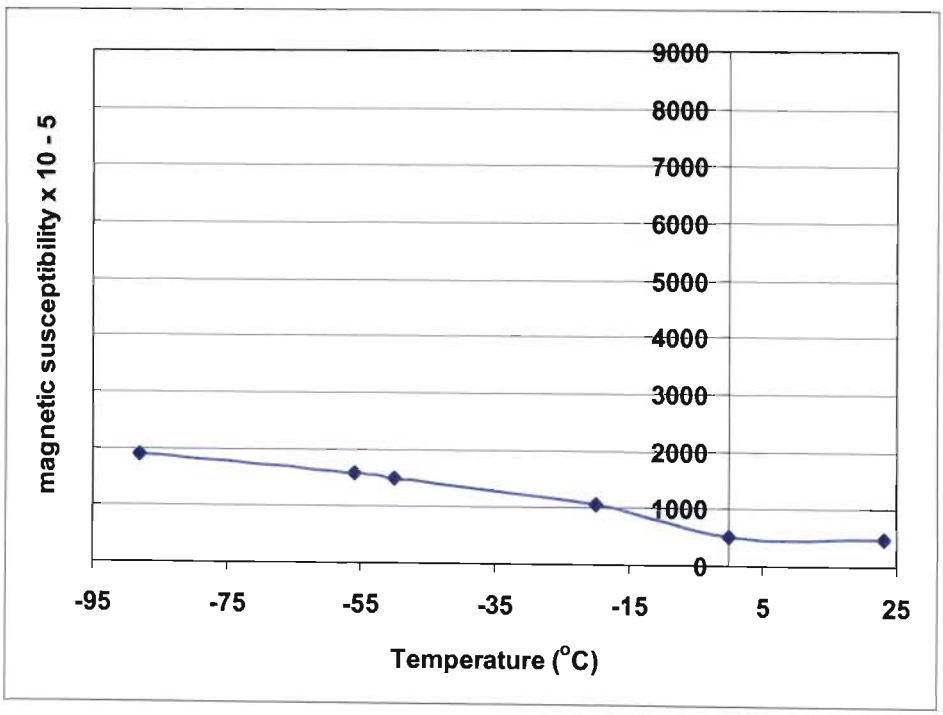

Figure 4.21: Correlation between magnetic susceptibility to sub zero temperatures of specimen A, 2nd generation of Alloy 2 [61]

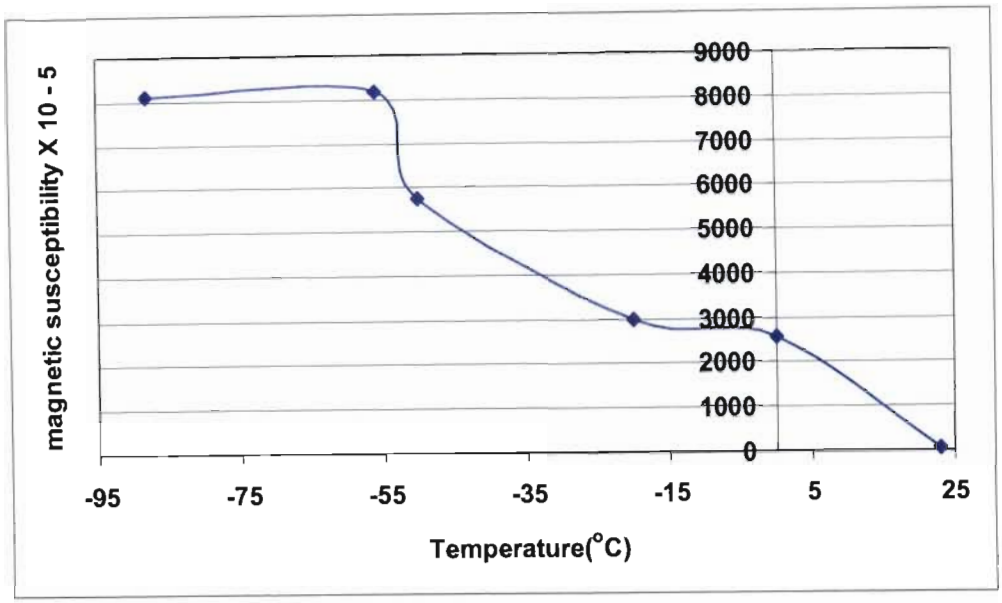

Figure 4.22: The effect of sub-zero temperatures on the magnetic susceptibility response of specimen B, 2nd generation of alloy 2 [61]

4.2.2.1 Conclusion

The mechanical tensile and compression testing results of 2nd generation of alloy 2 revealed that the 2nd generation alloy 2 qualified it to be used as a material for the manufacture of a wing aircraft bolt due to its high strength and exceptional degree of straining hardening (displayed in Table 4.6, Figures 4.14, 4.15 and 4.17 respectively), as well as having inherent corrosion resistance as per SPS –B-640 military standards for externally threaded fastener materials. Also discovered from these results was that 2nd generation alloy 2 displayed an exceptional ability to transform from paramagnetic austenite phase to a ferromagnetic martensitic product phase below the elastic yield point of the alloy. This phenomenon is illustrated in Table 4.6, Figures 4.14, 4.15 and 4.17. In addition, this property gave the alloy an inherent damage assessment ability that could be utilised for detecting and monitoring any form of damage (such as crack initiation) that could be incurred during operational service by monitoring the magnetic signature of the smart bolt.

Experimental results obtained from metallographic examination and the initial recorded reading of magnetic susceptibility (inductance) of the 2nd generation of alloy 2 tested specimens showed that the alloy had a duplex microstructure after thermo-mechanical processing. The impact test results showed that the fracture toughness and the magnetic susceptibility of 2nd generation of

alloy 2 increased significantly with decreasing temperature, illustrated in Tables 4.7 and 4.8. The incremental increase in fracture toughness and magnetic susceptibility with respect to decreasing temperature was attributed to the fact that the thermal martensitic phase transformation took place at a temperature close to the M_S temperature (-50°C). However, results gathered from further testing of the 2nd generation of alloy 2 to determine effects of sub-zero temperatures revealed that the ferromagnetic response of the alloy gradually increased with decreasing temperature for both tested specimens (Figures 4.21and 4.22). This meant that martensite was precipitated and increased as the temperature reached and exceeded the M_s temperature. This negative outcome meant that substantial data manipulation would have to be carried out in order to factor out these thermal effects if a meaningful and accurate damage assessment was to be achieved.

The 3rd generation of alloy 2 displayed the same ability as that displayed by the 2nd alloy 2 material with respect to the exceptional display of ferromagnetic response, i.e., from Figure 4.15, the transformation from austenite parent phase to a ferromagnetic martensitic product phase took place earlier (compared to the 2nd generation of alloy 2), well within the elastic region. Also from Table 4.6, the 3rd generation alloy had higher yield strength, ranging from 1050MPa to1100MPa, exceeding that of 2nd generation alloy (900MPa) and also registered almost zero magnetic susceptibility at initial testing conditions, although the 2nd generation alloy registered a higher ultimate strength compared to that of 3rd generation, illustrated in Table 4.6. The strength of 3rd generation fully met the strength criteria as stated by the military standards. Metallographical analysis of 3rd generation of alloy 2 test specimens revealed that the alloy also had a duplex microstructure after thermo-mechanical processing. However, from Table 5.3 both the actual chemical composition of the 2nd and 3rd generation of alloy 2 varied slightly from the intended target, which could be attributed to the manufacture of the alloys. It was also noted that both generations of alloy 2 contained the element molybdenum, which is an austenite stabilizer Nevertheless, the results clear showed that both generations of alloy 2 met strength criteria and an added magnetic response property required to be utilised as a damage sensor.

4.2.3 Experimental Test Results for Alloy 3

The chemistry for both the 2nd and 3rd generation melts of alloy 3 are shown below in Table 4.9 and the ferromagnetic response behaviour for both are represented by Figures 4.23 to 4.24. Table 4.10 gives an overview of the mechanical properties and the ferromagnetic response (magnetic susceptibility) of the TRIP alloys.

Table 4.9: **Differences in % chemical; composition between the desired target, 2nd generation and 3rd generation TRIP steels for alloys 3 [61]**

Element	C	Si	Mn	P	S	Cr	Mo	Ni
Desired target	0.25	0	10.0	0	0	12.0	0	1.50
Alloy 3, 2nd	0.19	0.08	10.5	0.005	0.010	11.6	0.03	1.33
Alloy 3, 3rd	0.20	0.068	10.2	0.011	0.014	9.66	0.13	1.86

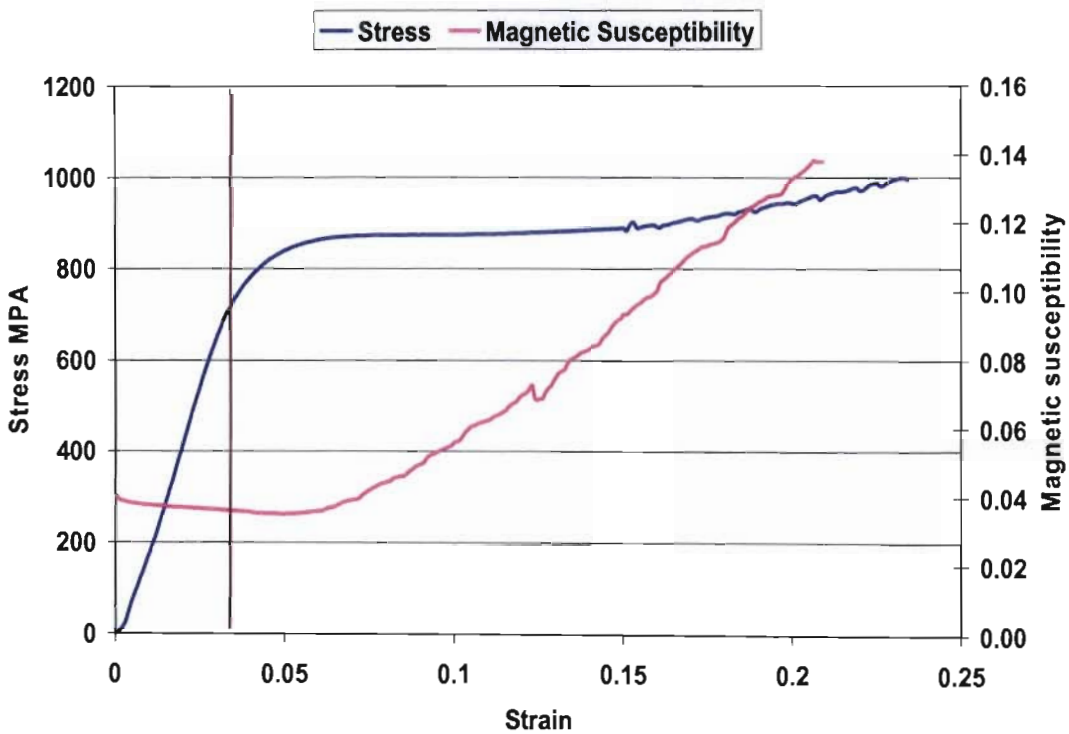

Figure 4.23: Typical tensile stress-strain and magnetic susceptibility-strain for the 2nd generation melt for alloy 3[61]

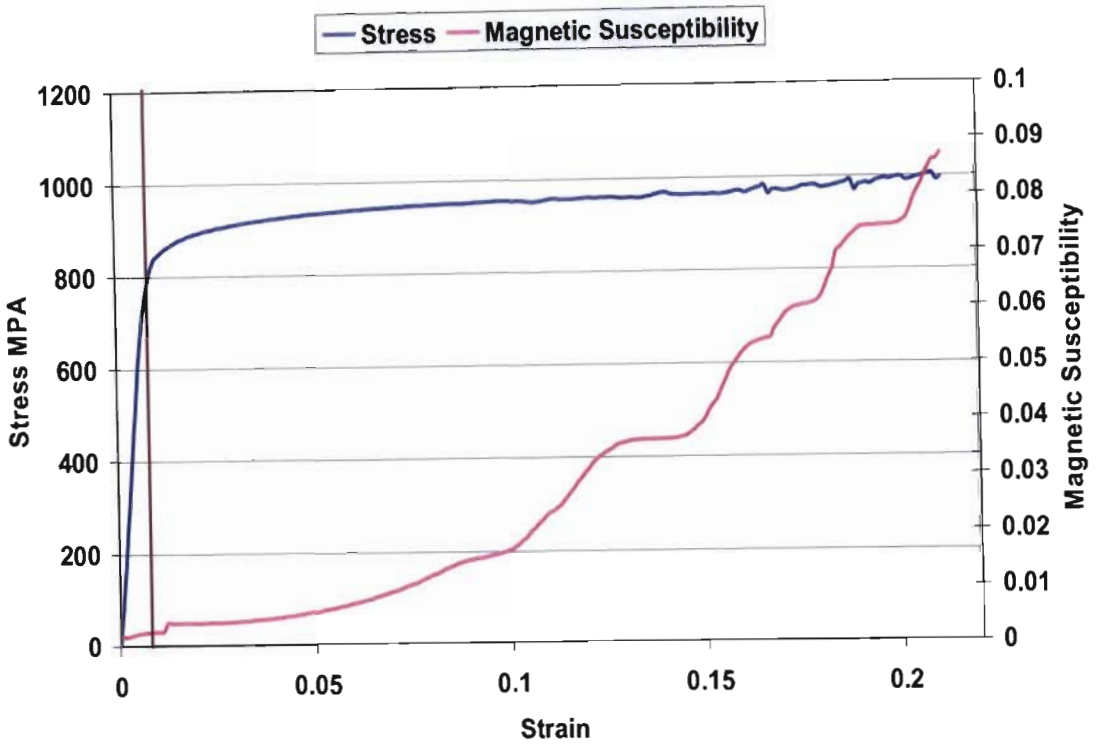

Figure 4.24: **Tensile stress-strain and magnetic susceptibility-strain curves for the 3rd generation melt of alloy 3 [61]**

Table 4.10: **Overview of the mechanical properties and the ferromagnetic response (magnetic susceptibility) of the TRIP alloys [61]**

Melt NO:	75% Reduction	Tensile Yield Strength MPa	Ultimate stress MPa	% Elongation	Initial magnetic Susceptibility	Final magnetic Susceptibility
2nd	75	800	1027	25	0.04	0.14
3rd	75	850	1000	15	0.00	0.09

Figure 4.25 picture A displayed no form of localised necking along the prismatic region of both specimens of the 2nd generation of alloy 3 and the fractured samples of the 3rd generation in picture D. However, in pictures B and C of Figure 4.25 the samples displayed shear type failure. In all cases the failure was brittle without any form of necking, which is attributed to the strain-induced martensitic precipitation during phase transformation.

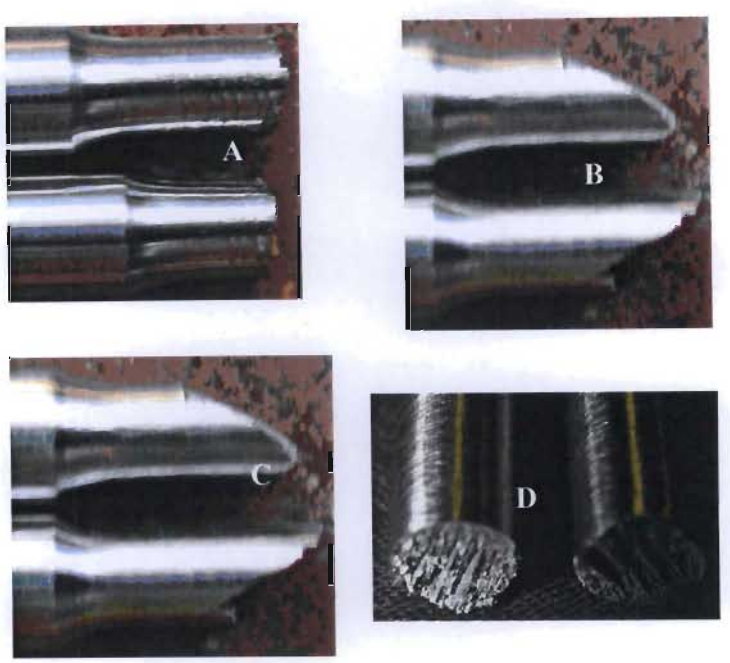

Figure 4.25: Shows the brittle fracture surfaces of the tensile tested specimens without any necking [61]

The Figure 4.26 represents two microscopic structures obtained from metallographic analysis of both generations of alloy 3 taken at 400X optical magnification. Both pictures A and B clearly indicate martensitic and austenitic elongations along the slip bands, which are oriented in the same direction as that of the rolling direction, indicating that transformation occurred. Picture, A, of Figure 4.26 displays a heavy incremental increase of the dark strips of strain-induced martensite with retained austenite (light coloured region). The SEM image of picture B shows elongated darkish strip regions representing the austenite regions, while the very light grey regions represent the martensitic region.

Figure 4.27 shows the microstructure for metallographicall analysed specimens for both generations of alloy 3 taken at 400X magnification, which clearly indicated dense dark strip of martensite which was attributed to the incremental increase in strain-induced martensitic precipitation along slip planes for tensile tested specimens, with retained austenite. The results are displayed as follows:

Figure 4.26: Microscopic structures for both the 2nd and of 3rd generations (SEM image) obtained from tensile tested specimens taken at 400X magnification [61]

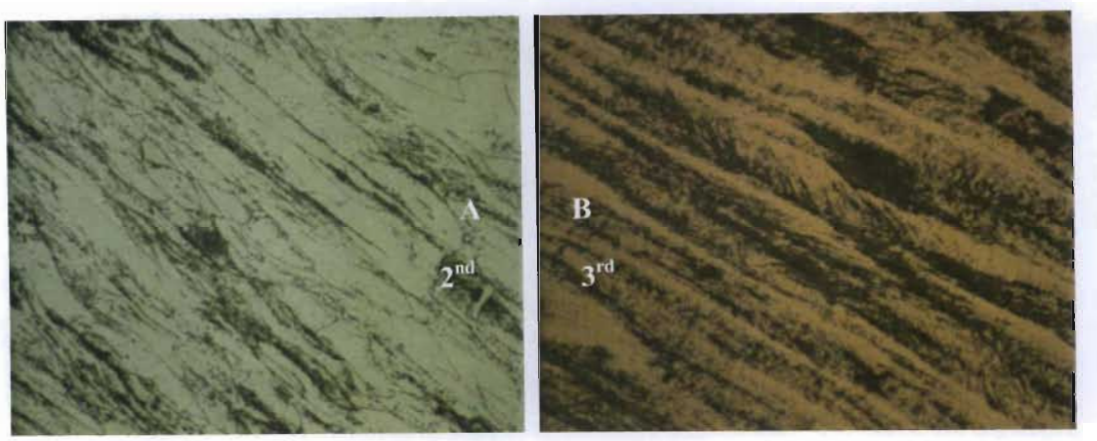

Figure 4.27: Microscopic structures for the 2nd and 3rd generation melts of alloy 3 taken at 400X for the compressed specimen, picture A, and tensile specimen picture B [61]

4.2.3.1 Conclusion

The mechanical tensile testing results of the 2nd generation of alloy 3 revealed that the alloy could not be utilised for the manufacture of the wing aircraft bolt because it did not qualify with respect to material strength. It did not possess the ultra high strength and exceptional high degree of straining hardening (displayed in Table 4.10, Figure 4.23) required as per military standards. It was also discovered from these results that the 2nd generation of alloy 3 displayed a poor degree of ferromagnetic response, i.e., the paramagnetic austenite phase transformation to a product ferromagnetic martensitic phase occurred quite far into the plastic region as illustrated

in Table 4.10 and Figure 4.23. In addition, due to the poor transformation displayed by alloy 3 this meant that it could not be utilised and depended upon to detect or monitor any form of damage

The 3rd generation of alloy 3 displayed different transformation characteristics to that of the 2nd generation alloy 3, i.e., from Figure 4.24, it was discovered that the transformation from austenite parent phase to a ferromagnetic martensitic product phase took place well below the yield point of the material, elastic region. Also from Table 4.10 it was noted that the 3rd generation alloy 3 had slightly higher yield strength (850MPa) which was 50MPA more than that of 2nd generation alloy (800MPa) and also registered almost zero magnetic susceptibility reading at initial testing conditions. Both the 2nd and 3rd generation of alloy 3 registered a similar ultimate strength, ranging from 1000Mpa to1027Mpa, Table 4.10. The strength of both 2nd and 3rd generations did not fully meet the military standards, strength criteria. Metallographic analysis of 3rd generation alloy 3 test specimens also revealed that the alloy had a duplex microstructure after thermo-mechanical processing. However, from Table 4.9 both the 2nd and 3rd generations of alloy 3 chemical compositions varied substantially from the intended target. This could be attributed to the thermal-mechanical manufacture of the alloys. In addition both the 2nd and 3rd generation alloys utilized a high percentage of manganese as their austenitic stabilizer element. It was noted that the 3rd generation of alloy 3 had higher molybdenum content. Nevertheless, the results clear showed that the both generations of alloy 3 do not meet the strength criteria required and they were therefore tested no further.

4.2.4 Experimental Test Results for Alloy 4

The chemistries for the 2nd and 3rd generation melts of alloy 4 are shown below in Table 4.11 and are both close to the target chemistry

Table 4. 11: Differences in % chemical composition between the desired target, 2nd generation and 3rd generation TRIP steels for alloys 4 [61]

Element	C	Si	Mn	P	S	Cr	Mo	Ni
Desired target	0.35	0.50	1.00	0	0	12.0	0	9.00
Alloy 4, 2nd	0.29	0.56	1.13	0.005	.007	11.6	0.01	9.48
Alloy 4, 3rd	0.35	0.58	1.64	0.11	.012	12.0	0	8.89

The ferromagnetic response behaviour for both the 2nd and 3rd generation alloys are represented by Figures 4.28 to 4.29. Table 4.10 below gives an overview of the mechanical properties and the ferromagnetic response (magnetic susceptibility) of the TRIP alloys.

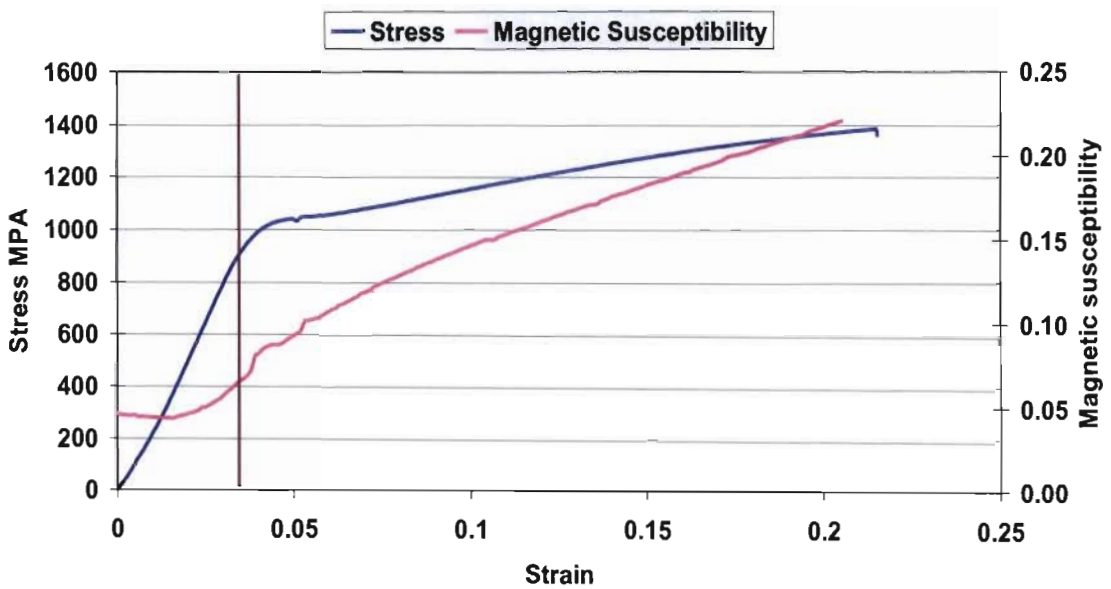

Figure 4.28: Tensile stress-strain and magnetic susceptibility-strain for the 2nd generation of alloy 4[61]

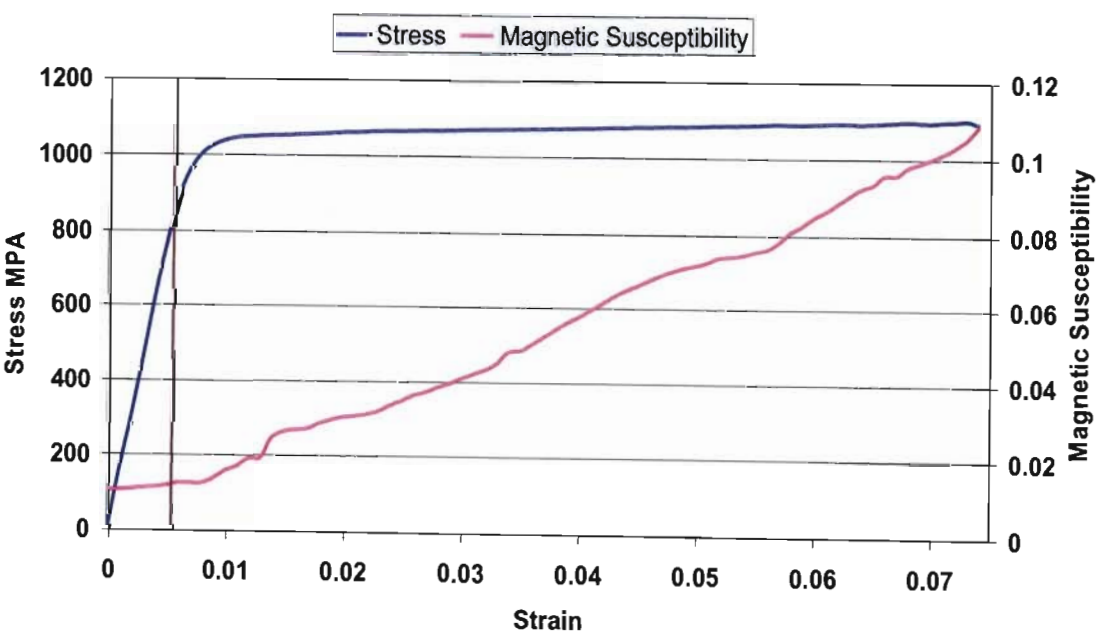

Figure 4.29: Typical tensile stress-strain and magnetic susceptibility-strain for the 3rd generation of alloy 4

Table 4.12: Overview of the mechanical properties and the ferromagnetic response (magnetic susceptibility) of the TRIP alloy 4 [61]

Sample NO:	75% Reduction	Tensile Yield Strength MPa	Ultimate stress MPa	% Elongation	Initial magnetic Susceptibility	Final magnetic Susceptibility
2nd	75	1011	1375	20.5	0.05	0.22
3rd	75	1030	1163	11	0.00462	0.07915

Tensile fractured specimens are displayed in Figure 4.30; the fractured surfaces shown in Figure 4.30 clearly showed no form of any localised necking along the prismatic region of the 2nd generation of alloy 4 in picture A. In addition, from pictures C and D of Figure 4.30, the fractured samples of the 3rd generation displayed no form of localised necking along the prismatic region. For both cases the failure to display any form of localised necking was mainly attributed to the strain-induced martensitic precipitation. It was also noted the same specimens (pictures A, C and D in Figure 4.30) displayed brittle failure with the exception of one specimen, which displayed typical brittle failure without any v-notched fracture, picture B.

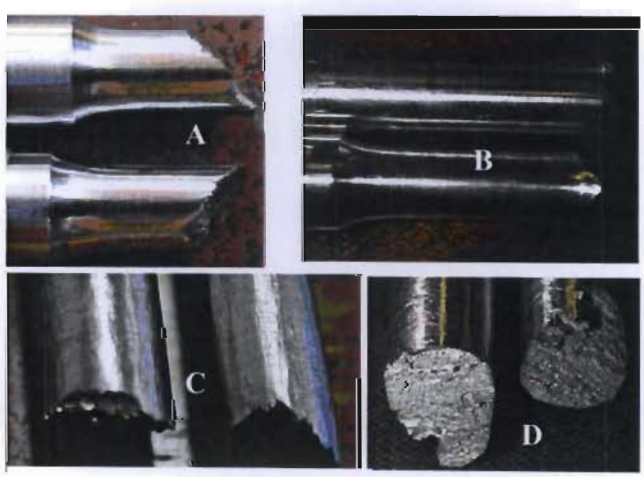

Figure 4.30: Brittle failure of specimens 1 and 2, 3 and 5 in pictures 1-4 response of the 2nd and 3rd generation of alloy4 respectively [61]

Figure 4.31 below illustrates the magnetic response with respect to applied stress loads, for the compression test conducted on the 2nd generation alloy material. The results obtained are similar to those of the tensile test conducted, from the viewpoint that the material phase transformation from parent paramagnetic austenite to a metastable product ferromagnetic martesitic phase was initiated almost from onset of testing, thus transformation taking place well before the yield.

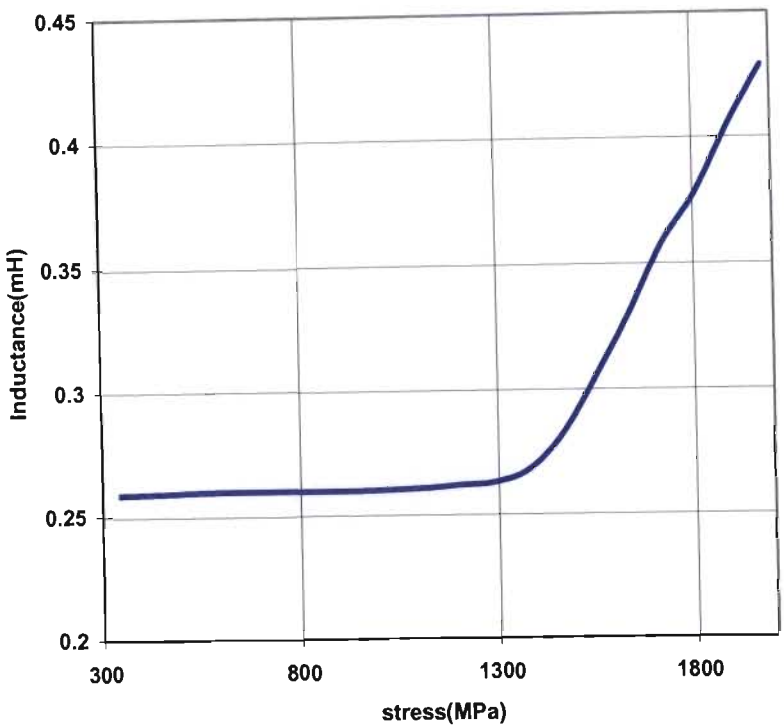

Figure 4. 31: Displays the inductance and compressive stress relationship developed for 2nd generation of alloy 4 [61]

Figure 4.32: Compression tested specimen, exhibiting slip band lines for the, 2nd generation alloy 4 [61]

The microscopic structures obtained from the metallurgical analysis for both the 2nd and 3rd generation alloys from tensile tested and compressive tested specimen are displayed in Figures 4.33 to 4.34. Picture A in Figure 4.33 taken at 400X magnification shows dark dense regions of strain-induced martensitic precipitation along the plane for the 2nd generation of alloy 4, with retained austenite (white coloured regions). The SEM image of the microstructure in picture B,

also showed dense amounts of strain-induced martensitic precipitation (dark regions) along the slip planes and dense white regions of retained austenite identical to that displayed in picture A. The microscopic structures shown in Figure 4.34 also displayed dense dark strain-induced martensitic precipitation along slip planes with retained austenite for the tensile tested specimens for both generations of alloy 4. The results are identified as follows

Figure 4.33: Microscopic structure of the 2nd generation, alloy 4 taken at 400 magnification of the compressed specimen in picture A, and tensile specimen in the SEM of picture B

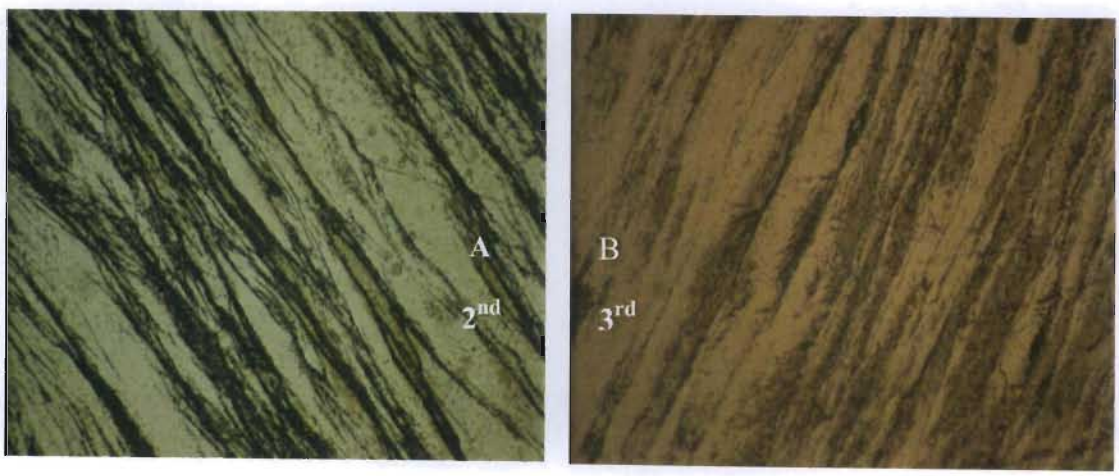

Figure 4.34: Microscopic structure of tested tensile specimens for both 2nd and 3rd generation alloy4, taken at 400X's optical magnification

The ferromagnetic response- strain and stress-strain properties of alloy 4 proved to be extremely good, shown in Tables 4.13 and Table 4.14 and Figures 4.28 to 4.29.

Table 4.13: Fracture toughness of the 2nd generation alloy 4 [61]

ID	Lateral Expansion		Shear %		Fracture Toughness J	
	20 °C	At -50 °C	20 °C	At -50°C	20 °C	At -50 °C
2nd Alloy 4	0.24	0.22	100	100	90	106
	0.21	0.12	100	100	98	144
	0.16	0.28	100	100	70	118

Figure 4.35 displays two pictures, picture A and B. In picture A the fracture that was displayed was pure shear at room temperature. At sub-zero temperatures (-50°C), picture B the fractured surface of the specimen displayed massive v- notch brittle fracture failure, similar to picture 1.

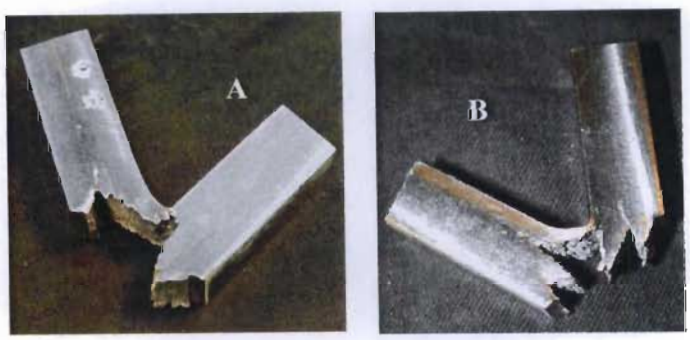

Figure 4.35: Shear brittle failure at room temperature, picture A, and at -50°C, Picture B the 2nd generation alloy 4 [61]

Table 4.14: Ferromagnetic response in terms of magnetic susceptibility at varying temperature of the 2nd generation alloy 4 [61]

Magnetic Susceptibility before Impact (20°C)	Magnetic Susceptibility before Impact (-50°C)	Magnetic Susceptibility after Fracture (20°C)	Magnetic Susceptibility after Fracture (-50°C)
0.000362	0.001446	0.003468	0.01215
0.000393	0.000432	0.007124	0.01489
0.000218	0.000541	0.005650	0.01113

Further testing was conducted on alloy 4 in order to investigate what kind of effects temperature alterations (particularly at sub-zero temperatures using dry ice) would have on the ferromagnetic response property on this TRIP steel alloy. Two samples were tested at sub-zero temperatures and at the same time the change in ferromagnetic response was measured using a magnetic susceptibility meter. The changes in susceptibility with respect to temperature are displayed in Figures 4.36 and 4.37.

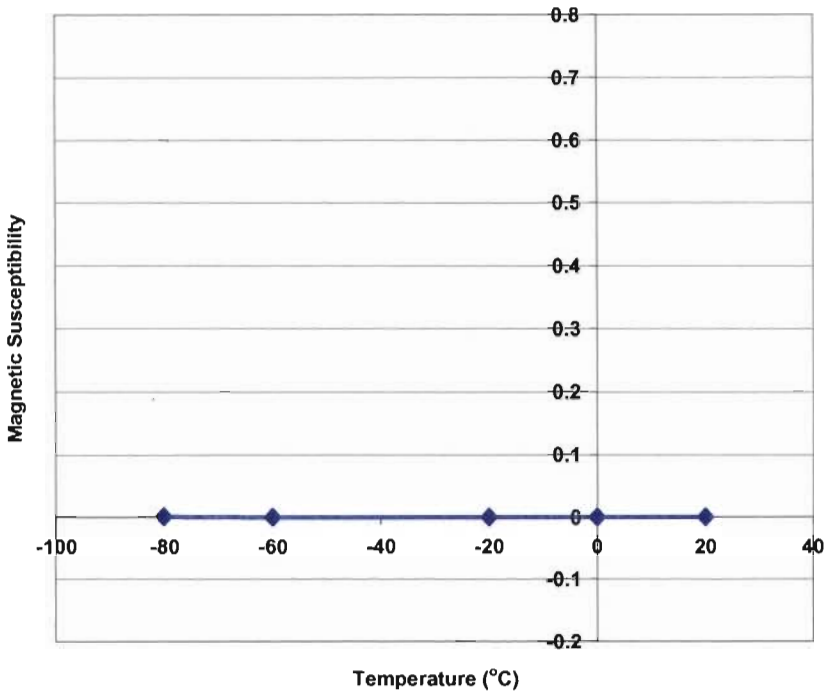

Figure 4.36: **Magnetic susceptibility with respect to varying sub-zero temperatures of the 2nd generation material 4 specimen A [61]**

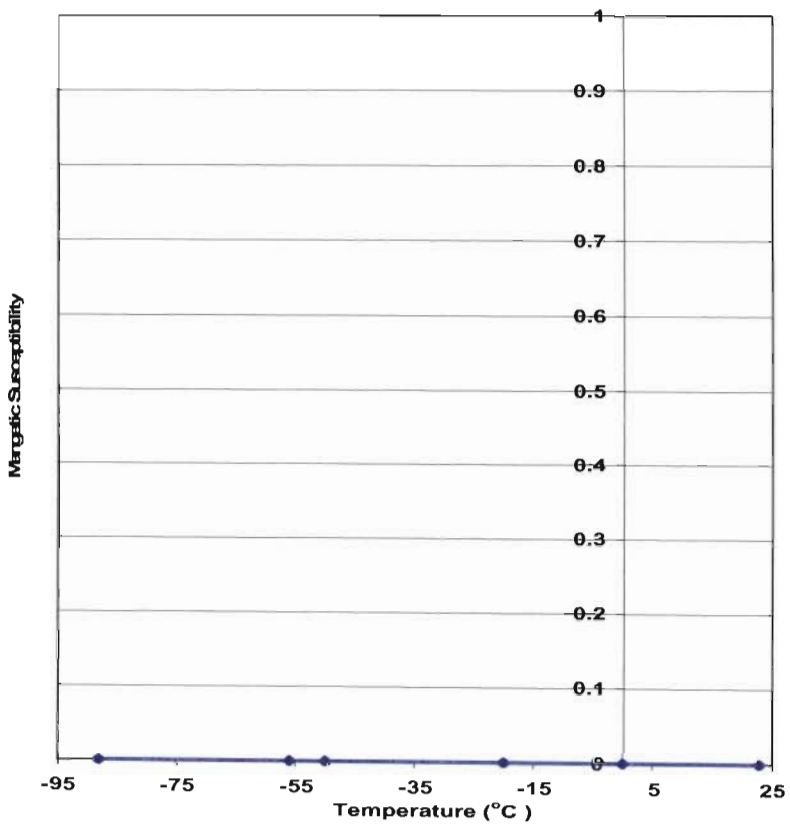

Figure 4.37: **Magnetic susceptibility with respect to varying sub-zero temperatures of the 2nd generation material 4 specimen B [61]**

4.2.4.1 Conclusion

The mechanical tensile and compression testing results obtained for the 2nd generation material of alloy 4 revealed an ultra high strength material with exceptional strain hardening (displayed in Table 4.11, Figures 4.28 and 4.29). This material also has enough Cr and Ni to possess good corrosion resistance and therefore meets the SPS –B-640 military specification. In addition the alloy displayed an ability to transform from paramagnetic austenite phase to a ferromagnetic martensitic product phase with a minimal incubation-strain period, which took place below the yield point of the alloy.

Experimental results from metallographic examination and the initial recorded reading of magnetic susceptibility (inductance) from 2nd generation alloy 4 test specimens revealed that alloy 4 had a duplex microstructure after thermo-mechanical processing. The impact test results of alloy 4 showed that the fracture toughness and the magnetic susceptibility of the 2nd generation alloy 4 increased significantly with decreasing temperature, which is illustrated in Table 4.13 and Table 4.14. The incremental increase in fracture toughness and magnetic susceptibility with respect to decreasing temperature was attributed to precipitation of a thermal martensitic phase. However, when further tests were conducted on the 2nd melt of alloy 4, the change in magnetic signature was zero, i.e., a constant reading was registered, as clearly demonstrated by Figures 4.36 and 4.37

The ferromagnetic responses of the 3rd generation of alloy 4 displayed virtually no form of strain-incubation, i.e., transformation from austenite parent phase to a ferromagnetic martensitic product phase began almost immediately upon application of the external load to the test specimens. The transformation also took place well within the elastic region. In addition, the 3rd generation of alloy 4 displayed a lower degree of strain hardening compared to that of 2nd generation of alloy 4, illustrated in Figures 4.28 to 4.29. The tensile test results also revealed that the 2nd and 3rd generation had similar yield strengths, illustrated in Table 4.12, with the 2nd generation of alloy 4 displaying higher ultimate strength and a higher ferromagnetic response range than the 3rd generation of alloy 4. However, the yield strength level (1000-1050 MPa) for both the 2nd and 3rd generation of alloy 4 satisfy the strength requirements for the material required to manufacture an aircraft bolt. Metallographic analysis of the 3rd generation of alloy 4 test specimens revealed that the alloy had a duplex microstructure after thermo-mechanical processing. However, Table 4.11 both the 2nd and 3rd generation of alloy 4 actual chemical compositions varied slightly from intended target; this could be attributed to the thermal-mechanical manufacture of the alloys. It was noted that the 2nd generation of alloy 4 contained a trace of molybdenum while the 3rd generation of alloy 4 contained a trace of phosphorus.

Nevertheless, the results clearly showed that the both generations of alloy 4 meet strength criteria and provided the added magnetic response required give the alloy the unique ability to be utilised as a damage sensor.

Although the material characteristics criteria were satisfied through extensive material testing of the four alloys, and a suitable candidate (meeting bolt the strength and transformation criteria) found, this was in a sense only the first milestone. The challenge was to use this material in a manner which would very substantially reduce the time spent jacking up the wings of C130 aircraft and removing all the bolts for inspection. To do this the bolt would ideally have to be interrogated in situ, with the use of a simple meters/hand-held device, and in addition questions regarding the effect of the mode of damage on the ability of the material to transform would have to be answered. During the testing of the four candidate alloys, simple strength testing was performed (in order to meet military standards), but the loading that the bolt will actually experience will most likely be of a fatigue nature. While it is well documented in any fatigue literature that before a cracks initiates in a component, a small plastic zone (which will produce transformation) is created ahead of the crack tip, the question arises whether this small amount of transformed material could be detected sufficiently early to produce a damage warning. Producing this warning relies not only on a steep transformation curve (engineered into the material through chemistry and processing) but a sufficiently sensitive interrogation instrument. Thus the second half of the Smart Aircraft Bolt project could be termed Product Development.

4.3 Product Development

4.3.1 Design Concepts for Smart Aircraft Bolt

Once the evaluation of the strength and transformation characteristics of the different TRIP steel alloy materials was concluded, several smart design concepts were evaluated, with the aim of determining which bolt design configuration satisfied the requirements of the product design specification (SPS-B-640 military standards). It was important to provide a bolt which met all the functionality of the current 4340 bolt, but could easily be interrogated to access the amount of damage incurred in the bolt. There is no sense in substituting a smart (and more costly) material into the bolt if it takes 200 man hours to determine whether there is any damage. A means of measuring the changing magnetic susceptibility therefore needed to be incorporated into the bolt assembly. Several design concepts were considered, including

1. A hole drilled down the centre of the bolt so that a probe could be easily inserted into the bolt, while the bolt was still in situ.

2. An undercut (as seen in Figure 4.38) beneath the head of the bolt. This deliberately introduces a stress raiser so that the first site of transformation is here and a washer with an internal coil placed over the undercut could be easily interrogated for its changed inductance. Inductance in a coil changes as the magnetic permeability of the bolt material changes.

3. Another bolt design with an undercut before the top thread (as seen in Figure 4.39) having a smart washer/nut (as described above and pictured in Figure 4.43) over the first thread, which is a natural site of the first damage. Again this would only require an inductance meter to be connected up during interrogation and could be performed with the bolts in situ.

Figure 4.38: Smart Aircraft bolt with groove cut out underneath the bolt head.

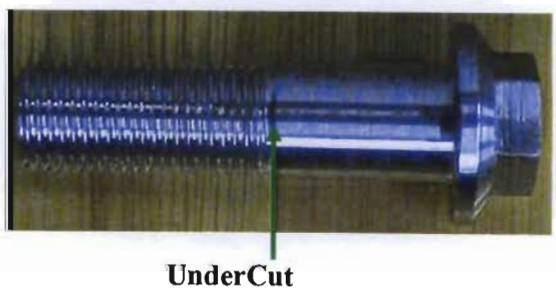

Figure 4.39: Smart Aircraft bolt with an undercut just before the beginning of the top thread

Design concept 1 was discarded on the basis that military specification (and indeed mindset) would not permit such a configuration. Design concepts 2 and 3 were both tested with the smart washers over the sites of interest.

The monitoring of the incubation strain corresponding to the strain induced martensitic nucleation (incremental change in the magnetic susceptibility of the material) was achieved

with the use of two SMART washers. One washer was mounted at the bolt head (area over the groove or undercut for grooved bolt) while the other was placed at the beginning of the first thread root and across the first four threads, as these are the sites at which the bolt experienced the highest stress due to stress concentration (areas which promote crack initiation), thus the small plastic zone existing ahead of the initiated crack is the areas in which the material has undergone phase transformed from austenite to martensite. Hence such an area will register some magnetic signature. The yield strength of washer material in which the electrical coil is embedded equalled that of the aircraft bolt so that overstressing of the assembly produced preferential deformation within the TRIP steel bolt. The plastic deformation was obtained by measuring the inductances of the coils embedded in the SMART washer. This inductance was measured quite simply by two hand-held Inductance meters connected to the coil leads. Figure 4.30 shows the assembly drawing smart bolt, washer, coil, nut test grips used for tensile testing.

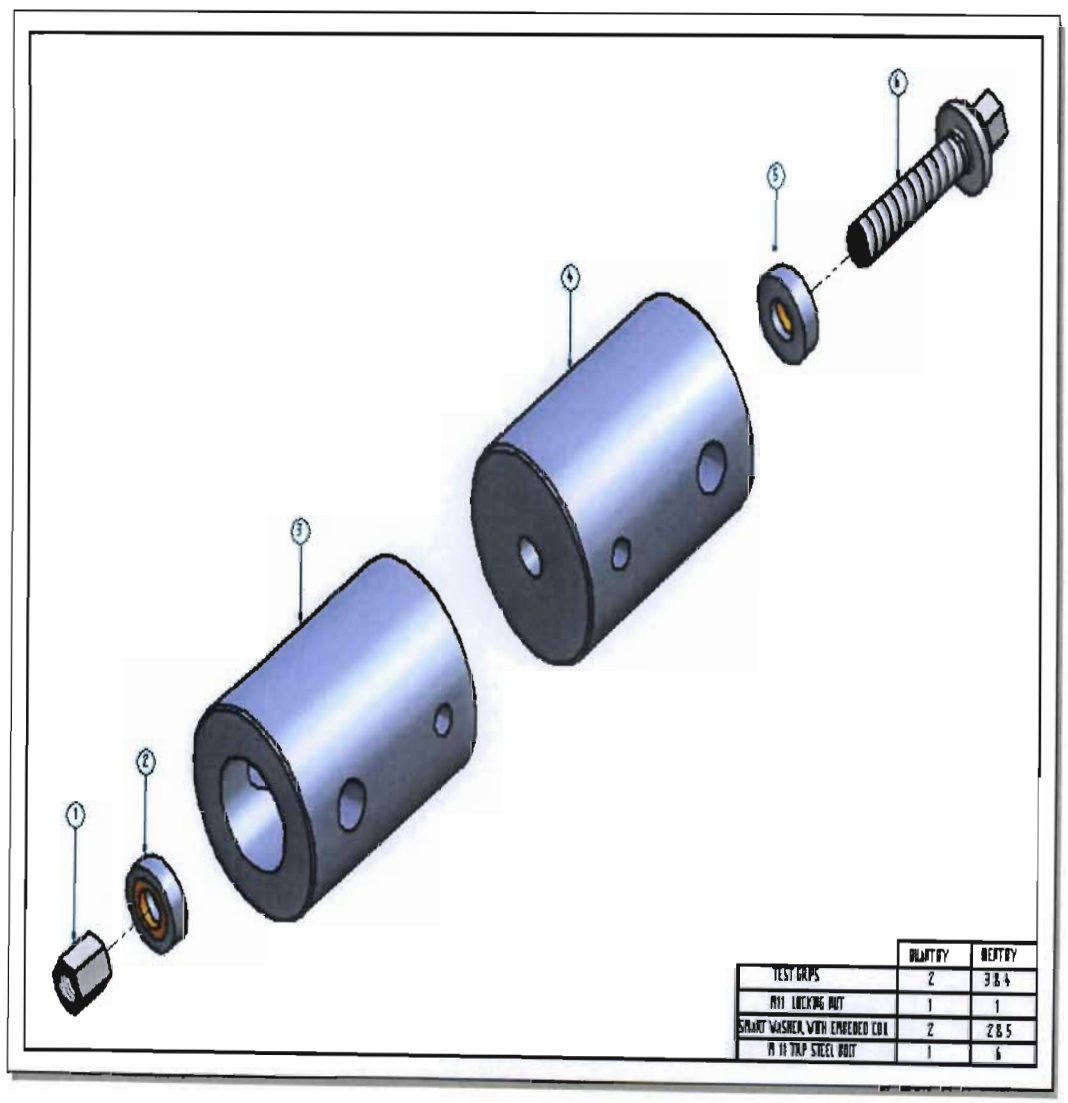

Figure 4.40: Assembly schematic layout of the tensile of the smart aircraft bolts.

The concept of having the coils over the first thread proved most effective (and most natural) for detecting damage, but substantial testing was required to verify that this concept worked in practice. Among the issues to be dealt with were:

1. The fact that the loading conditions experienced by the bolt in situ will not be pure tension, but in fact fatigue loading, and, the question arises as to whether the coils within the smart washer would be sensitive enough to detect any change in ferromagnetic response of the bolt material caused by any form of damage, created before a crack initiates.

2. Would the constant cycling of temperature have any effect on the sensitivity of the coils or washer itself? Would the material of the smart washer interfere in any way with the readings of magnetic transformation in the bolt, by showing a temperature induced transformation itself?

In order to answer these questions a series of fatigue and cryogenic tests were devised using sub-scaled prototype studs (with known transformation curves) as seen in Figures 4.41 and 4.42. The experimental methods for this testing are described in details in the section below

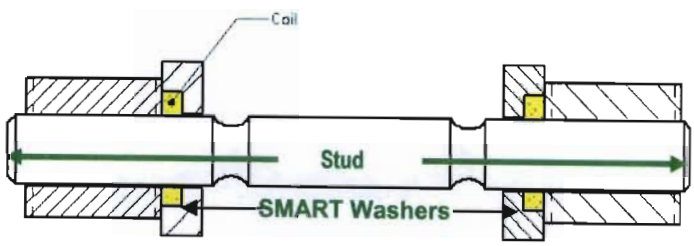

Figure 4.41: Sub assembly schematic layout of the smart stud with the smart washers used for both cyclic temperature and cyclic fatigue testing

Figure 4.42: M11x1.5 cut thread stud, Smart washers and locking nut placed on either side over the top of thread(s) used for both the temperature cyclic testing and fatigue tension-tension testing

4.3.2 Fatigue Testing

A series of sub-scale SMART aircraft prototype studs were manufactured from the two different strain memory alloys with known transformation characteristics, and tested in fatigue mode (oscillating loads through a set point) using an MTS fatigue testing machine Third generation TRIP steel melt were tested using the MTS fatigue testing machine. The inductance of the SMART washer was monitored before and during cycling until failure of the studs occurred. The data obtained from the experiments was used to establish the endurance limit and how sensitive the SMART washers were, i.e. how soon do the SMART washers detect the damage. Ideally the microstructural transformation should occur ahead of the crack tip, because this is a region where the material has plastically deformed. Therefore the smart washer should pick up the magnetic signature before the crack is initiated.

A SMART washer consisted of a base metal manufactured out of 316 stainless steel, copper coil embedded into the base metal and held together by epoxy resin (LR 220 plus Ampreg 20 harder) which was allowed to cure for six hours. The coil consisted of 0.112mm copper wire wound to 350 turns. The coil/washer set up is illustrated below in Figure 4.43:

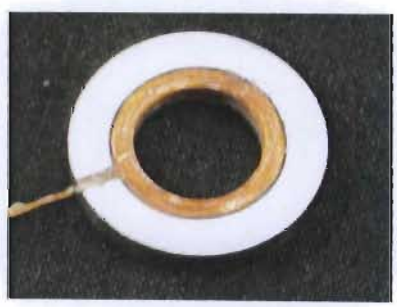

Figure 4. 43: Smart washer with a copper coil embedded into a stainless steel base metal

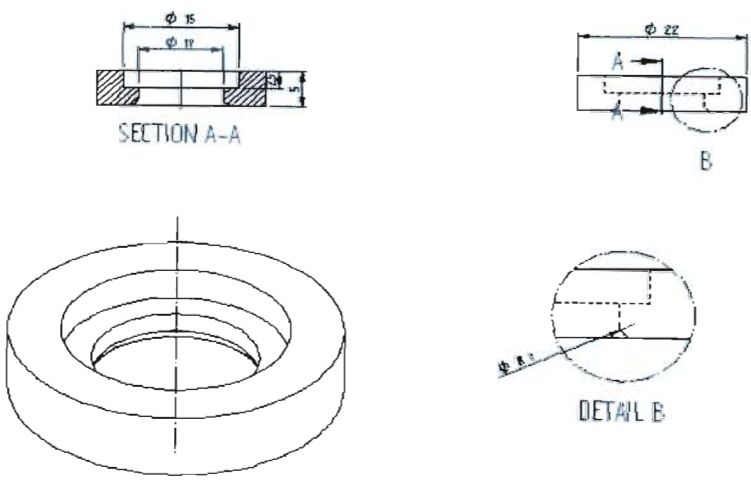

Figure 4.44: Schematic line drawing of smart washer

4.3.2.1 MTS Control and Hydraulic Setup

The MTS fatigue test machine operated a double-acting, double-ended heavy-duty actuator piston rod under precision closed loop servovalve control (precision force generation), which was appropriate for the cyclic tension fatigue testing of the prototype bolts. The piston rod movement was accomplished by the supply of high pressure hydraulic fluid to one side of the actuator piston (port A), which caused the piston rod to extend and then opening the other side to the return line (port B), making the piston rod retract. The amount of hydraulic fluid and the speed and direction of the movement was controlled via the servovalve. The force applied to the prototype bolt, which was mounted between the actuator piston rod and the load frame cross-head, was the result of the applied differential pressure and effective piston area.

The hydraulic actuator operated at a pressure rating of 21 MPa. This was supplied from two motors rated at 11KW, 20 litres per second at 21 MPa and 40 KW, 80 litres per second at 21 MPa respectively, dependant on loading parameters. The MTS frame structure is rated for 100KN.

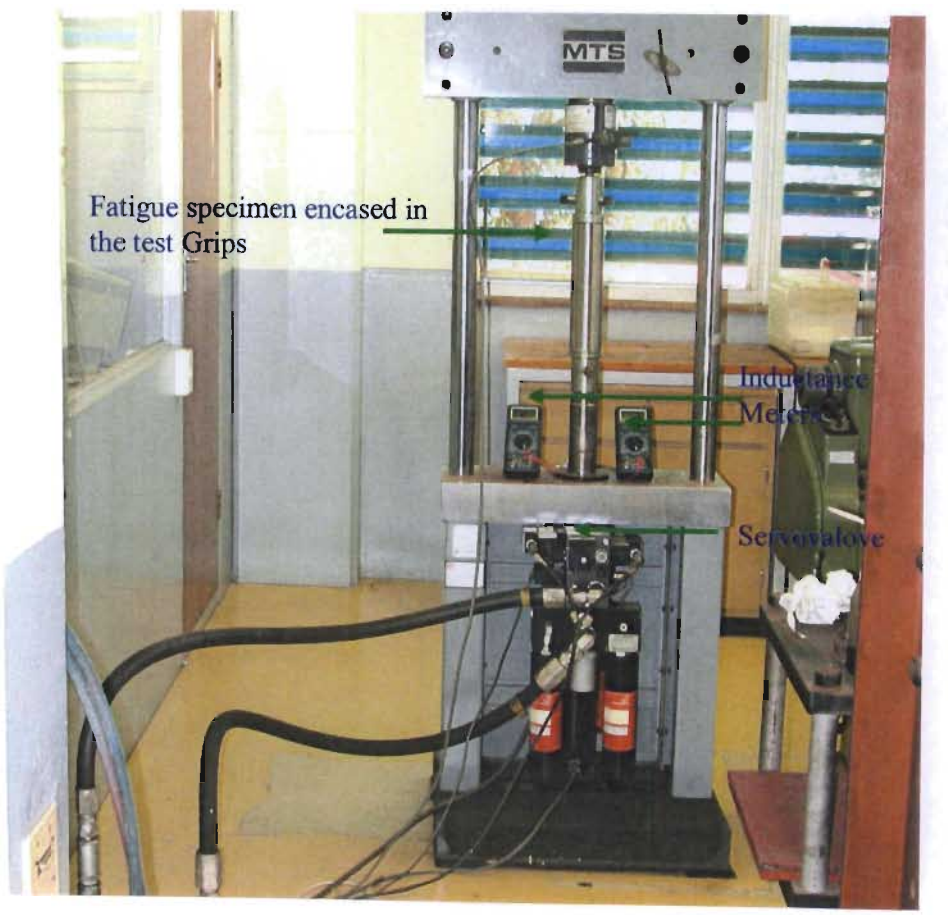

Figure 4.45: MTS machine used for fatigue testing

The MicroConsole model 454.XX controller provided a work station for multifunctional digital display for signal read out, cycle counter, program and record control, hydraulic pressure control, hydraulic interlocks (which typically lock the system at low fluid levels or if the hydraulics over-heat), program interlocks and mechanical interlocks for load frame crosshead lock circuit and load frame test area guard or actuator rod position limit switches respectively. The MicroConsole also housed an internal power supply for plug in modules, primarily designed for vibration, structural and component testing.

Figure 4.46: MicroConsole model 458.10 controller.

The MicroConsole was integrated with a 458.72 DC controller, Model 458.90 functional generator and a WaveBook for data capture. The DC controller rendered the set point control to balance the valve command signal for control mode transfer for the servovalve, span setting (the precise adjustment of the dynamic amplitude of the force range of the composite command), interlocks such as upper and lower limits, which were adjusted to set the most positive level of the force of the upper limit and lower limit detectors. If the feedback signal exceeded the levels of the upper and lower limit, the test was aborted and indicator lights were displayed on the MicroConsole Display. The function generator was a plug-in module used to provide an output waveform that was selected for cyclic sine-wave form fracture mechanics and fatigue testing. The whole integration of the MicroConsole controller, wave book, input command signal and feedback signal together with the test parameter spacing are explained in the Functional Decomposition schematic layout of the entire experiment as illustrated in Figure 4.47.

Functional Decomposition of the Experiment

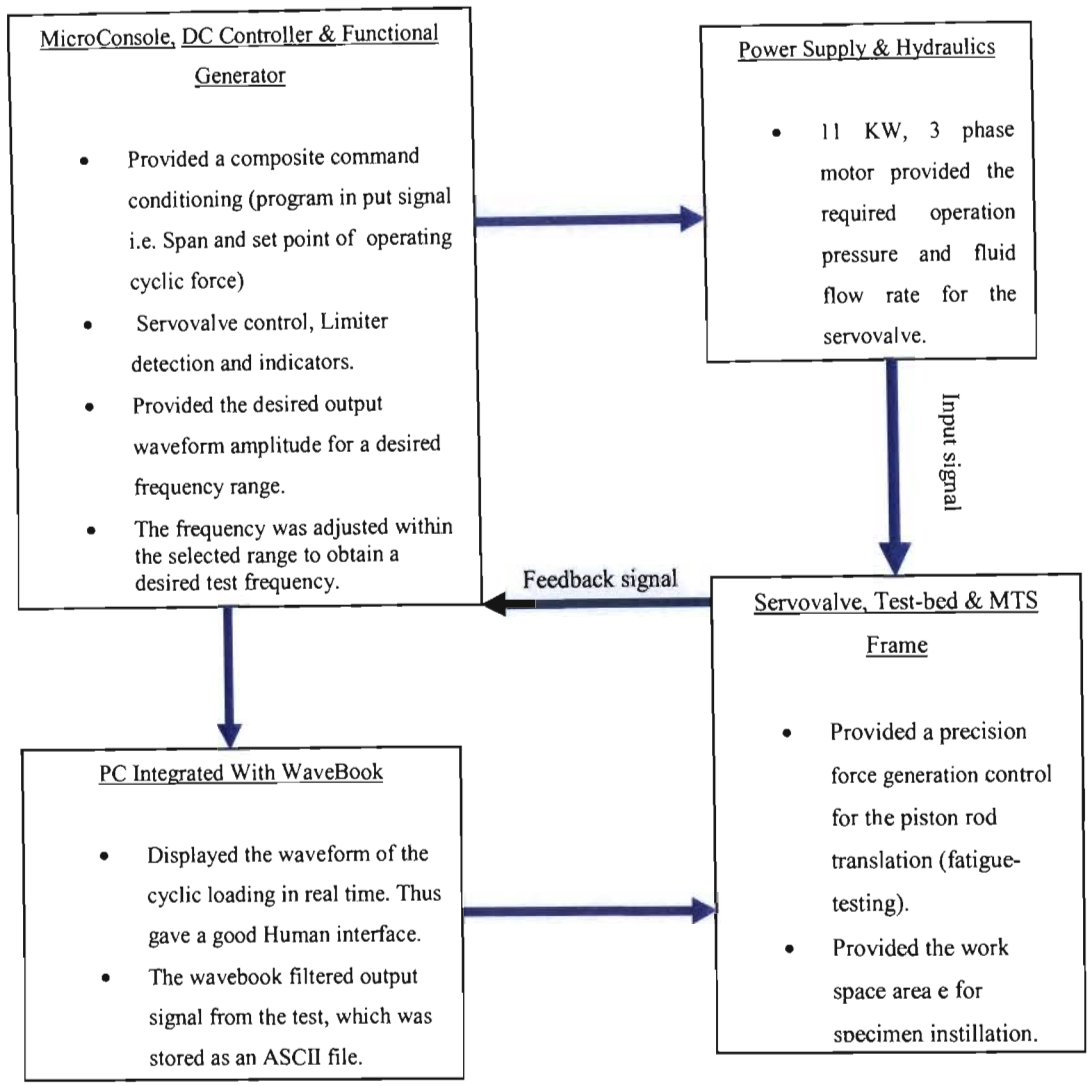

Figure 4.47: Schematic layout of the function decomposition of MTS fatigue testing machine

4.3.2.2 Specimen Installation

The SMART stud was placed between two test grips, after which two SMART washers were placed on either side over the cut-out of the stud. The cut-out acted as a stress concentration. The SMART stud was mounted against test grips and the face of the locking nut that engaged the first thread of the stud. The locking nuts were then torque, which made the bottom the faces of the test grips butt firmly up against the washers inside the grips and bottom faces of test grips respectively. This also removed any form of free translation of the specimen during testing.

The washers were situated at these positions because the first three threads of the studs carried about seventy percent of the load. These were areas that illustrated pronounced sudden changes of state (transformation) from metastable paramagnetic parent phase austenitic to ferromagnetic product phase martensite within the SMART aircraft stud. Two M60x 2 threaded shafts with a step down shoulder with a cut-out hole (pin slots) connected the test gips to the interlinks.

An interlink was inserted over the shoulder, which consisted of a hole cut out of M60x 2 threaded shaft, held together by a 25.4mm pin and its opposite ends consisted of M27x 2 threads that was screwed into the servovalve piston and load cell respectively. Two locking rings were mounted on either side of the test grips and interlinks so that they were held in position throughout the duration of cyclic loading. The set up assembly configuration is shown in Figure 4.48

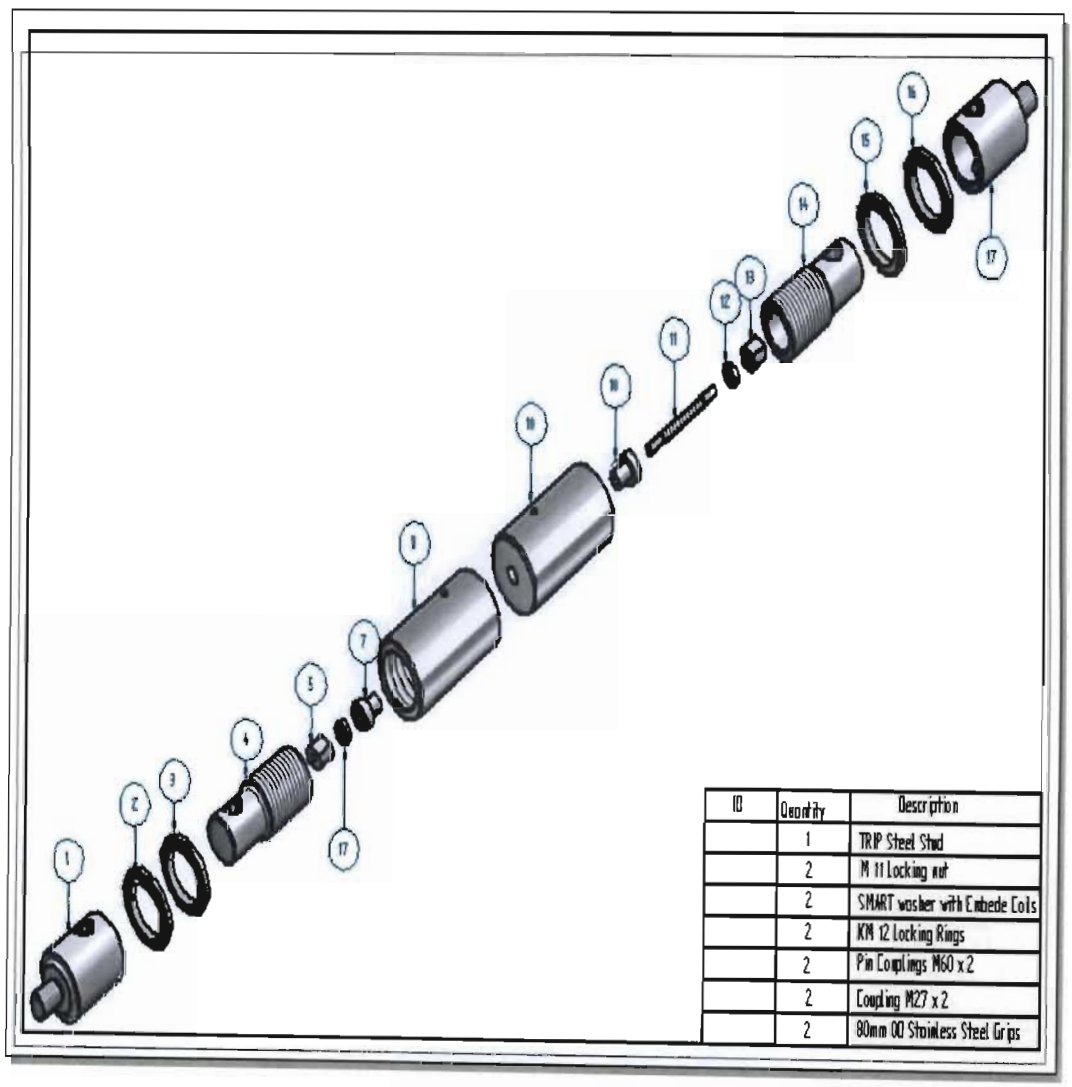

Figure 4.48: Assembly of the smart stud, smart washers, locking nuts and test grips, used for cyclic temperature and fatigue testing on MTS test machine

The data acquisition and tabulation of sinusoidal waveforms in real time (input load oscillation on the specimen about a set point) where monitored using a graphical Windows based program in WaveBook on a computer integrated to the MicroConsole Controller). The program was set up so that data was continuously scanned for a specified duration of time and at a specific rate, using frequency (cycle count, every 1000 cycles need to recheck this) until failure. Simultaneously the irreversible transformation from paramagnetic austenite to ferromagnetic martensite that occurred at successive high fatigue loading was also monitored and recorded by two inductance meters at the exact time the data acquisition was triggered in the waveform program.

4.3.3 CyclicTemperature Testing

A Cryogenic chamber was used to carry out cyclic temperature testing on the SMART aircraft studs. The cryogenic chamber operated a 3kW cooling unit, which comprised of a two stage compressor, two stainless steel cylinders with a 2 kW cooling element wound in between the inner and outer cylinders. The loading of the specimen then occurs within the inner of the two stainless steel cylinders. The outer cylinder was heavily insulated from the exterior in order to prevent any form of energy dissipation or gain. The chamber was rated for a temperature range from 60°C to -50°C, which was set up, controlled and monitored by a temperature-time controller.

The studs coupled with smart washers were tested in a cryogenic atmosphere under static load in tension. Specimen installation was exactly the same as described for the fatigue testing because all the grips used were the same. The Smart washers (embedded coils) where tested for the effectiveness in terms of sensitivity; at what point the strain-induced transformation in the material could be detected.

Figure 4.49: Cryogenic chamber, cooling unit, temperature controller, and load read out meter

4.3.4 Metallurgy and Microscopy

The metallographic and microscopy analysis was carried out using exactly the same method for specimen preparations, mounting and hardness testing to select the best polishing method and polishing technique, as that used for the tensile specimens and untested, straightened flat plate off-cuts for the most promising two candidate materials.

4.4 Test Results from Product Development

Product development includes several phases:

1. Possible design scenarios were evaluated.

2. The most promising design concepts were tested in simple tension-tension, fatigue mode as well as cryogenically (cyclic temperature under constant load).

3. Material response and geometry were modelled using a combination of material results, and computer packages. These results are presented in chapter (6) as they form a slightly different discussion.

In section 4.2.1 three concepts for the smart bolt system were discussed, namely a centre drilled bolt (immediately rejected based not only on the military specification but also on initial modelling results (of previous work [77]). The other two concepts both involved a smart washer which effectively measures the changing inductance of a coil embedded within the washer. The inductance change as a result of the magnetic susceptibility of the core (in this case the bolt) can therefore be correlated to damage within the bolt. The two possible sites for the smart washer application were sited for the two different smart bolt design concepts: one site would have been either a groove added beneath the head of the bolt (to concentrate damage) and a washer placed over the site, or a washer could be place over the site of the first damage, which (from bolt theory literature [106]) is the first thread. Subscale studs were therefore manufactured and tested in tension-tension fatigue as well as cryogenically, to determine whether the smart washer was sensitive enough to detect damage and if so which position provided the best results.

Ideally alloy 4 would have been used to conduct this testing; however, the difficulties of reproducing chemistries (in small quantities) with stringent alloying windows (Schaeffer- De Long, Figure 4.9) in South Africa proved an obstacle. Nonetheless, in reality all that was required to answer the question of product development was an alloy or alloys with similar known transformation characteristics.

For the purposes of simple tensile testing the two different positions of the smart washer on a bolt, an alloy (MB1) with lower tensile strength (and well-documented transformation curve) was used. This material was also used (due to greater available quantities) to produce material data for the modelling phase of the product development. The chemistry of MB1 (as seen in Table 4.15 below) had similar Cr and Si levels to that of alloy 4, but relies primarily on Mn to stabilize the austenite phase down to room temperature. The lower carbon content makes it considerably less strong than alloy 4, but substantial quantities (having been cast and processed in semi-commercial quantities) made it very useful for all the testing required for transformation data for mechanical response modelling

Table 4.15: Differences in chemical composition between the 2nd, 3rd generation alloy 4 and, MB1 TRIP steels

Element	C	Si	Mn	P	S	Cr	Mo	Ni
Desired target Alloy	0.350	0.500	1.000	0.000	0.000	12.000	0.000	9.000
Alloy 4, 2nd	0.290	0.560	1.130	0.005	0.007	11.600	0.010	9.480
Alloy 4, 3rd	0.350	0.580	1.640	0.110	0.120	12.000	0.000	8.890
MB1	0.180	0.460	9.300	0.016	0.015	14.170	0.000	1.540

4.4.1 Tensile Evaluation of the Smart Prototype Concepts 2 and 3

As previously stated the material used for the simple tensile test of the two bolts of concept 2 and 3 was MB1, which has been tested extensively using standard tension and compression specimen's geometry. Figures 4.50, 4.51 and 4.52 below show the tensile and compressive test results for the alloy using standard geometry). Tables 4.16 and 4.17 show the tensile and compressive properties respectively.

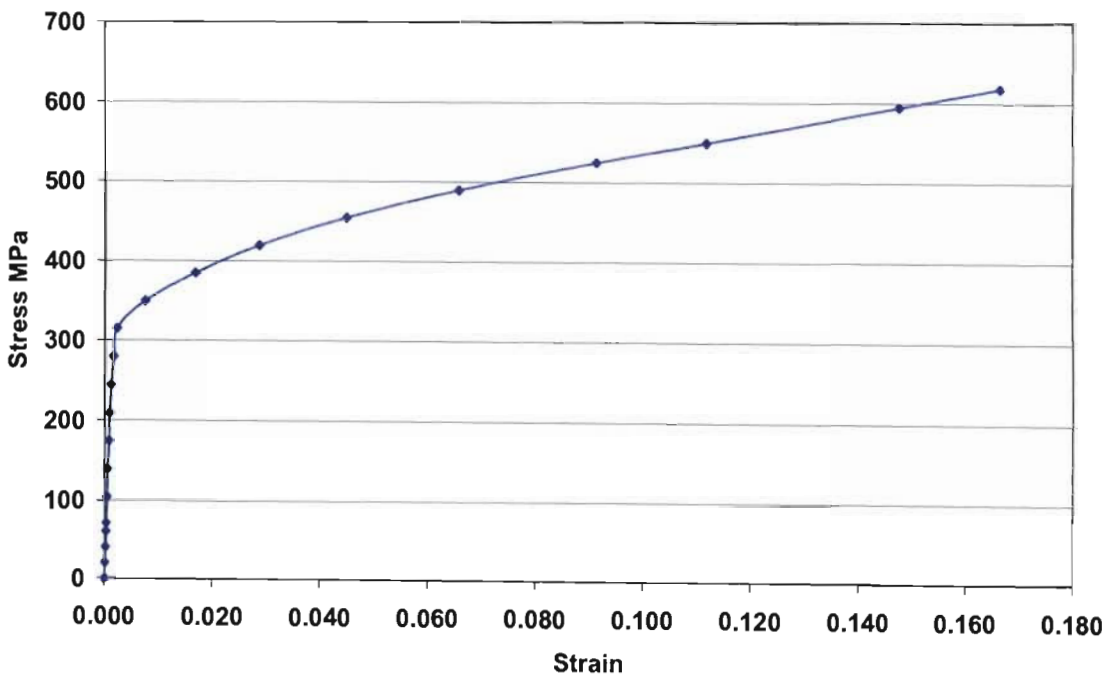

Figure 4.50: Tensile Stress-strain curve for the MB1 TRIP Steel alloy

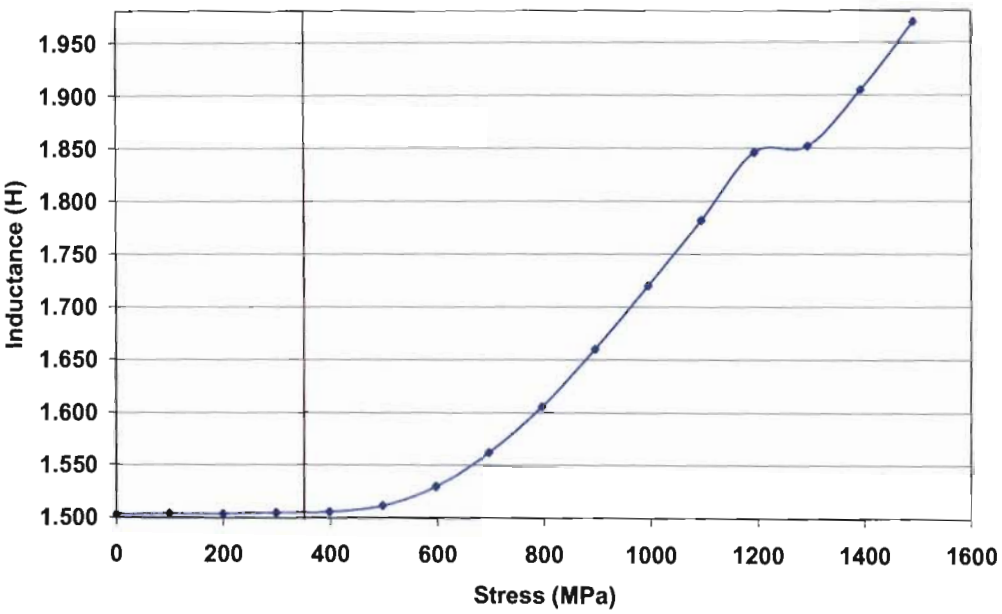

Figure 4.51: Inductance-compression stress curve for the MB1 TRIP Steel alloy

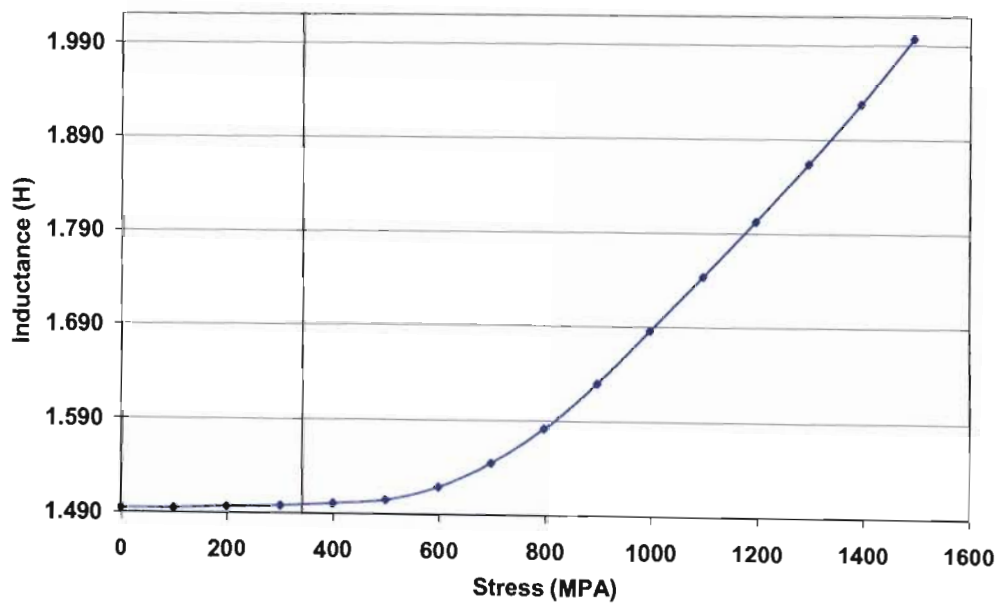

Figure 4.52: Inductance-compression stress curve developed for MB1 TRIP Steel alloy

Table 4. 16: Mechanical tensile properties of the MB1 TRIP steel alloy

Sample NO:	% Reduction	Tensile Yield Strength MPa	Ultimate stress MPa	% Elongation
1	80	300	618.0873	16.6352

Table 4.17: Overview of the compressive mechanical properties and the ferromagnetic response (change in inductance) MB1

Sample NO:	75% Reduction	Compressive Yield Strength MPa	Ultimate stress MPa	Initial Inductance H	Final Inductance H
1	75	350	1492.78	1.503	1.969
1	75	350	1584.63	1.495	1.997

A set of sub-scaled Smart aircraft bolts manufactured from a 22 mm diameter MB1 TRIP steel rod material were tensile tested. As previously explained the bolts had two different design concepts, one with a groove under the head and another with a groove just before the beginning of the first thread (section 4.3.1, Figures 4.38 and 4.39).

Two smart washers were used, one placed underneath the bolt head (pink curve in Figure 4.54 and 4.55) and the other washer placed over the top thread(s), (represented by the blue curve in Figures 4.54 and 4.55). The second washer was placed over the first three threads due to the fact that the stress distribution is never uniform throughout the threads [106]. Furthermore, thread 1 carries the greatest portion of the load due to the fact that the mating potion of the nut never experiences compression, thus the resulting deflection slightly increases the bolt pitch and decreases the nut pitch, which tends to relieve the pressure on threads 2 and 3, as seen in Figure 4.53 below

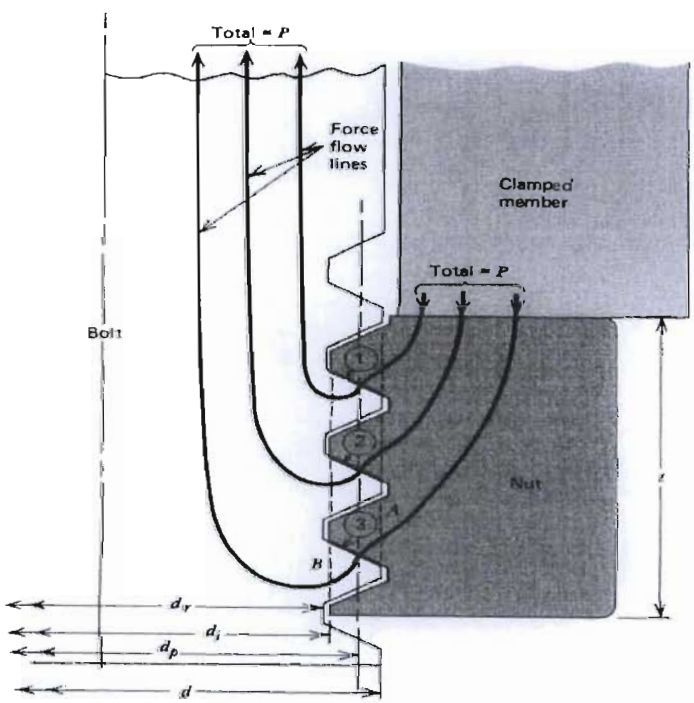

Figure 4.53: Demonstrating of the force flow through a bolt in tension [106]

4.4.1.1 Design Calculation of Smart Bolt Using MB1 TRIP steel alloy

The design calculation for the bolts/nut sizes is shown below. The smart bolts were M11 x 1.5 ISO standard bolts, into which the threads were cut. This made it both cost effective and less time consuming to manufacture. The force required to fracture the bolt at first thread is given by

$$F = \sigma_y \times A_s \tag{4.1}$$

where A_s (72.30mm^2) is the tensile area for the threaded section, for ISO metric cut threads, and σ_y is the yield of material [Table 4.15]. Therefore

$$F = 300x10^6 \times 72.30x10^{-6} = 21.690kN$$

In order to determine a balance between the bolt tensile strength and the thread stripping of both the bolt and the nut, the bolt tensile force required to yield the entire thread-stripping failure surface of the nut based on parabolic stress distribution is expressed as follows:

$$F = \pi d(0.75t)\sigma_y \approx \pi d(0.75t)(0.58\sigma_y) \tag{4.2}$$

Thus equating equation 4.1 and 4.2 indicating a balance between bolt tensile and thread-stripping length, the nut thickness was approximated to be

$$t = 0.47d \tag{4.3}$$

However, nuts are usually softer than bolts in order to allow slight yielding of the top thread(s) and thus distribute the load more uniformly among the threads in contact, and stand nut thickness is approximately

$$t = 7/8d = \frac{7}{8}11 = 11mm$$

locking nut of 20mm was used to clamp the bolt.

The results of tensile test bolt are illustrated in Figures 4.54 and 4.55. Figure 4.56 displays the position where fracture of the bolt occurred.

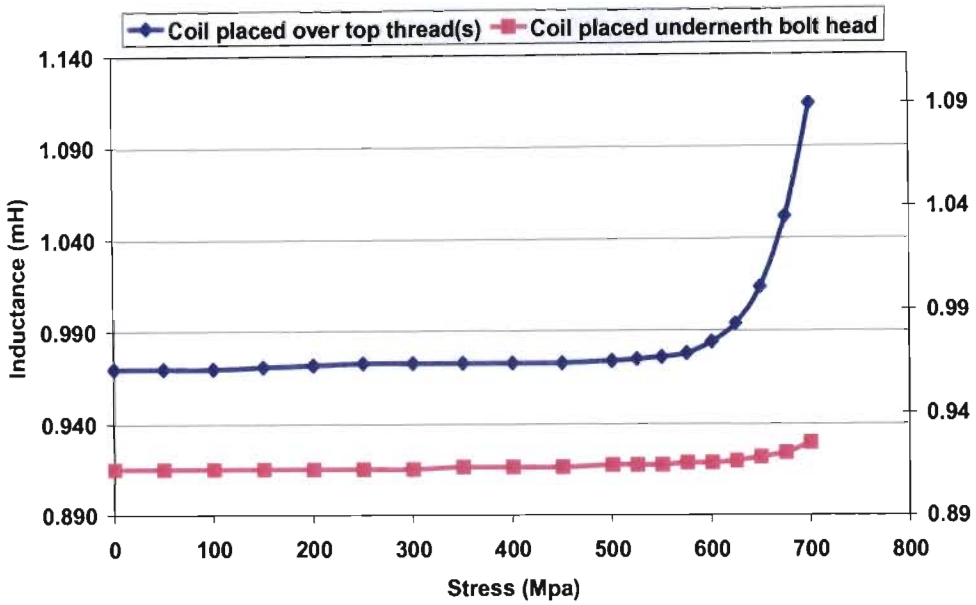

Figure 4.54: **Difference in Inductance-tensile stress curves for smart washers placed over the top thread(s) and under the bolt head for specimen 1**

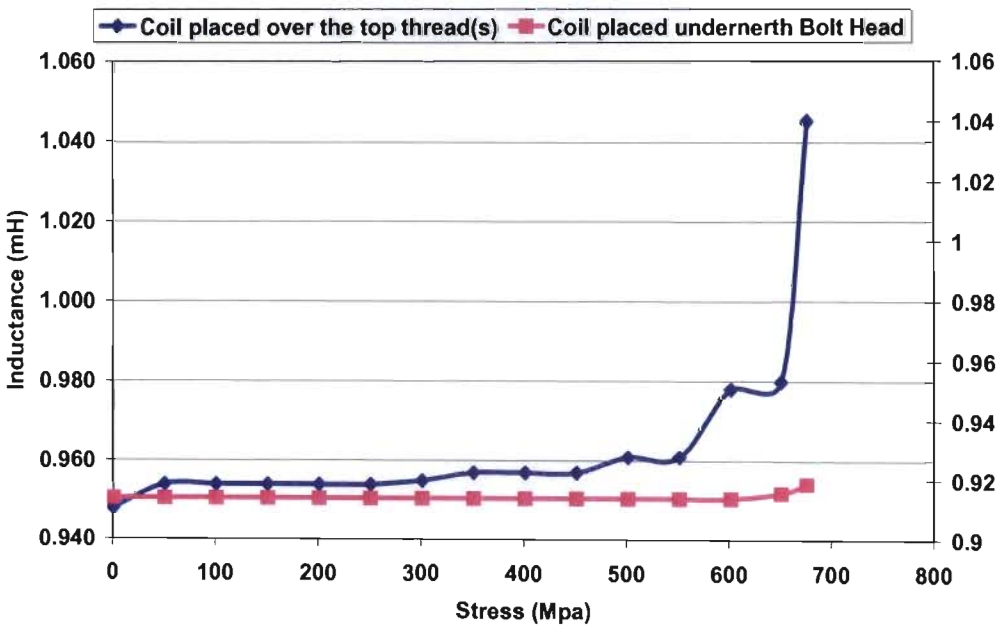

Figure 4.55: **Difference in Inductance-tensile stress curves for smart washers placed over the first few threads and under the bolt head specimen 2**

Figure 4.56: Bolt fracture for both bolts occurred at the first thread root [61]

Metallographic samples were cut off from MB1compressed specimens, (from areas where the specimen buckled the most, i.e., the central part of the compressed specimen) and their microstructure was analysed. The metallographic results for both MB1 are represented as follows: Pictures A and B, in Figure 4.57 taken at 400X magnification show dark dense grey/black regions of strain-induced martensitic precipitation along the plane for both specimens 1 and 2, with retained austenite (yellow coloured regions). The microscopic structures shown in Figure 4.58 and Figure 5.59 taken from the tensile tested smart bolts are identical for both samples. The microscopic structures for untested metallographic analysed samples, picture A, showed minimum fraction of martensite, while picture B, tested bolt samples, showed dense dark regions of box martenstic precipitated along the slip planes with retained yellow regions of austenite for both samples photo micro photographed at 400X optical magnification.

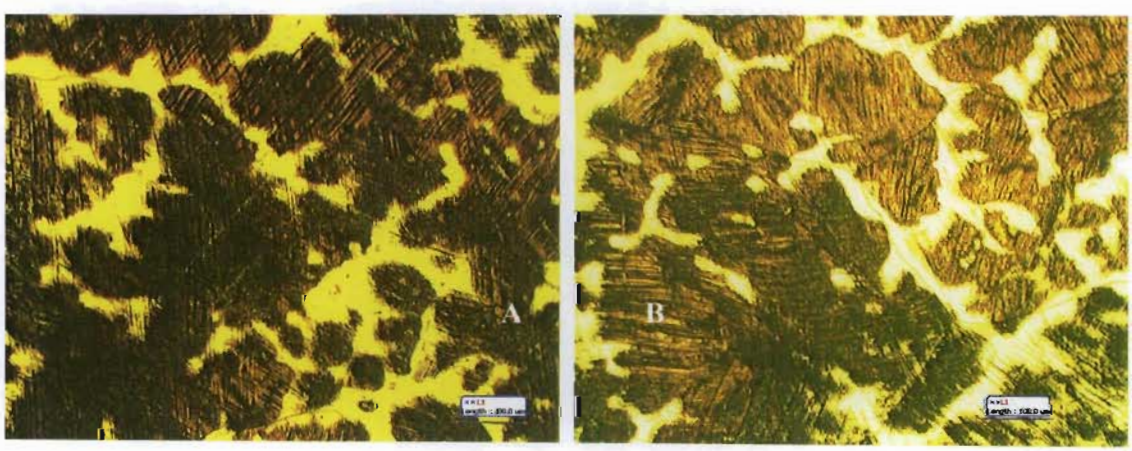

Figure 4.57: Shows dark martensite regions and retained austenite, yellow regions of the micro structures for the compressed specimens 1 and 2 manufactured from the MB1 TRIP steel alloy in pictures A and B

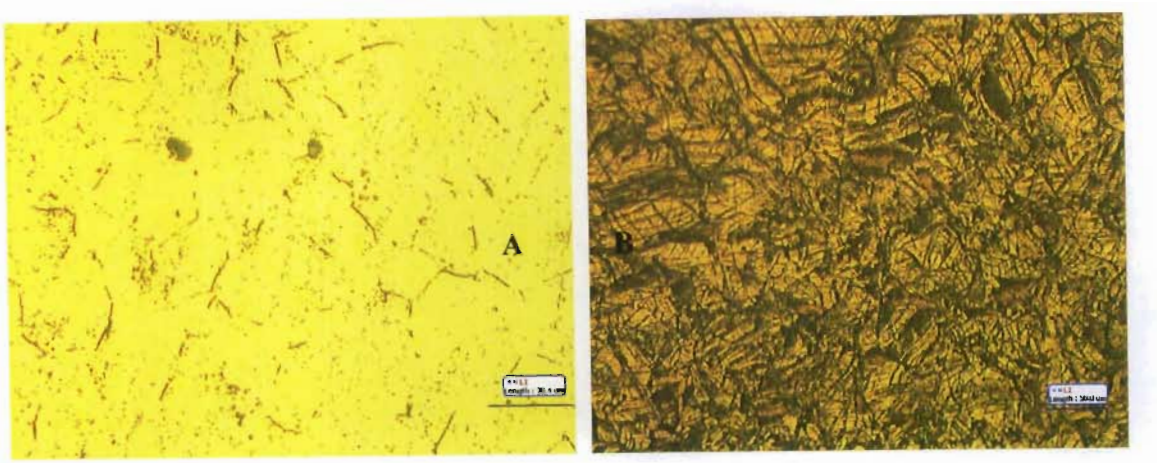

Figure 4.58: **Microscopic structures for untested MB1 sample, picture A, and tensile tested smart bolt sample 1, picture B, micro photographed at 400 time magnifications**

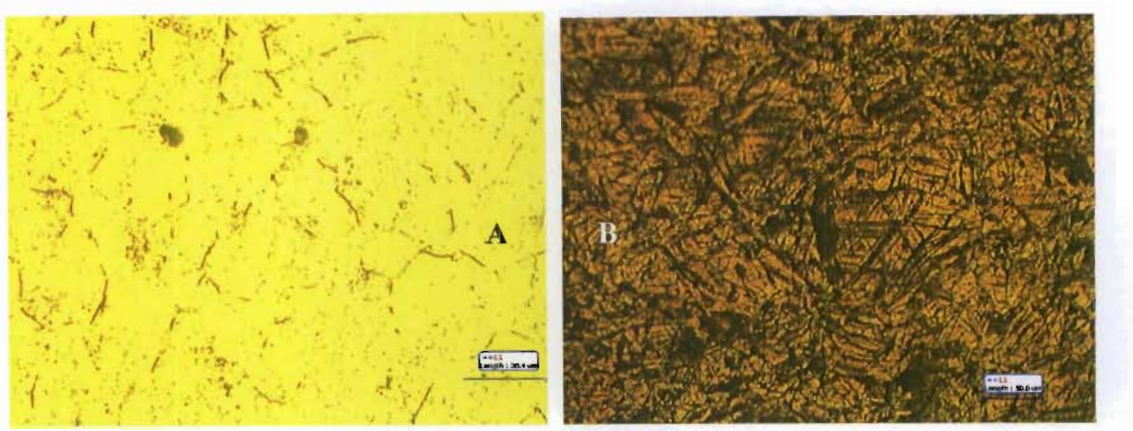

Figure 4.59: **Microscopic structures for untested MB1 sample, picture A, and tensile tested smart bolt, picture B sample 2, micro photographed at 400 time magnifications**

M2BR alloy was used for fatigue and cryogenic testing of phase 2 of the product development a

Table 4.18: **Differences in chemical composition between the 2nd, 3rd generation alloy 2 and, M2BR TRIP steels, appendix E**

Element	C	Si	Mn	P	S	Cr	Mo	Ni
Desired target Alloy 2	0.300	0.500	2.100	0.000	0.000	8.500	2.000	8.400
Alloy 2, 2nd	0.210	0.360	2.570	0.005	0.006	8.000	1.910	8.910
Alloy 2, 3rd	0.330	0.440	2.630	0.013	0.016	8.750	1.700	8.490
M2BR	0.320	0.610	4.200	0.005	0.005	8.420	0.010	8.400

Note that alloy 2 did not have a good transformation response as alloy 4, and also the chemistry of M2BR contains slightly more percentage manganese than either generation of alloy 2, making the austenite phase more stable (and hence less easy to transform) than alloy 2. In addition, one would expect that there would be some thermally precipitated martensite present at low temperatures (similar to alloy 2), making it perfect to thoroughly test the smart washer's sensitivity. The results of these will follow in section 4.4.2 and 4.4.3.

As previously mentioned, the fatigue testing of the prototype concepts was conducted using a material designated as M2BR TRIP steel. Prior to commencing manufacture of the studs to be used for fatigue testing, a compression test was performed to give an indication of the transformation of the material, the results and microscopy of which are shown in Figures 4.60 and 4.61. Figure 4.61 displays the microscopic structure for both the untested and compressed M2BR TRIP Steel alloy. As seen in picture A, there is virtually no form of martensite as opposed to picture B, which displays dark martensite regions, precipitated along the slip-planes, and with retained austenite, yellow regions.

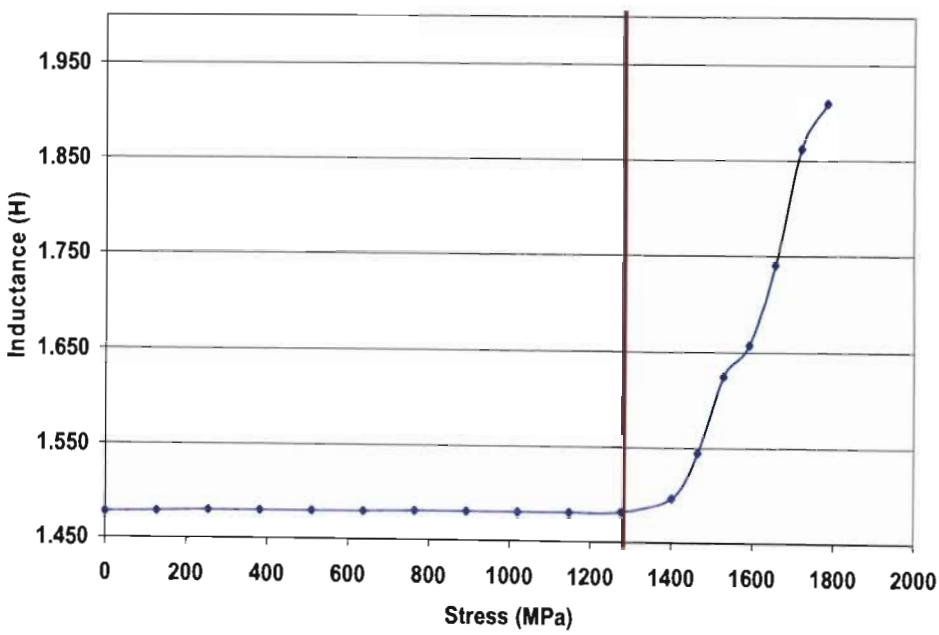

Figure 4.60: Inductance-compression stress curve for M2BR TRIP Steel alloy

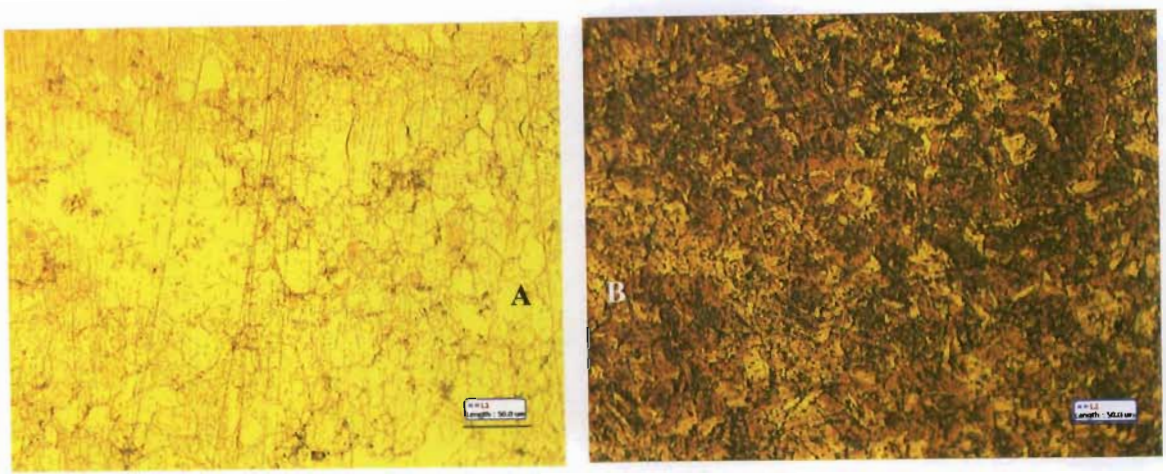

Figure 4.61: **Microscopic structure of the untested and compressed M2BR TRIP Steel alloy. Pictures A and B, photo micro photographed at 400 time magnifications**

4.4.2 Fatigue Testing of the Two Prototype Concepts

The Figures 4.41 and 4.42 in chapter 4 display the smart stud (machined out of M2BR TRIP Steel) and smart washer (316 stainless steel) sub-assembly, fully coupled with the testing grips assembly as shown in section 4.3.2.1 Figure 4.45. Two M2BR TRIP steel specimens were tested using the MTS fatigue test rig, at a frequency of 4 Hertz. The locking nuts on either side of the stud were tightened to a force of 5kN and the set point was set to 44kN, which is an initial mean load from which the amplitude was offset. The set point was adjusted on the DC 458.72 controller set point dial representing a ±100% full-scale read out of the load cell, and the span (amplitude) setting was adjusted to 12kN using the span scaled dial, also represented by ±100% full scale, i.e., the specimens were cycled between 38kN and 50kN to failure. The DC controller on the Microconsole provided the command input for servovalve control and output signal to wave book for data acquisition of load with respect to time for the number of cycles to failure. The change in inductance representing the change in permeability of the material was recorded for every 2500 cycles using a set of smart washers. The fatigue tests were conducted at room temperature.

4.4.2.1 Calculation of Low Cycle Fatigue and Bolt Tension with External Joint Separation Force

The bolt axial load F_b and the clamping force between test grips F_c are both equal to the initial tightening force F_i. For a complete clamped member (rigid joint) as show in Figure 4.62 picture (a) and free body diagrams pictures (b) and (c) of Figure 4.62

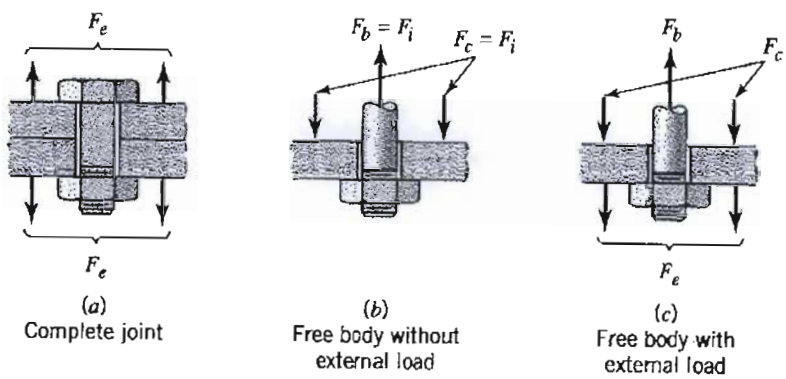

Figure 4.62: Free body diagrams for a bolt subjected to clamped loading conditions [106]

The Bolt axial force and the clamping force are expressed by the following equations [106]

$$F_b = F_i + \left(\frac{1}{1+R}\right).F_e \quad \text{and} \quad F_c = F_i + \left(\frac{1}{1+R}\right).F_e \tag{4.4}$$

$$R = \frac{K_c}{K_b} \tag{4.5}$$

where R is the ration of spring stiffness of the smart bolt, K_b, and Clamping members, K_c (test grips), F_e is the external separating force applied. The spring rates are defined by the following equation:

$$K_c = \frac{A_c E_c}{g} \text{ and } K_b = \frac{A_b E_b}{g} \tag{4.5}$$

where $E_c = E_b$ = 200 GPa and g is the approximated effective length bolt illustrated in Figure 4.63

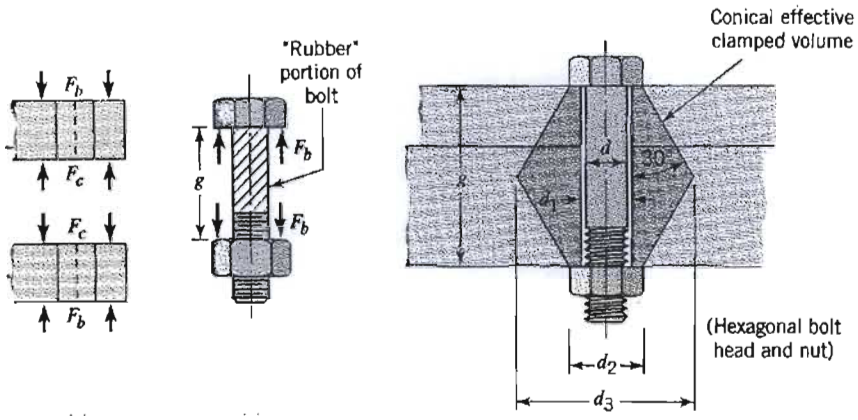

Figure 4.63: An approximation of the effective area of the clamped members. The area is roughly equal to the dark grey section [106]

The effective clamped area A_c in Figure 4.62 is defined by

$$A_c = \frac{\pi}{16}\left(5d^2 + 6dg + 0.065g^2\right) \qquad (4.6)$$

The effective area of the smart bolt (A_b), M11 x 1.5 with cut threads is taken as 65.90 mm^2, d (nominal diameter of the bolt) and g is taken as 72.7 mm

$$A_c = \frac{\pi}{16}\left(5x11^2 + 6x11x72.7 + 0.065x72.7^2\right)$$

$$A_c = 1061\,\text{mm}^2$$

Thus

$$K_c = \frac{1061x200}{72.7} \text{ and } K_b = \frac{65.90x200}{72.7}$$

So

$$R = \frac{2918.8}{181.29}$$

$$R = 16.1004$$

F_{emax} and F_{emin} are 50kN and 37.9kN respectively

Torque (T) applied to tighten the bolts was m

$$T - 0.2xF_i xd \tag{4.7}$$

$$F_i = \frac{20}{0.2 \cdot 11}$$

$$F_i = 9.091kN$$

Therefore substituting values of R, F_i and F_e into equations 5.5 - 5.6 and solving for F_{bmax} and F_{bmin}

$$F_{b\max} = 9.091 + \left(\frac{1}{1+16.1004}\right).50$$

$$F_{b\max} = 56.17kN$$

$$F_{b\min} = 9.091 + \left(\frac{1}{1+16.1004}\right).37.9$$

$$F_{b\min} = 44.78kN$$

Material physical properties:

Ultimate strength σ_{UTS} for M2BR = 1320MPa

Yield stress σ_y for M2BR = 1000MPa

Brinell hardness number $BHN = {}^{S_U}/_{3.45} = {}^{1320}/_{3.45} = 382.61$

The fatigue strength reduction factor for M11x1.5 ISO metric bolt thread, K_f, is for material with Brenill hardness greater than BHN 200 is 3.85

Thus the fluctuating stress experienced by the smart bolt was is expressed as

$$\sigma_{\max} = \frac{F_{b\max}}{A_s} \text{ and } \sigma_{\min} = \frac{F_{b\min}}{A_s} \tag{4.8}$$

The stress mean, σ_m and alternating stress, σ_a (stress amplitude), are expressed as follows

$$\sigma_m = \frac{(\sigma_{\max} - \sigma_{\min})}{2} \text{ and } \sigma_a = \frac{(\sigma_{\max} + \sigma_{\min})}{2} \tag{4.90}$$

Applying Goodman's equation, the equivalent strength required to determine the number of cycles to failure on log scale stress amplitude vs. number of cycles is expressed as follows [106]

$$Se = \frac{\sigma_a}{\left(1 - \sigma_m / S_U\right)} \tag{4.10}$$

Table 4.19: Calculated values of mean stress, alternating stress, equivalent stress, and the fluctuating stresses using residual stress method.

ID NO:	F_{bmax} KN	F_{bmin} KN	σ_{max} MPa	σ_{max} MPa	σ_{max} MPa	σ_{max} MPa	σ_a MPa	σ_m MPa	S_e MPa
1	56.17	45.86	3060.24	2441.91	1000.00	381.67	309.17	690.83	651.35
2	56.17	45.98	3075.43	2448.45	1000.00	373.02	313.49	686.51	655.92

At 10^6 cycles the endurance limit, S_n, for the machined smart bolt is expressed as

$$S_n = S_n' C_L C_S C_D C_T C_R C_G \tag{4.11}$$

where C_L is the load factor for axial loaded components, C_S is the surface finish factor, C_D is the diameter size effect factor, C_T is the temperature factor, CR is reliability factor and C_G is gradient factor [106].

Thus S_n' = 0.5 $S_{U,}$ C_L = 0.85, C_s = .65, C_D = 1, C_T =1, C_R = 1, C_G = 0.9

$$\Rightarrow S_n = 0.5 \cdot 1320 \cdot 0.85 \cdot 0.65 \cdot 1 \cdot 1 \cdot 1 \cdot 0.9$$

$$S_n = 328.16\,\text{MPa}$$

At 10^3 cycles

$$S_f = S_U \cdot C_L \cdot C_S \cdot C_T \tag{4.12}$$

$$S_f = 1320 \cdot 0.75 \cdot 1$$

$$S_f = 990\,\text{MPa}$$

Therefore the number of cycle to failure from the graph is estimated at 12000 cycles, appendix E

The fatigue test as previously discussed are normally conducted under tension-tension loading and these tests were carried out under constant cyclic amplitude until the smart stud failed. Figures 4.64 and 4.65 illustrate the quantitative relationship established between the number of cycles to failure and the change in inductance due to the irreversible transformation from austenite to martensite nucleation that occurred in the material.

The change in magnetic signature associated with the increase in the fraction martensite with increasing number of cycles to failure is displayed in the Figures 4.64 and 4.5. Table 4.20 shows the readings at the start and finish of each test for both washers, from which is can be seen that having the washer situated over the first threads produces a much better indication than at the groove beneath the bolt head. In addition the fractured stud can be seen in Figures 4.66 and 4.67, both of which fractured at the site of the first threads.

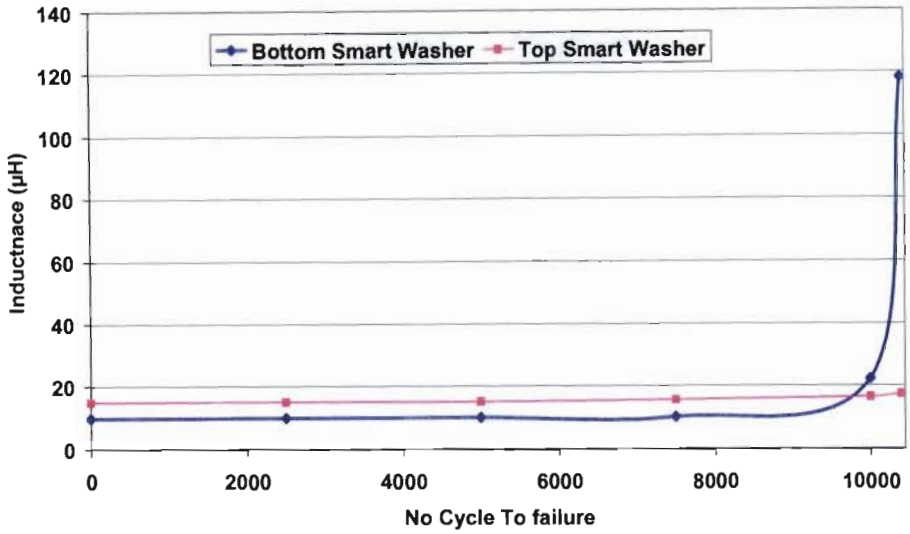

Figure 4.64: Change in inductance with respect to the number of cycles to failure of the smart stud specimen1

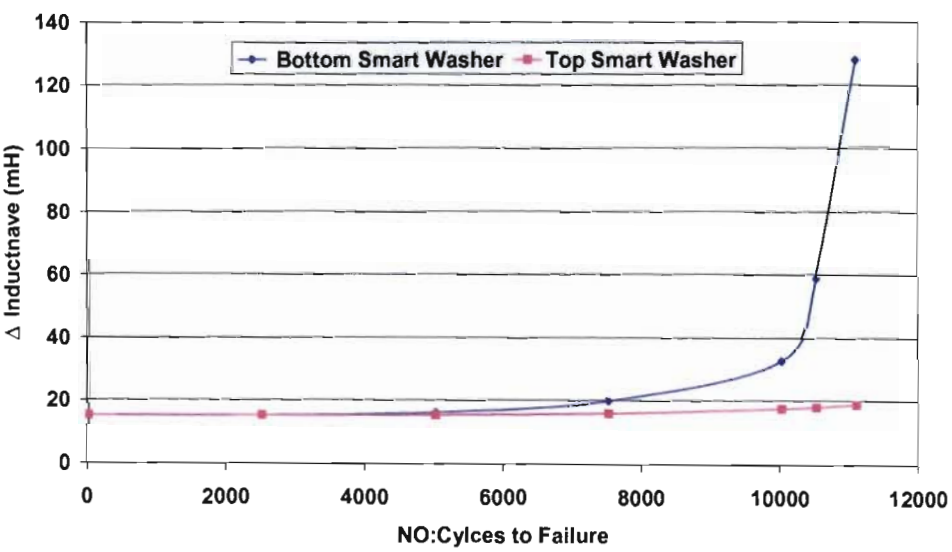

Figure 4.65: Change in inductance with respect to the number of cycles to failure of the smart stud specimen 2

Table 4.20: Overall view of the change in inductance to NO: cycles to failure, Cycle Loads

ID NO:	Initial Inductance Top Smart Washer (µH)	Initial Inductance Bottom Smart Washer (µH)	Final Inductance Smart Top Washer 1 (µH)	Final Inductance Smart Bottom Washer 2 (µH)	Number of Cycle To Failure
1	15.2	9.9	16.1	118.2	10394
2	15.17	15.18	18.87	126.8	11080

Figure 4.66: Brittle fractured surface (picture A) of the smart stud occurred at the first thread in contact with the locking nut (picture B) sample1

Fracture occurred at the 1st threads of stud in contact with the first threads of the lock nut. Also displayed are beach wave on the fracture surface

Figure 4.67: Brittle fracture of test sample 2 of the fatigue M2BR smart stud.

After fracture, samples were cut from the fractured specimen close to the fractured areas. The metallographic results obtained are displayed in Figures 4.68 and 4.69. Figure 4.68 displays the microstructure of the first stud taken at 400X optical magnification, the microscopic structure displayed denser dark regions of strain-induced martensitic precipitation along the slip planes with returned retained austenite (yellowed regions, coloured regions) with a massive crack. Figure 4.69 also displays dense dark regions of strain-induced martensitic precipitation along the slip planes with returned austenite (yellowed coloured regions) as that of Figure 4.68.

Figure 4.68: Microstructure of fatigue M2BR stud 1, micro photographed at 400X optical magnifications

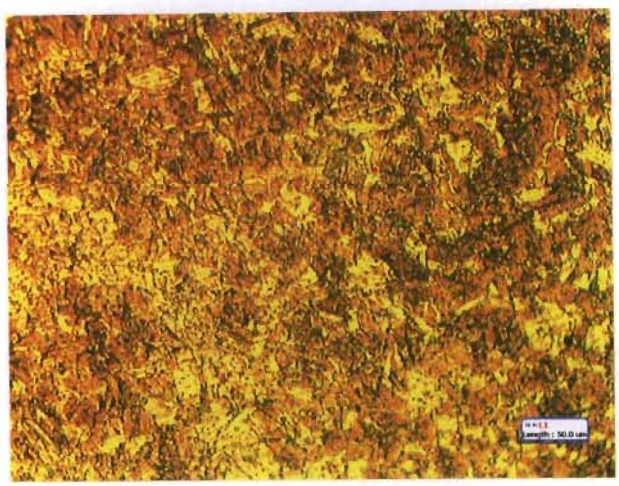

Figure 4.69: Microscopic structure of M2BR Stud 2, micro photographed at 400X magnifications

4.4.3 Smart washer Cyclic Fatigue Temperature testing

The objective of testing the smart washers at both lower and higher than room temperatures, was to determine whether the washer themselves were in any way affected by the variation in temperature that would be produced by take-off, flight, landing and airfield-apron time. The alloy used in this case was the M2BR alloy. Also M2BR has a similar composition to alloy 2 and is more stable. Therefore the cycling temperature and fatigues testing of M2BR TRIP steel studs may or may not produce any change in magnetic signature at low

temperature. Before testing the studs and smart washers, the smart washers themselves were immersed in the cryogenic chamber and then cycle tested between a temperature range of 51.3°C and -47.8°C for a twelve hour cycle. The inductance of the coil was measured and no change in the coil inductance was found, implying that the 316 stainless (used as the body of the washer and the housing of the coil) did not itself produce thermal martensite. The question then remained as to whether the coil would perform at low temperatures.

The temperature cyclic testing of the two studs manufactured of M2BR alloy material was carried out in two phases; the first phase involved cycling the smart stud between 51.3°C and -47.8°C under no external load. In the second phase the studs were tested under the same cycling temperatures, but this time a 55kN external load was applied. In both cases the change in inductance of the two smart washers placed over the first top thread(s) were then measured frequently as explained in chapter 4, section 4.3.7. The specimens (studs) were subjected to 51.3°C for 12 hrs and then -47.8°C for another 12 hrs cycle period for two days. The results obtained were as follows:

Table 4.21: Inductance change of smart washers at different temperatures and load

Sample ID	Temperature °C	Inductance Top Smart Washer (mH) Day 1	Inductance Bottom Smart Washer (mH) Day 1	Inductance Top Smart Washer (mH) Day 2	Inductance Bottom Smart Washer (mH) Day 2	Load kN	Stress MPa
	25.4	15.19	15.18	15.19	15.20	0	0.00
1	50	15.19	15.18	15.19	15.20	0	0.00
	-47.5	15.19	15.18	15.19	15.20	0	0.00
	25.4	16.83	16.81	16.83	16.82	55	760.72
2	50	16.83	16.81	16.83	16.82	55	760.72
	-47.5	16.83	16.81	16.83	16.82	55	760.72

Figures 4.70-4.71 show the correlation established between the changes in inductance with respect to cycling temperature for both specimens under zero loading and under 55kN static loading.

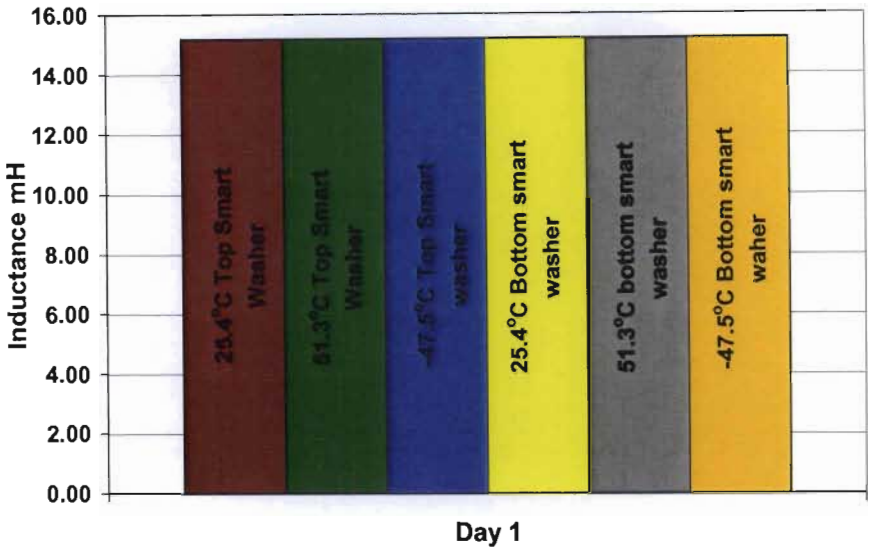

Figure 4.700: Constant level of inductance for both smart washers with respect to cyclic temperature testing (51.3°C and -47.8°C) on day 1, zero loading

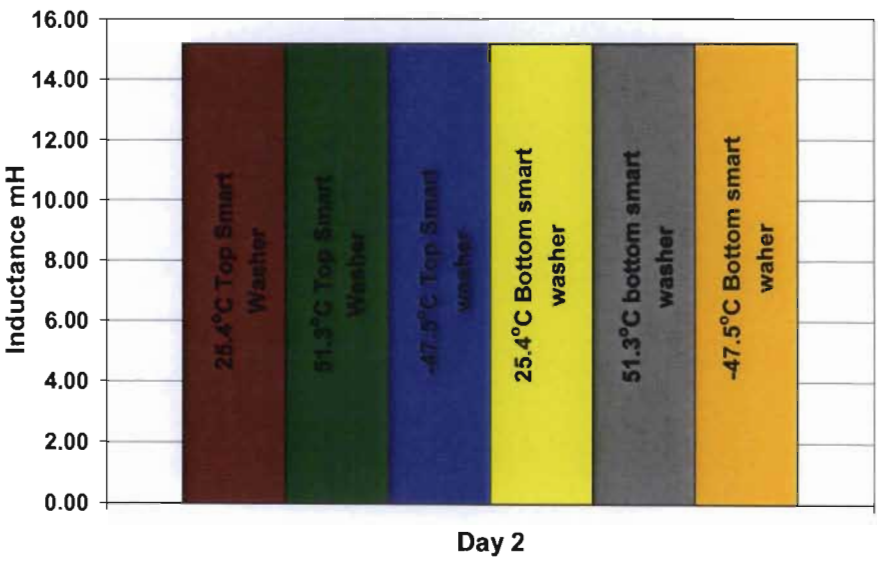

Figure 4.71: Constant level of inductance for both smart washers with respect to cyclic temperature testing (51.3°C and -47.8°C) on day 2, zero loading

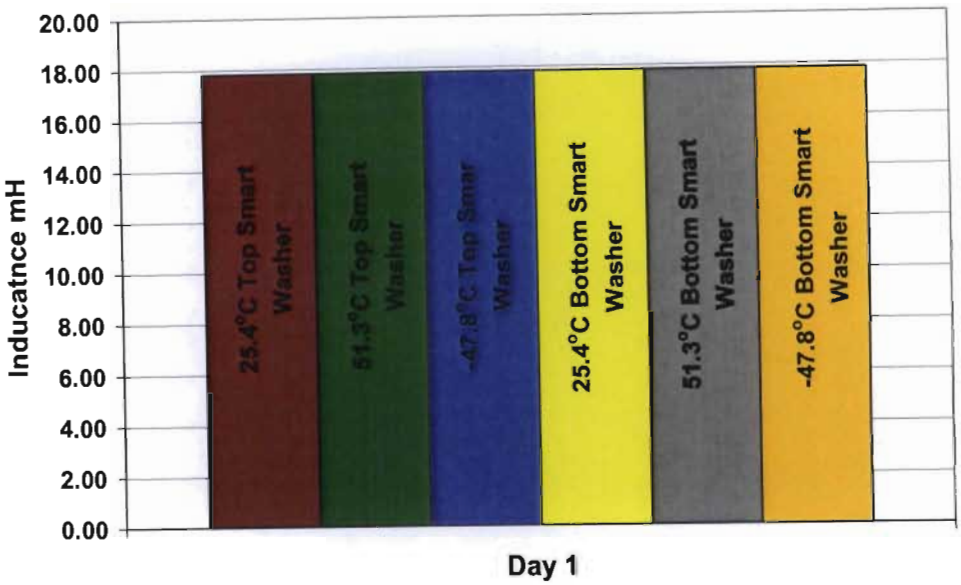

Figure 4.722: Constant level of inductance for both smart washers with respect to cyclic temperature testing (51.3°C and -47.8°C) under 55kN static load on day 1

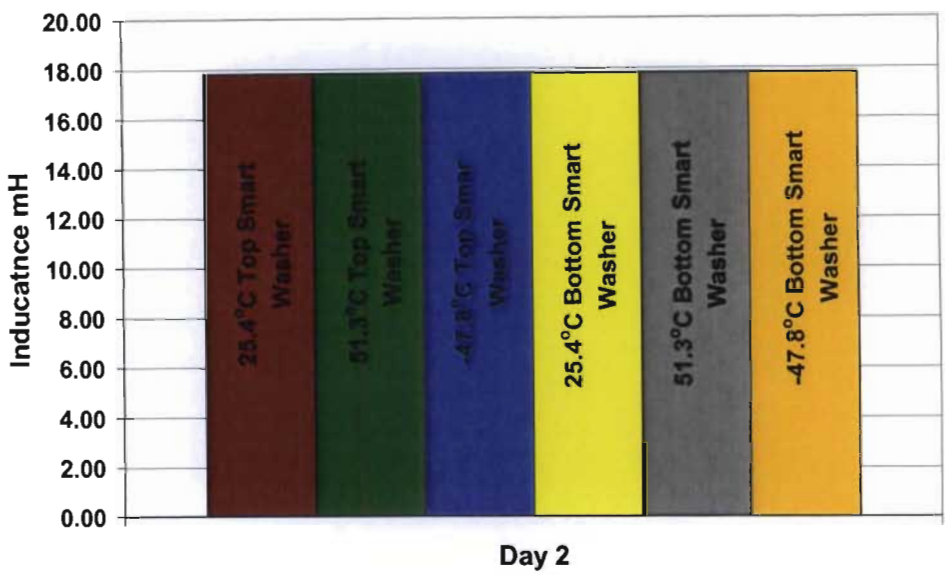

Figure 4.73: Constant level of inductance for both smart washers with respect to cyclic temperature testing (51.3°C and -47.8°C) under 55kN static load on day 2

Samples were cut off from the temperature cycled specimen in areas close to the first load carrying thread and their microstructure was analysed. The metallographic results obtained are displayed in Figures 4.74and 4.75 taken at 400X optical magnification. Picture A of Figure 4.74 shows the microstructure of an untested specimen at room temperature, which is identical to the microstructure obtained for the sample cyclic temperature tested at (51.3°C and -47.8°C) under

no load. The specimen in picture be was tested for 12 hr period, for 2 days with no external load applied. In both pictures, is clear that a small amount of martensite is visible along slip planes. Figure 4.75 shows the incremental increase in martensite precipitation, with retained austenite (yellowed regions) for the smart stud cyclic temperatures (51.3°C and -47.8°C) tested under a constant 55kN static load.

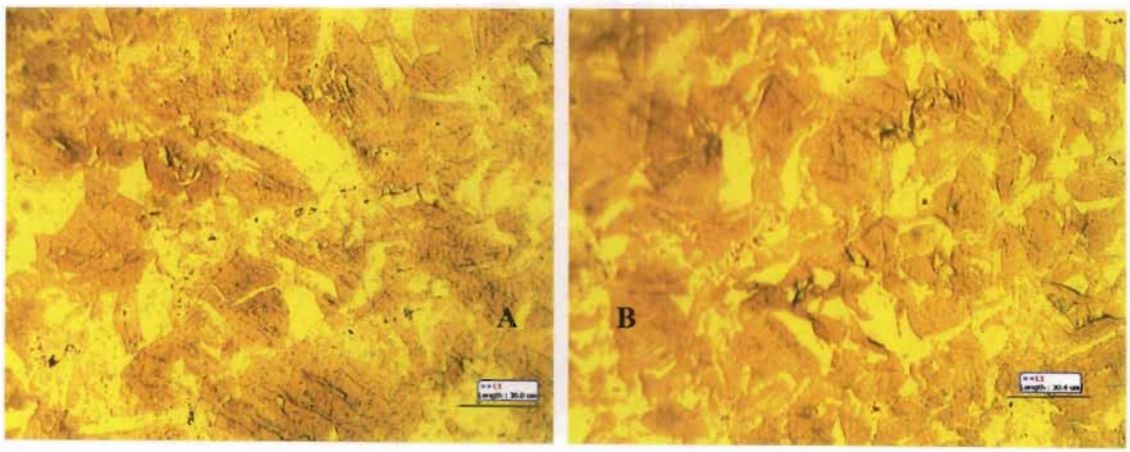

Figure 4.74: Microstructures of untested sample 1, picture A, and cyclic temperature (51.3°C and -47.8°C) tested sample 1, picture B

Figure 4.75: Microstructure of cyclic temperature (51.3°C and -47.8°C) test sample 2, tested using a constant 55kN static load

4.4.4 Discussion

The data obtained from the tensile testing of the smart aircraft bolt manufactured from the MB1 TRIP steel alloy clearly indicated that, firstly the transformation occurred significantly at the top thread root (measured by the smart washer place over the top thread(s)), as compared to the

washer placed underneath the bolt head. Secondly, although the magnetic measurement were made on the lateral surface of the test section (smart washer placed over the first two-three threads, butting up against the locking nut) adjacent to the fracture surface, the smart washer placed over the top thread(s) measured the change in inductance resulting from the phase transformation of the parent phase austenite to product phase metastable martensite at low incubation strains, i.e., the change in ferromagnetic response occurred within the elastic region, displayed in Figures 4.54-4.55.

The optical metallographic results obtained of the smart bolts, Figures 4.58-4.59 confirmed the indication of magnetic detection by the smart washers for the incremental increase in martensitic precipitations. In addition, from the untested specimens, the metallographic images of the samples showed minute traces of martensite. However, samples cut from the tensile tested studs displayed a duplex microstructure with dense dark lenticular form of martensite precipitated along the slip bands with retained austenite (yellowed regions) confirming that transformation had occurred.

From the experimental data obtained from the tension fatigue testing of the smart studs, the change in inductance recorded from the smart washers showed that the inductance increased with increasing number of cycles to failure of the smart bolt, illustrated by Figures 4.64 and 4.65 of the two studs. This is attributed to the martensite nucleation that increased progressively during the fatigue testing. In addition, the metallographies of the smart stud manufactured from M2BR TRIP steel alloy clearly showed a substantial increase in the dark dense region due to strain-induced martensitic precipitation along the slip plane. Illustrated in Figures (4.68 -4.69) are bands of martesite roughly parallel to the fractured surface, this indicates that the state of stress if plane strain. The precipitation of martensite locally destabilizes the austenite resulting in the serrated appearance. The reason for this is the general inhomogeneous precipitation of matensite which laid in the volume increase associated with transformation. Furthermore, regions in-between probably have significant hydrostatic component of stress which tend to suppress the transformation.

Results obtained from the cyclic temperature testing showed firstly that the smart washer does not in any way interfere with the damage detection process (even at very low temperatures). Further, the results from the testing of the smart stud under no static load and under a constant static load have been presented and have revealed that, firstly for the cyclic temperatures testing under no load, there was no change in inductance registered by the smart washers over the two day testing period, regardless of whether the temperature registered was 50°C or -47.8°C as

illustrated in Table 4.21, Figures 4.70-4.71 and by the metallographic results of Figure 4.74. However, Figure 4.75 indicates a substantial increase in lath martensite along slip planes, when compared to Figure 4.74 for the smart stud subjected to both cycling temperature loading and an external static load of 55kN. The material transformed substantially as illustrated in Figure 4.70-4.71 and Table 4.20. But the change in inductance remained constant throughout the cyclic temperature loading. Therefore the increase in inductance and increase in martensite nucleation in the microstructure (Figures 4.72-4.73) is attributed purely to the external load applied. Thus the smart washer performs its function perfectly regardless of the service temperature range of the aircraft

The martensite morphologies of both the studs fatigue tested and temperature cycled when observed indicated that the martensite morphology was driven by stress state (plain strain) because the planes of maximum shear lay at roughly 45° to fracture surface, i.e., when viewed on the plane perpendicular to the direction of the fractured surface, such plane appeared to be lines roughly parallel to the fractured surface

The smart washer as a concept has therefore shown itself to operate without interfering in the damage detection, across all temperatures of the aircraft's service temperature range, and when placed over the first threads easily detects the damage induced both by static and dynamic loading conditions.

The evaluation of a smart washer concept proved that concept worked, through fatigue testing and cryogenic testing of the smart studs manufactured in limited quantity. The replacement material, M2BR TRIP steel proved as stated before to be metastable in its parent austenite phase at low temperatures. Also the alloy (M2BR) displayed the ability to transform from paramagnetic austenite phase to a ferromagnetic martensite product phase with minimal incubation strain period, which took place below the alloy yield point. High strength level (compressive strength) was also noted. These characteristics displayed by M2BR are identical to those displayed by alloy 4, the alloy intended to be further testing and validation of smart washer concept. Both alloys, alloy 4 and M2BR met the strength criteria and the magnetic response required to give these alloys their unique ability to be utilised as a damage sensor.

CHAPTER 5

Simulation of the Mechanical Model and Magnetostatic Model of the Aircraft Bolt

5.1 Introduction

The simulation of the mechanical response model and magnetostatic response model was carried out in two stages. The first stage involved creating the geometry (mechanical model) of an altered 19 mm diameter smart aircraft bolt based on actual bolt geometry, defining mechanical properties (stress-strain) of the TRIP steel (MB1) alloy, then simulating where the martensitic nucleation will occur and the quantity as a function of applied loading through the use of transformation kinetic model for TRIP steel alloys. Finally the model will be executed as a nonlinear material analysis using the transformation kinetic model for TRIP steels. The output mechanical model from FEA will essentially be used as the base input model for magnetostatic response model (FEMM), the second stage of modelling. The base model will then need to be modified in order to integrate the magnetic permeability (resulting into change in inductance) of the TRIP steel smart bolt material, which will have to be adjusted for each loading increment and for the corresponding calculated amount of martensite precipitated within any point in the smart aircraft bolt. The site(s) where martensite will precipitate are vital for the positioning of an interrogating system (smart washer). Note that transformation occurs at high stress, localised area. Two positions (underneath the bolt head and over the first thread(s)) for smart washer application were investigated

5.1.1 Mechanical Geometric Model

The smart aircraft bolt geometry was modelled as half cross section of the smart bolt using plane strain triangular element properties. The work plane for the model was rotated and aligned so that the geometric model resided in the positive ZX-plane required by MSC. Nastran, with the z-axis being the centre line for axisymmetric modelling. Also the helical nature of the threads were assumed to be negligible, which more importantly required less analysis time. This also helped decrease the file and model size. The geometry of the bolt was altered in order to

include an undercut (stress concentration) just before the first thread. The undercut helped improve and promotes strain induced matensitic precipitation which gave the best possible site for a smart washer (sensor) to be applied. The geometry of the bolts used, as well as the finite element model mesh can be seen in Figures 5.1 and 5.2 below.

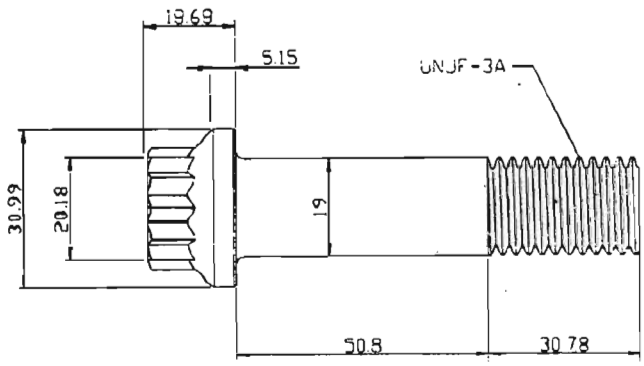

Figure 5.1: 19mm, 16 threads per mm aircraft bolt modelled for the mechanical model

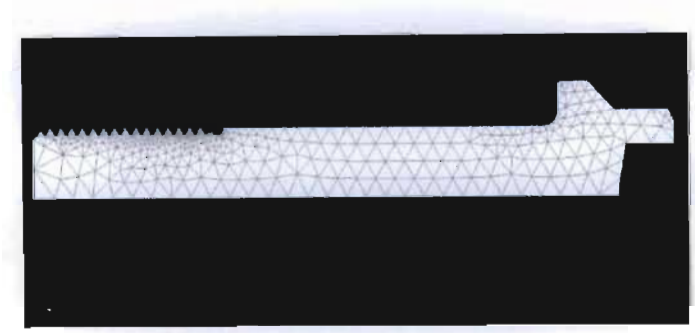

Figure 5.2: Finite element mechanical model of the Smart aircraft bolt

5.1.2 Defining Model function, Model Material and Model Property

The strain-induced nucleation of martensite occurs inhomogenously, and the region where martensite has formed becomes stronger than any other region. For this reason a model function defined by the stress-strain data obtained from the tensile test of the MB1 TTRIP steel material was created, which defined the properties of the material. The tensile specimens were machined from the material and tensile tested at various pre-determined strains, whereupon the test was stopped and the specimen cut (in the centre), polished and etched using the method described in chapter 4. Representative microstructures were recorded and analysed using Motic Image Plus 2.0 (a metallurgical image analysis software package). A curve of percentage martensite vs.

strain could be constructed from this visual data. Some of the representative microstructural images are presented in Appendix B. Figure 5.3 below shows some of the raw data used to construct the material's non-linear plasticity characteristics. Other material data from the tensile test, such as Young's modulus and yield strength were also utilized to characterise the material. Although MB1 and alloy 4 do not have equivalent mechanical properties or transformation characteristics, MB1 data was used to illustrate the modelling methodology. Figures 6.3 and 6.4 show the model function and material input screens. Plane-strain linear triangular element property types were defined for the selected model material.

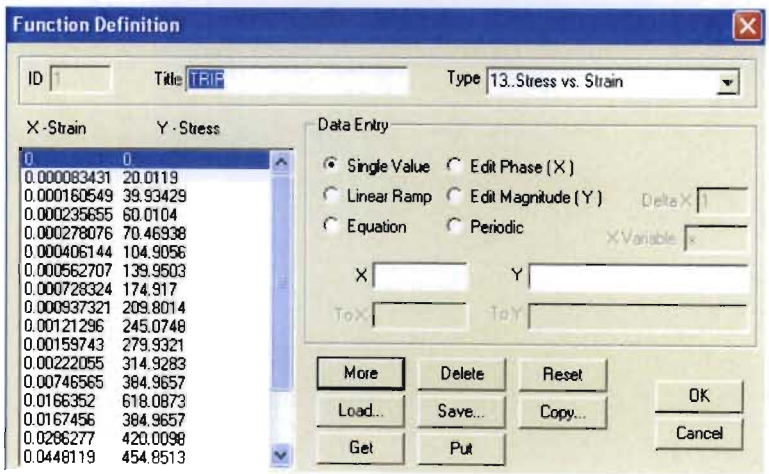

Figure 5.3: **Model function definition of the stress-strain curve for MB1 of the TRIP steel material defining elasto-plastic properties of the modelling smart bolt**

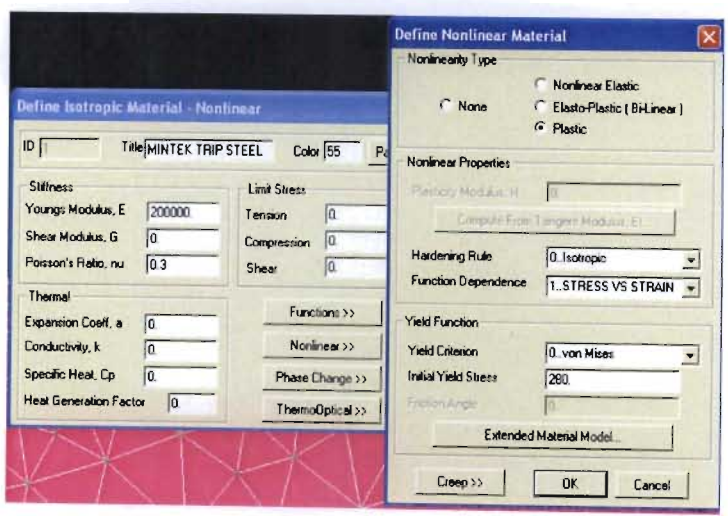

Figure 5.4: **Isotropic and nonlinear material properties of the smart bolt**

5.1.3 Meshing geometry

The numbers of elements along the curves, outlining the boundary were then seeded. This also helped orientate the elements, and space out the elemental nodes equally along the top of the threads, while the element spacing was more biased towards the root circle at the base of the thread root and underneath the bolt head. This approach was used because these are areas were the highest stress concentrations exist (promotes phase transformation in an area that favours the sensor positioning), thus this method made it possible to model what is happening in that region with greater accuracy. In areas of less interest, fewer elements are used and were more widely spaced. Once the above mentioned steps were completed, a boundary surface was created from all the curves. The surface was then meshed using non mid-node triangular elements defined by the model property and the cylindrical co-ordinate system required for axisymmetric analysis.

5.1.4 Model Constraints and Model Load

A constraint set was first created. A set of constraints was applied along curves or nodes on the left-hand side flanks of the threads to simulate the sliding action between the bolt threads and those of the nut. Then X symmetric constraints were specified along the centre z axis of the smart bolt model. Like the constraint set, a load set was defined. Non-linear loading (load increments set to 33) analysis static axial load was applied to the nodes of the curve underneath the bolt head. This was done because the non-linear incremental solution carried out different advancing schemes, different iteration schemes, and different convergence criteria to obtain a solution for each incremental load. The magnitude of the load applied (taken from the mechanical data obtained from tensile testing of smart bolt) was also just sufficient to move the material into the plastic region of the stress-strain curve and allow it to undergo permanent deformation.

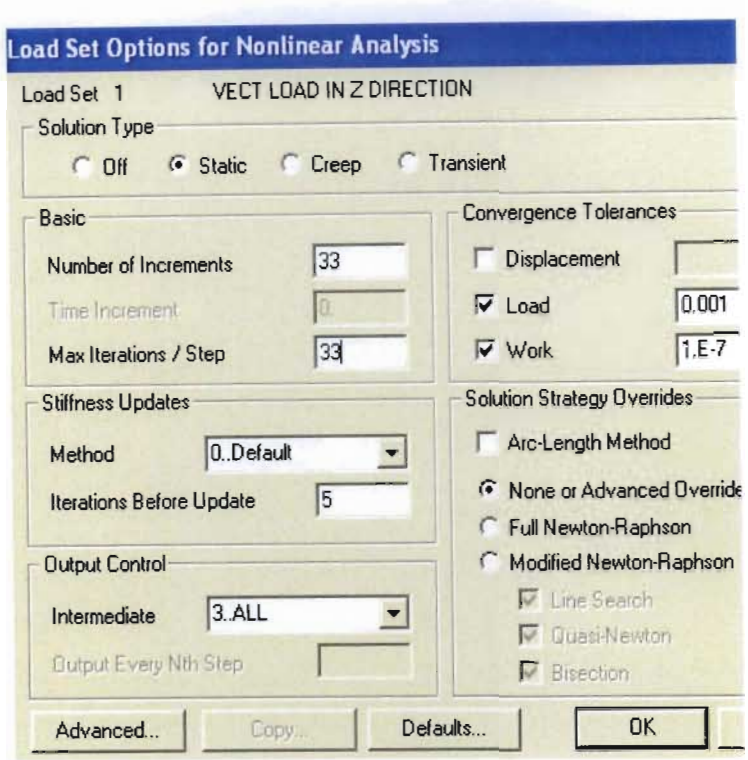

Figure 5.5: Displays the load set option for nonlinear analysis

Once the above steps were completed the model was then executed as a nonlinear static analysis. Another output vector set was created which incorporated the transformation kinematics modelling equation defined by the Olsen and Cohen model. The numbers of output sets which calculated the volume fraction of martensite, based as a function of plastic strain corresponding to a particular load increment, was noted. A new output set was created defined by the Olsen-Cohen transformation model (evolution of martensite as a function of plastic strain), as explained by equation 3.11 in chapter 3. The identity (ID) of the vector containing the martensite volume fraction data was noted. A graph of martensite volume fraction of strain was developed from tensile tested MB1 TRIP steel. Then a second graph of martensite volume fraction using Olsen-Cohen was plotted and mapped onto the first graph of martensite volume fraction (metallographically determined appendices A and B) to obtain a best fit. This meant that the values of α and β were determined by plotting best fit curve and superimposing Olsen-Cohen model (graph) to that (graph Mart_vol_frac-strain) determined from the microstructure. The value of α and β determined were 2.935 and 35.13 respectively, for n = 1.1. The two models are shown below as flows

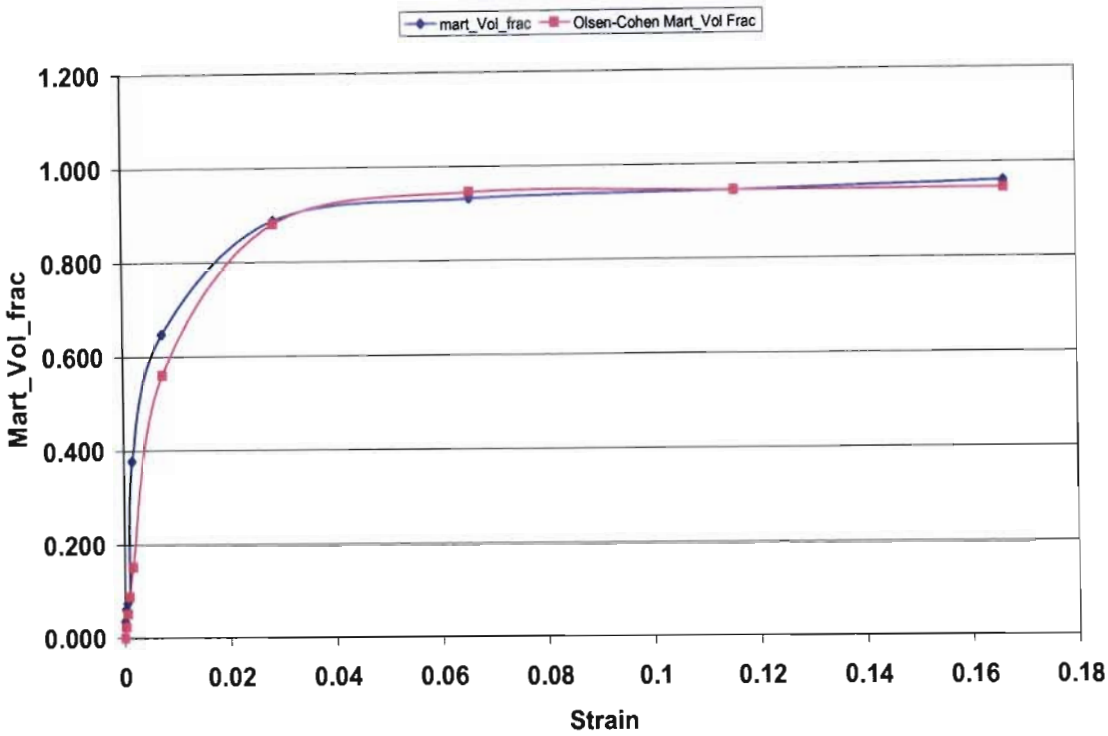

Figure 5.6: **Olsen-Cohen model superimposed to on the model calculated from the amount of martensite for each individual microstructure obtained for each tensile tested specimen**

A nonlinear analysis was implemented on the mechanical model. As mentioned previously, the nucleation of martensite occurs inhomogenously, as the region where martensite nucleates first becomes stronger than any other region and is associated with brittle failure without any form of necking being (tensile Results chapter 4). In the case of the smart bolt, the nonlinear static analysis showed the location where bolt failure would take place. The mechanical model also showed the site(s) where strain-induced transformation is likely to take place and this was found to be at the same location where the bolt failure would occur, at the thread roots of the top thread(s), illustrated in Figure 4.15, which also determined the region where smart washer (sensor) should be positioned.

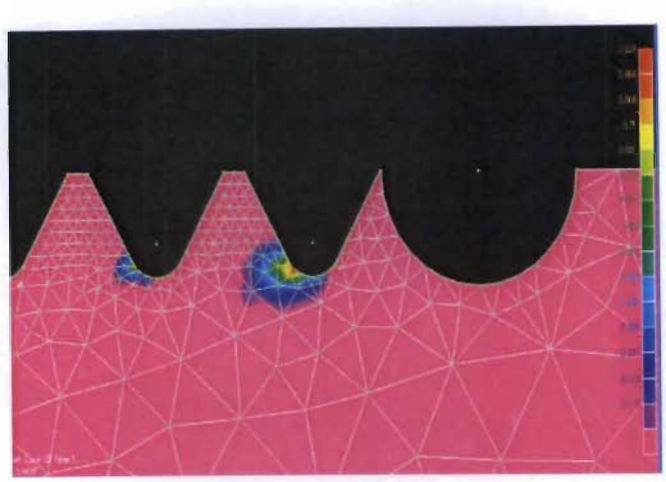

Figure 5.7: **Region of failure determined at the first thread root, and best possible site for sensor positioning**

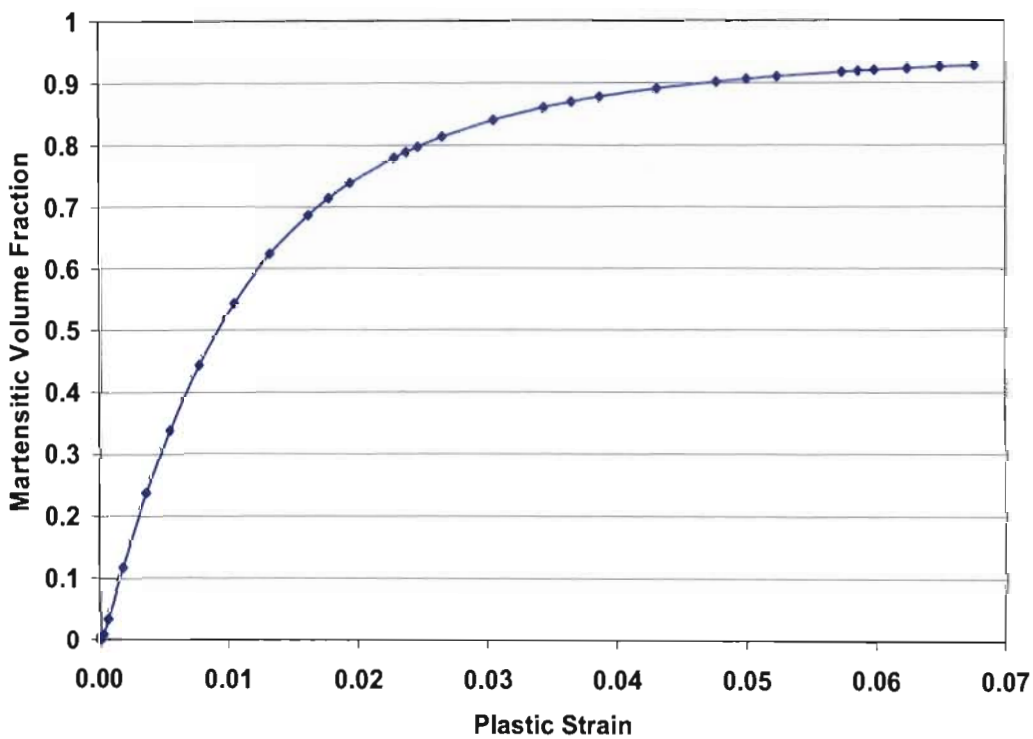

Figure 5.8: **Martensitic volume fraction deduced as a function of plastic strain for Mintek TRIP steel alloy at 298K derived from mechanical response model**

All the work carried out was done and saved in one special working directory, and all the FEMM and MSC/Nastran for windows script files were also saved in this very same working directory. Finally a nastran_to_FEMM MO.bas script file application program file was executed in nastran with a modified number output sets and output vector ID variables of the martenite

volume fraction, so that they reflected the values of the number of output sets incorporating the Olsen-Cohen transformation output model and its vector ID, which created and returned the volume fraction of martensite transformation for each elemental (MB1 TRIP steel data) data for geometric extraction for FEMM analysis, for multiple output sets.

5.2 Magnetostatic Response Model of Aircraft Bolt

The mechanical response model as stated above was then used to model the geometry, nonlinear mechanical characteristic of MB1 TRIP steel, best possible site for sensor application and the magnetic response of the smart aircraft bolt. The output set of the mechanical model provided the input magnetostatic response of the smart aircraft bolt Model. A lua script file (mod_input.lau) in association with geo_extract .out file was utilized in FEMM to create a base geometry and material set (MB1 TRIP steel alloy and magnetostatic response properties) for each element in any vicinity of the smart aircraft bolt geometry. FEMM was utilized in order to deduce the change in material permeability (change in inductance at various tensile nonlinear loading). The smart bolt model was centralized in the semi circular domain in order to allow accurate and practical modelling of the magnetostatic response of the Smart aircraft Bolt.

5.2.1 Material Properties and Boundary Conditions

The geometric model of the aircraft bolt (smart memory alloy) was positioned in the centre of a semi-circular domain to emulate a reasonable simulation of far field effects. Two new block material sets (copper coil block material and air block material) were then added to the geometry within the defined boundary of the problem domain, with defined material properties. In the first model, the coil block replicating the smart washer (ID 12mm, OD 22mm by 4mm thickness) was modelled over and along the bolt shank, over the undercut, and over top thread(s). The empty space was modelled using air block material property. In the second model, using the exact material properties and boundary conditions, the copper coil was placed underneath the bolt head to model the change in inductance of the smart bolt. In both models, an arbitrary set of co-ordinates within the domain representative of the measurement coil included a current density J, was randomly specified, which was later used to calculated the change in inductance (magnetic response) due to the change in bolt localized material permeability because of the nonlinearity of TRIP steel's martensitic nucleation within smart aircraft bolt (strain memory alloy) deduced from nastran, i.e., calculating the AJ block integral for the coils. The change and strength in inductance of the coil was evaluated by integrating the AJ block with respect to current I flowing through the coil as follows

$$L = \frac{\int A \times J dv}{i^2}$$

The Mvf_input.lua script file was executed in order to create separate FEMM models (33 models in this case were created) for each load increment, i.e., this updated the material sets and transformation kinetics for each elemental region for a specific amount of martenstic for a each specific nonlinear incremental load set.

In order to simulate the change in inductance, two sets of boundary conditions were applied. For the first, the boundary condition was defined so that the magnetic flux lines never crossed the longitudinal axis of the symmetry (Robin boundary condition described in chapter 2). This implied that both A and *r* values were equated to zero.

The second of the boundary conditions was defined by an asymptotic boundary condition which allowed modelling a suitable approximation solution to an open boundary condition. As explained in chapter 2, [section 2.5.3.2] since the outer edge of the solution domain was circular, Radius *r*, the outer finite element boundary was removed from the area of primary interest and the open domain solution was then closely approximated by applying equation (2.56) to the circular boundary. The asymptotic boundary conditions for this case was be defined as a Robin boundary condition of the form

$$\left(\frac{1}{\mu_0 \mu_r}\right)\frac{\partial A}{\partial n} + c_0 A + c_1 = 0$$

where

$$c_0 = \frac{1}{\mu_0 r}$$

$$c_1 = 0$$

μ_o and μ_r are defined as the permeability of air and core material respectively. R is the radius of the boundary domain.

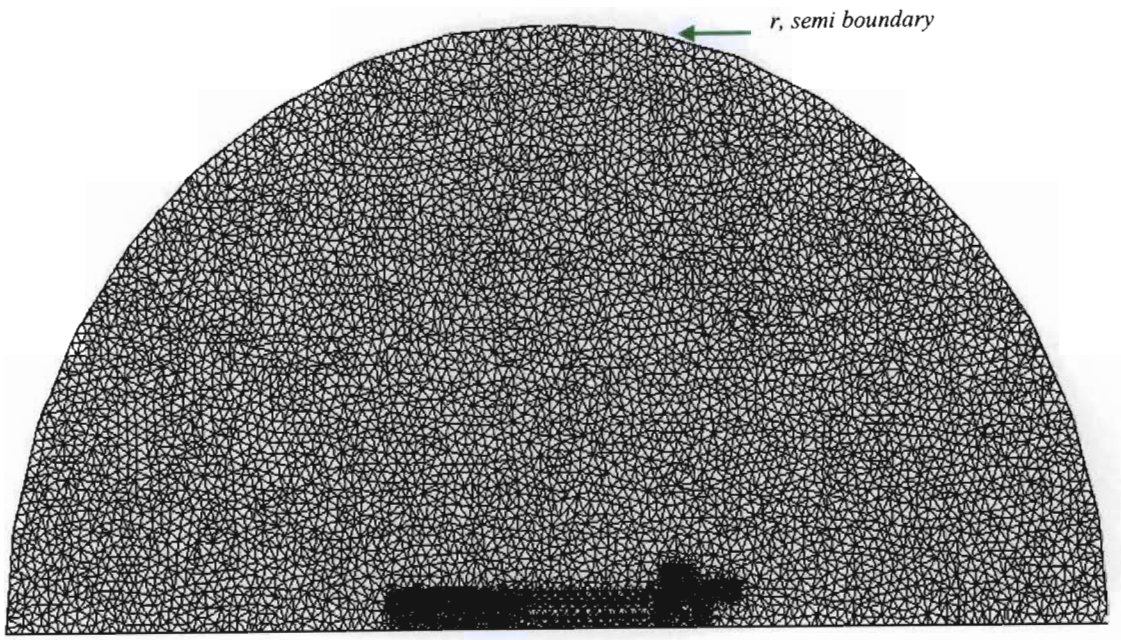

Figure 5.9: Domain in which the mechanical model of Smart bolt used to model the magnetostatic model of Smart aircraft bolt

Once the above steps were finalized, and the coordinates of any point within the boundary of the coil block noted, a lua script file: ananlyse.lau file was run to analyse each of the FEMM models created and in turn calculates their block integral for the measurement coil. The data from the analysis was written to a post_pro.output file, and was read off using note-pad. Note: lua is a powerful, light-weight extension programming language assigned for any program that needs one. However, lua programming is not the focus of this thesis.

5.3 Results and Discussion from Mechanical Model and Magnostatic Response model

The precipitation of strain-induced martensite shown by the mechanical model and corresponding changes in flux density determined from the magnestostatic response for the smart bolt (strain memory alloy) subjected to tensile loading are illustrated in Figure 5.10. The mechanical response model results obtained revealed that the best site for a smart washer to be positioned to measure the change in inductance due to the change in the material permeability proved to be at the top thread engaged to the washer, more so on the first thread root as this is the area where highest transformation would occur. However, from the data collected from the tensile testing of the smart bolts, the change in inductance observed by the smart washer placed underneath the bolt head closer to the shank-head fillet was far less than that of the smart

washer placed over the first two threads. Thus in the magnetostatic model, a block coil was also placed underneath the bolt head and the change in inductance change measured and compared to the magnetostatic model with the coil placed over the root of the first thread. It was clearly observed that the change in inductance for the magnetoastic model with the coil placed over the first thread root was far greater than measured at the shank-head fillet. Figure 5.9 shows the difference in change inductance

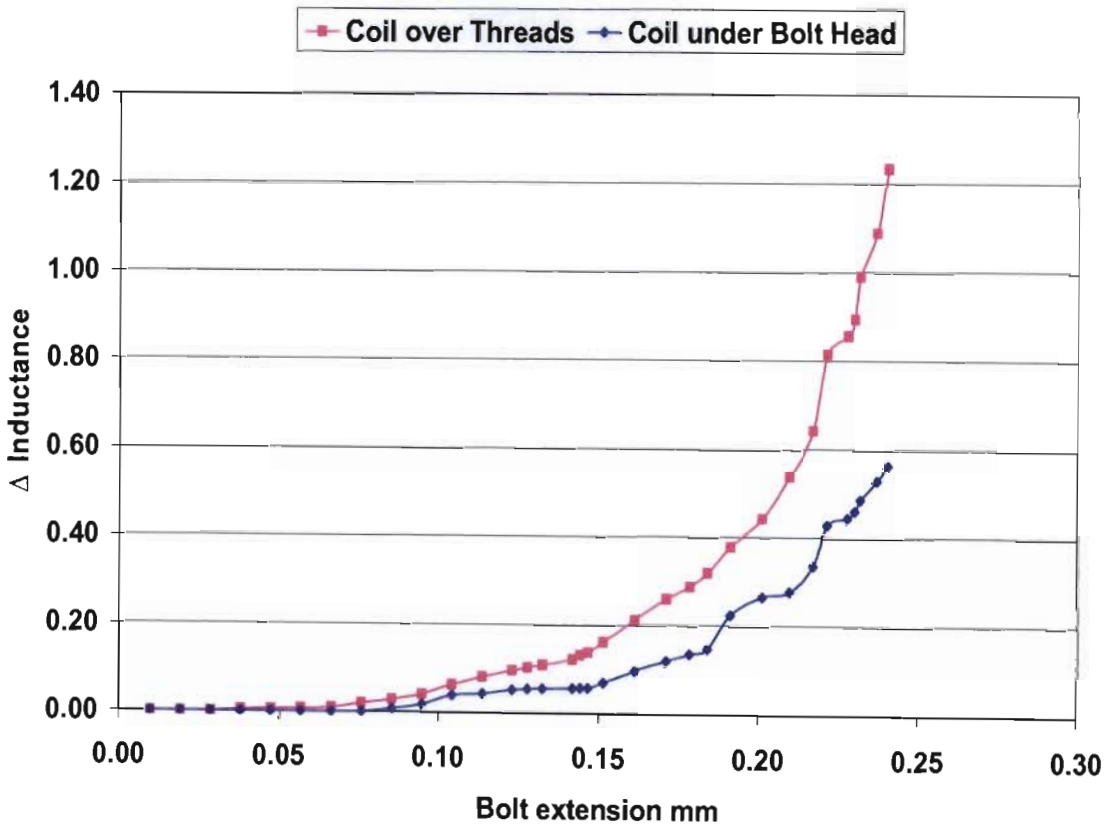

Figure 5.10: Difference in the inductance change-bolt extension between the smart washer coil placed underneath the bolt head and that of the coil placed over the top thread root

The incremental increase in strain-induced martensitic transformation sites are clearly show in Figure 5.11, for the varying bolt extension. Figure 5.11 shows that the best possible site is at the first thread root, just after the undercut, that act as a stress raise thus promoting strain-induced transformation to take place.

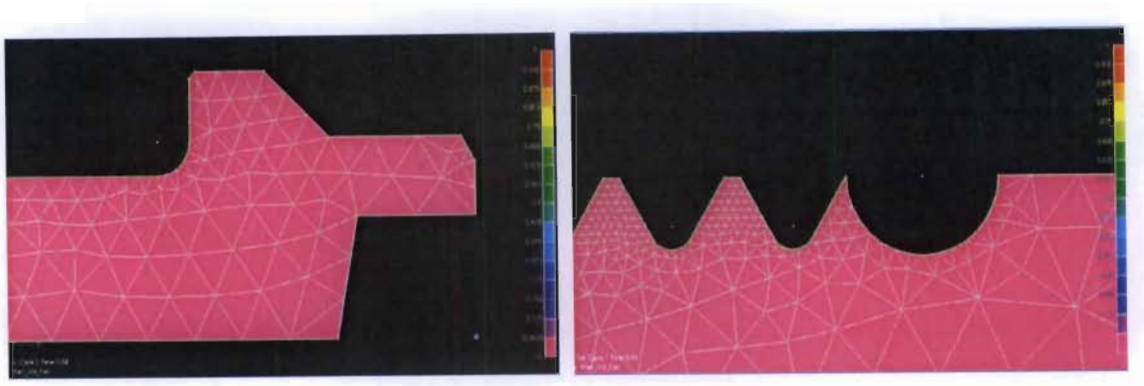

Bolt extension 0.00942133mm

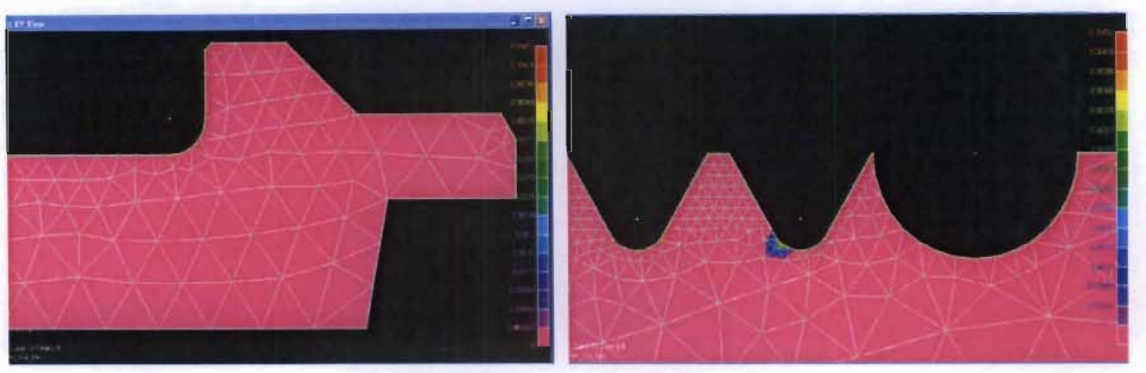

Bolt extension 0.0943627mm

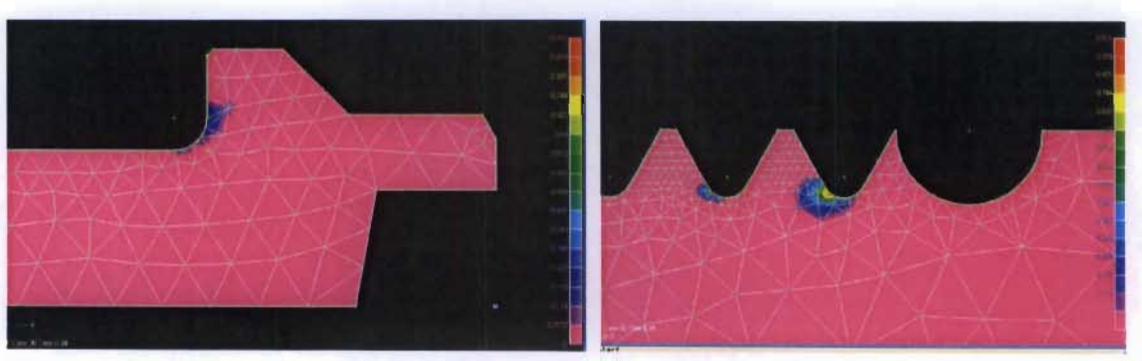

Bolt extension 0.226162mm

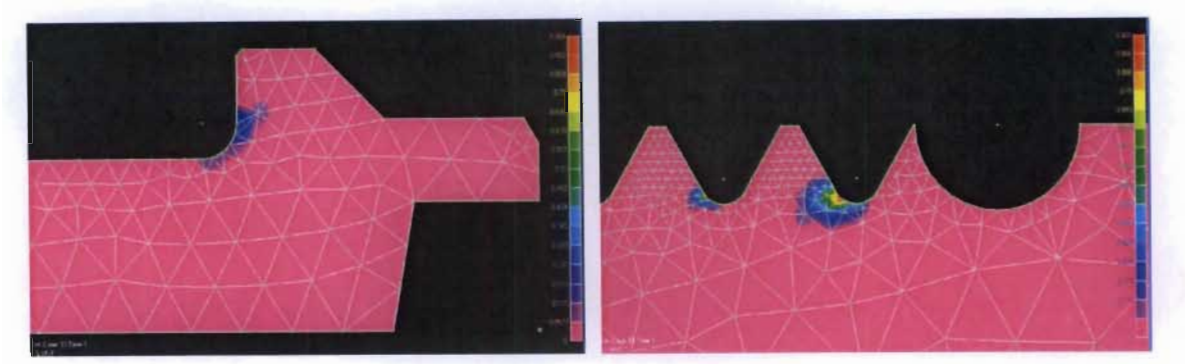

Bolt extension 0.241666mm

Figure 5.11: Incremental increase in martensitic volume fraction at the top thread(s) root, with increasing bolt extension.

The changes in the flux density of the material associated with the change in permeability of the smart bolt (strain memory alloy) especially at the thread root areas, due to the incremental increase in strain-induced matensitic precipitation (increase in martensite volume fraction) with increasing bolt extension are illustrated in Figure 5.12. In addition, from Figure 5.12, it was clear that with increasing bolt extension resulting from the increase in loading, the region at the thread root, especially at the first thread root, (the triangular element determined from mechanical model, Figure 5.11), in this region showed an increase magnetic flux density due to the significant increase in the amount of martensite, thus the most suitable area for transformation to take place.

Bolt extension 0.00942133mm

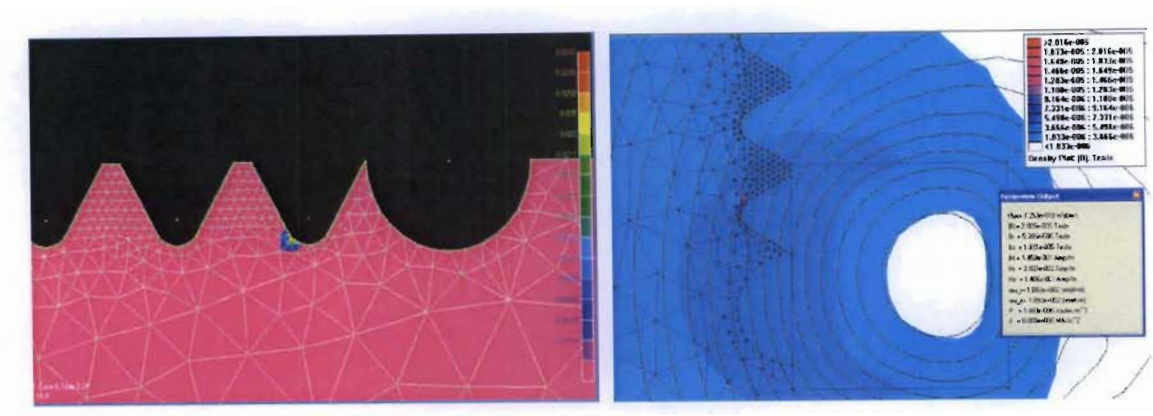

Bolt extension 0.0565604mm

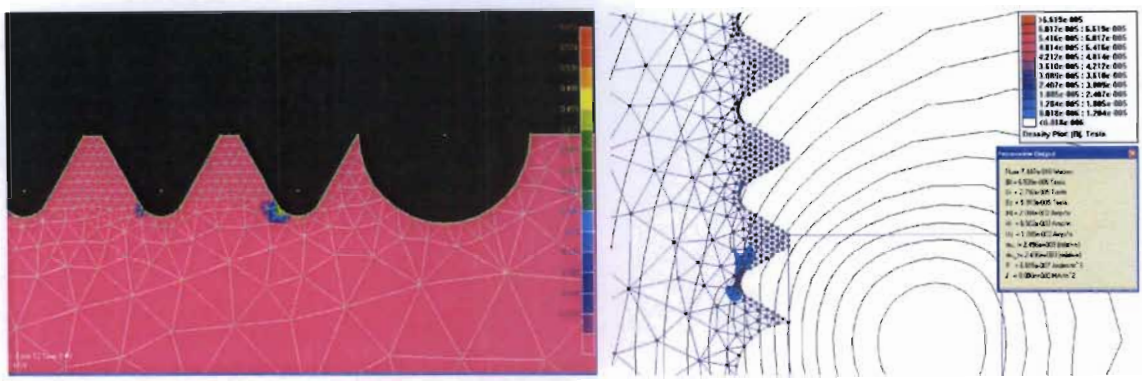

Bolt extension 0.1133112133mm

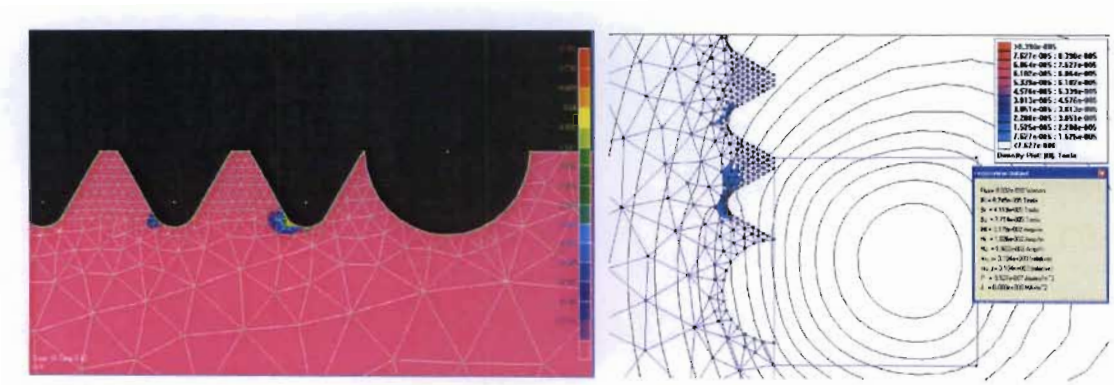

Bolt extension 0.14616mm

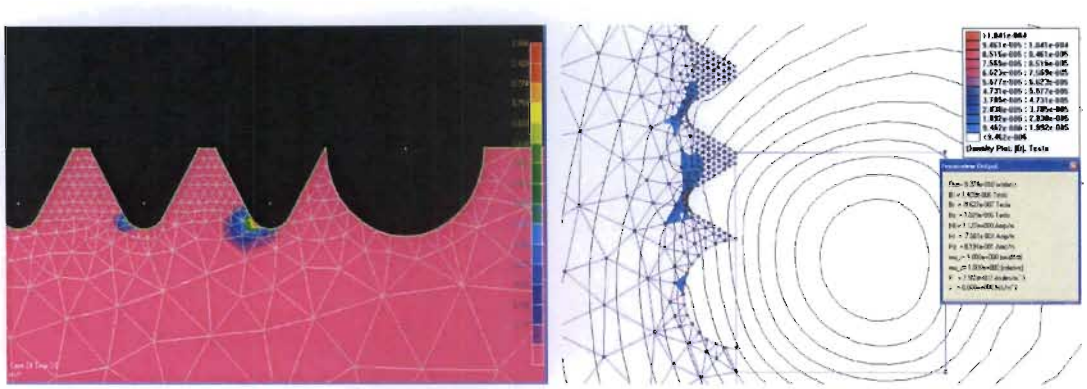

Bolt extension 0.190776mm

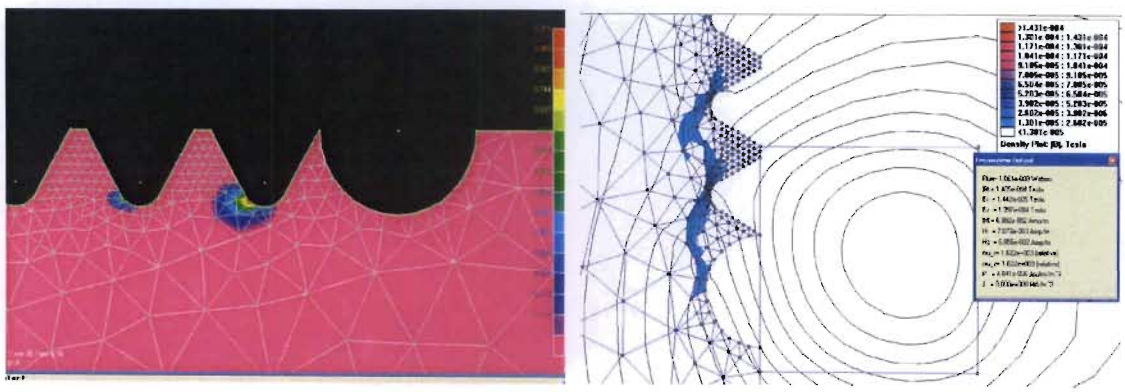

Bolt extension 0.226162mm

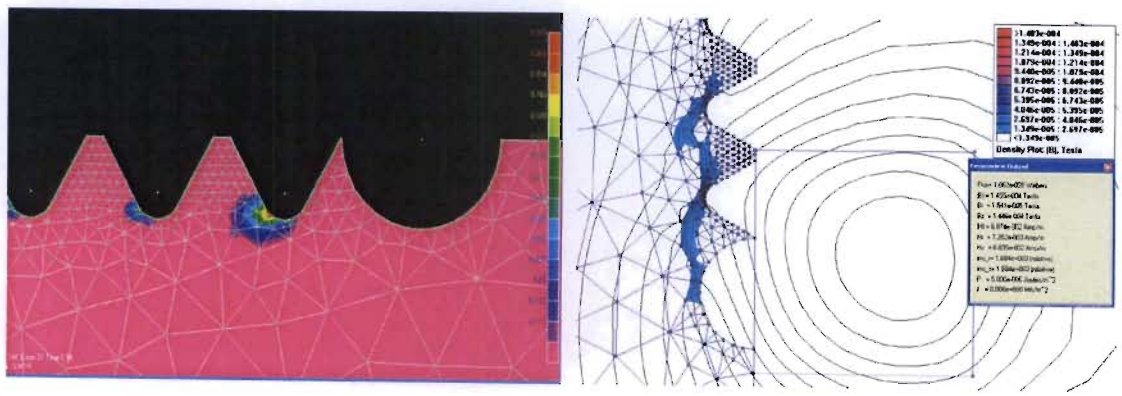

Bolt extension 0.231417mm

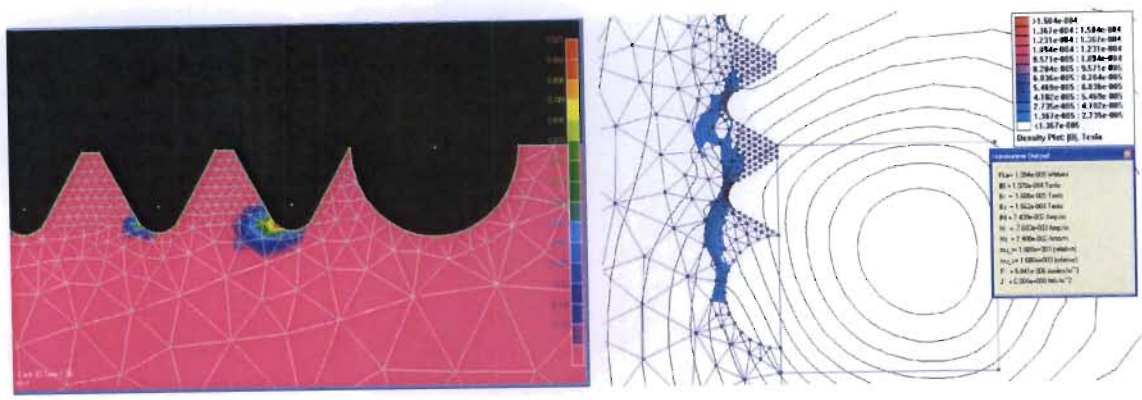

Bolt extension 0.236641mm

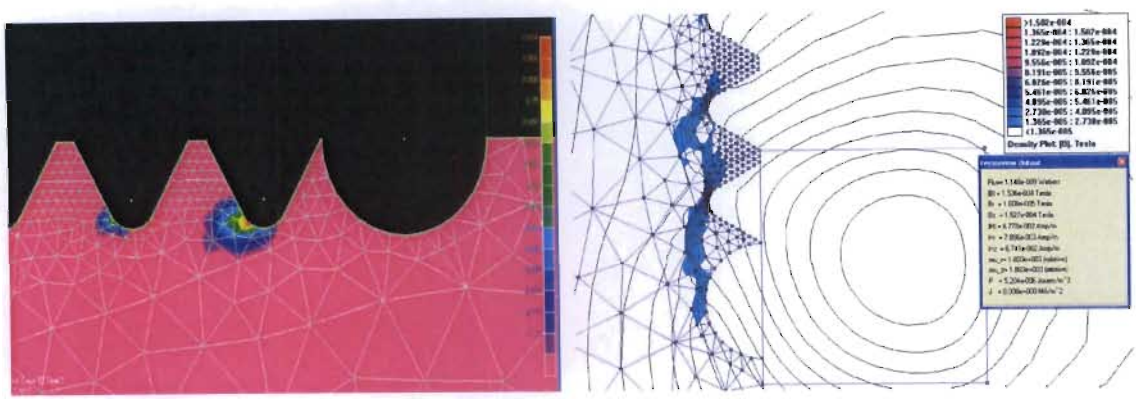

Bolt extension 0.241666mm

Figure 5.12: Incremental increase flux density in regions where there was a substantial increase in martensitic volume fraction, at the top thread(s) root, with respect to increasing bolt extension

5.4 Conclusion

The aim of the technique described here was to provide a platform to correlate the amount of martensite precipitation due to strain-induced transformation resulting from plastic straining of the smart bolt material (strain memory alloy) to the application of an incremental external load. The prediction of the regions where martensite would be precipitated (also the best possible site for smart washer placement) was in agreement with the experimental results.

As stated before, finite element analysis (FEA) and finite element method magnetism (FEMM) provided a highly versatile and flexible means for optimisation and refinement of the geometry of the smart bolt with its mechanical characteristics integrated to the volume fraction of martensite, and the most efficient site(s) for smart washer application for a strain memory alloy (smart bolt) for improved sensing performance of the smart bolt were predicted. The prediction of the mechanical model and corresponding magnetostatic response model for the three quarter diameter inch smart aircraft bolt was carried out in two parts. The first part involved the modelling of the geometry of the smart bolt and the incorporation with a modified version of the Olsen and Cohen response model required to simulate the incremental increase in the volume fraction of martensite as a function of plastic strain resulting from applied external loading. This also provided the locating site of the martensite and sensor application. A nonlinear analysis implemented for the model, as mentioned before, was used to determine the volume fraction of martensite for every loading increment based on the stress-strain physical properties of the MB1 TRIP steel alloy. In the second part, the output mechanical response model containing the geometry, loading condition, material properties and the volume fraction of martensite provided the input model for the magnetostatic response model and was then imported through the use of lua script files in finite element methods magnetism, FEMM. The model was updated for each load increment in order to incorporate the magnetic permeability of The Mintek TRIP steel alloy, i.e., for each loading an equivalent amount of volume fraction of martensite was calculated in any region of the smart bolt.

The results obtained from the mechanical and magnetostatic response models showed that the best site for martensitic strain nucleation to occur was in the vicinity of the top thread(s). The incremental increase in inductance was more pronounced for the smart washer placed over the top thread(s) as was the flux density of the material, with increasing bolt extension.

CHAPTER 6

Conclusion

An evaluation of several candidate TRIP steel alloy to be considered as a material for the manufacturing of smart aircraft bolt, has been presented in this work. Two generations of the four candidate TRIP steel materials were tested for their mechanical properties and ferromagnetic responses characteristics. From the tensile testing data obtained from all four candidate TRIP steel alloys, both generations of all the four alloys displayed unique transformation characteristics with respect to their mechanical properties. However, only alloys 2 and 4 displayed acceptable material properties with respect to yield stress, ultimate tensile strength, and ferromagnetic response, i.e., the change in magnetic susceptibility took place almost immediately upon application of an external load. Although the material selected seemed similar in chemical compositions, the percentage carbon content of alloys 1, 2 and 3 were much less than expected. The carbon element helped stabilize the austenite phase in the alloy parent phase. In fact all four alloys displayed duplex microstructures (confirmed from their metallographic analysis) with small amounts of martesite being present. This made them very slightly magnetic before any external loading was applied.

From the graphs of magnetic susceptibility vs. strain, and stress vs. strain, presented in chapter 4, alloys 2 and 4 displayed a minimal strain-incubation period, i.e., the amount of strain required to begin the martensitic nucleation (and hence a change in magnetic susceptibility) was very small, and occurred long before the yield point of the material was reached. Also it was concluded from the results that alloys 2 and 4 displayed the highest yields strengths and ultimate yield, illustrated in Tables 4.6 and 4.12 of chapter 4. The high degree of yield strength, ultimate strength and very good resolution of magnetictic susceptibility were also confirmed form the data collected from compression testing of TRIP steel alloys 2 and 4. However, upon further testing of alloys 2 and 4 with respect to impact at sub-zero temperatures, the data collected revealed that the fracture toughness of alloys 2 and 4 further increased with decreasing temperature on impact, but alloys 2 proved to be thermodynamically unstable at sub-zero temperature From Figures 4.21 and 4.22 an increase magnetic susceptibility meant the alloy underwent athermal martensitc nucleation, which was attributed to the carbon content required to stabilise the austenite being inadequate. This also meant that at temperatures close to M_s temperature, the transformation kinetics of alloy 2 at sub-zero temperature were affected. The

suitability of alloy 2 was therefore considered somewhat reduced as the thermally induced martensite would be difficult to calibrate out of that produced by strain-induced mechanisms. This however, was not the case for alloy 4: it seemed that alloy 4 displayed no form of thermal martensitc nucleation (figures 4.36 and4.37) and alloy 4 proved to be the most suitable candidate material. The material development phase of the smart bolt development was therefore complete.

The product development phase of this research identified three concepts for a smart prototype bolt that allowed in situ damage monitoring, namely: a bolt with a centre-drilled hole (for probe insertion); a bolt with a groove machined beneath the bolt head, with a smart washer with inductance coil embedded) located over the groove; and thirdly, a bolt with the same smart washer concept, but located over the first few threads of the threaded section. The first concept was discarded early in the product development as difficulties arose with the military specifications, as well as monitoring equipment sensitivities. The concepts utilizing the smart washer were further tested using cyclic temperature testing, fatigue testing, and computer techniques.

The smart washers were found to be the most cost effective and feasible solution for detecting the magnetic signature associated with transformation. No additional circuitry was required for this method apart from "off the shelf" inductance meters required to log the change in inductance of the coils, due to the changing magnetic permeability of their cores (bolts). The experimental data obtained from the tensile testing of the concept smart bolt designs, revealed that the transformation was more substantial at the thread root of the top thread(s) since the change in inductance registered by the smart washer placed over the top thread was far greater than that recorded by the smart washer placed underneath the head of the bolt for either design. The undercut on the shank of the bolt underneath the bolt head served virtually no purpose. Also, for both of the bolt designs, the bolts fractured at the top thread engaged with the locking nut. Furthermore, the metallographic images of the microstructure confirmed strain-induced martensitic nucleation which was magnetically detected by change in inductance recorded from the smart washers.

Considering the operating temperatures range of the aircraft (and therefore the operating range of the bolts under development) a set of cyclic temperature tests was performed to investigate the performance of the smart bolt design concepts. These tests included testing the washer itself, as a means of verifying that no athermal martensite was precipitated within the washer (which was manufactured from 316 stainless steel) as this would interfere with reading from bolts. These tests proved that the washer remained "inert" in terms of magnetic susceptibility

interference. A set of studs manufactured from a material very similar in composition to alloy 2 (denoted M2BR) were also manufactured and cyclic testing performed to determine the performance of the washer interrogation system. The experimental results revealed no change in inductance as measured by the smart washer when no loading was applied and the bolts were cycled between 51.3°C and -47.8°C for 12 hour cycle periods. When a load was applied to the bolts however, a change in inductance was recorded, but this value was constant throughout the temperature cycling regime (which was the same as that for the unloaded condition). A microstructural inspection confirmed that there was no presence of martensite after cycling temperature testing with no external load present, but the small amount of martensite were indeed present after cyclic temperature testing with an external load. From this it is clear the smart washer were indeed effective in detecting martensite correctly at low temperatures. Furthermore, the alloy M2BR was thermodynamically stable across the service temperature range of the aircraft bolt. The strength of this alloy was however as high as that of alloy 2 in compression, which was still therefore the better suited candidate for smart aircraft bolt production.

The tension-tension fatigue testing of the smart stud to failure at a frequency of 4 Hz, illustrated once again the smart washer concepts effectiveness in detecting the change in material inductance, which was a result of the irreversible transformation from austenite to martensite occurring at a microscopic level within the smart stud material's microstructure ahead of a crack initiation. Crack propagation took place at the top thread root engaged to the locking nut as was the case for pure tensile testing. Further proof that the phase transformation had taken place was revealed in the metallographic results that clearly indicated a substantial increase in the amount of martensite nucleation at the slip plane.

The martensite transformation was also modelled within the aircraft bolt geometry and these results predicted what was later found from experimental results to be accurate because the strain-induced transformation is generally inhomogeneous within a component, the volume fraction of martenste precipitated due to transformation was correlated to the plastic load strain for each load increment for mechanical response model. The output model of the mechanical model provided the input model for the magnetostatic model of the aircraft bolt (smart memory alloy). The technique was thus carried out in two parts. In the first part, a half scale axisymmetric geometry of a 19mm diameter smart aircraft bolt was modelled with defined MB1 TRIP steel stress-stain properties (mechanical), incorporated into a modified version of the Olsen and Cohen transformation kinetics model. That was used to simulate and determine the best possible region(s) or site(s) where strain-induced martenste would be precipitated in the smart stud. This was found to be at the top thread root of the stud engaged to the nut top

thread(s). The resultant mechanical response model determined was then imported to the Finite Element Methods Magnetism, FEMM, as a base input geometric model containing all the martensite parameters for each loading conditions (load increments), with the material properties of MB1 TRIP steel for the second part of the analysis; this being the magnetostatic response model of the smart aircraft bolt model determined from the mechanical response model. The magnetostatic response modelling was carried out purely to predict the change and strength of inductance by calculating and evaluating the current and field strength in the coils of the smart washers.

The results obtained from the mechanical and magnetostatic response models simulations showed that the best site for smart washer placement was over the top thread(s) engaged with the locking nut, because the change in inductance calculated for the smart washer coil block integral for each load increment (bolt extensions) corresponding to the amount of transformed material was more substantial than that calculated for the smart washer coil placed underneath the bolt head illustrated in Figures 5.10 and 5.11, which was expected since the top thread(s) experience the highest stress level because they carry roughly 80% of the bulk load. These results also showed that the smart washer concept worked well and that the result obtained from the tensile testing of the two sub-scaled smart bolts and the smart stud tested for both cyclic temperature and fatigue verified that the smart washer was an easily implementable solution for measuring the inductance change of the smart aircraft bolt. Also from the mechanical and magnetostatic response model simulations, tensile testing of the sub-scaled bolts and the fatigue and cyclic temperature analysis proved that the best possible site for smart washer location was over the top thread(s) engaged with that of the locking nut. In addition the smart washer concept proved that the magnetic signature (change in inductance or magnetic susceptibility) of smart bolts or smart studs was dependant on the volume fraction of martensite present within the TRIP steel aircraft bolts or studs and thus the changes in transformation directly influenced by progressively increasing induced-strain. Also, because of the great versatility and flexibility of FEA and FEMM, it allowed the smart bolt to be optimised with respect to the mechanical and magnetostatic response modelling, which resulted in to the bolt geometry remaining very similar to that specified by the current SPS –B-640 military standards for aircraft bolt geometry

The smart bolt (strain memory alloy) and smart washer concept offer a relatively inexpensive cost effective data acquisition platform upon which the interrogation of the smart bolt system in service would be straight forward and with a high degree of accuracy in real time monitoring and recording data, thereby reducing maintenance cost that might be associated with scheduled inspection. No expensive data acquisition and storage systems are required for detection and monitoring the service life of the smart bolt. This kind of benefit would help reduce the routine

200 man-hours required for the periodic inspection of the C130 wing bolts. In order for the smart aircraft bolt assembly to gain military certification (and subsequent implementation into the commercial market) full size bolts will be need to manufactured and tested in military laboratories in variable amplitude fatigue tests, using the program that military materials laboratories have for simulating the flight loading spectrum. From these tests it will be possible to calibrate an inspection period and an inductance level at which bolts should be replaced.

REFERENCES

1. V Verijenko, and B Burton, " Smart Materials for Structural Health Monitoring" ESDA, July 2002, Istanbul, Turkey
2. F Lecroisey and A Pineau, "Martensitic Transformation Induced by Plastic Deformation in the Fe-Ni-Cr- C System", Metallurgical Transactions, Vol. 3, pp 387-396. February 1972.
3. G R Chanani, S D Antolovich, and W W Gerberich, "Fatigue Crack Propagation in TRIP steel", Metallurgical Transaction, vol. 3, pp 2661-2672, 1972.
4. A Hall James, V F Zackay and R E Parker, "Structural Observation in a MetasTable Austenitic Steel", Transactions of the ASM, vol. 62 , pp. 965-976, 1969.
5. D Webster, "Development of a high strength stainless steel with improved toughness and ductility", Metallurgical Transactions, vol. 2 pp 2097-2104, 1971.
6. G R Chanani, and S D Antolovich, "Low cycle fatigue of High Strenght metasTable Austenitic steels", Metallurgical Transactions, pp 217-229, 1974.
7. P C Maxwel, A Goldberg, and J C Shyne, "Stress-Assisted and Strain-Induced Martensites in FE-NI-C Alloy", Metallurgical Transactions, vol. 5, pp 1305-1318, 1974.
8. J R C Guimarares, and R J De Angelis, Stress-Strain Relationship during Transformation Enchanced Plasticity", Metallurgical Transactions, vol. 4, pp 2379-2381, 1973.
9. U Krupp, P Luezuo, R G Teteruk, and H J Christ, "Deformation-induced Martensite Formation in MetasTable Austenitic Steel in Dependence on the Carbon Content", Institut fur Werkstofftechnik, Universitat Siegen Fed. Rep. Germany, 2002.
10. F A Grossley and R W Lindberg, "Microstructure Analysis of a High Strength Martensite-Beta Titanium Alloy", Metallurgical transactions vol.13, pp. 841-883, 1970.
11. F Abrassart, F Lecroisey, A Pineau, "Martensitic Transformation and Plasticity in the Fe-Ni-Cr-C System", Metallurgical Transaction, vol. 16, pp-905-909, 1970.
12. G B Olson and M Cohen, "Kinetics of strain-induced Martensitic Nucleation", Metallurgical Transactions A, vol 6A, pp 791-795, April 1975.
13. R G Stringfellow, D M Parks and G B Olson, "A Constitutive Model for Transformed Plasticity Accompanying Strain- Induced Martensitic Transformation in MetasTable Austenitic Steels", Acta Metallurgica, vol.40, 7, pp 1703-1716, 1992.

14. V I Leivitas, A Idesman and G B Olson, "Continuum Modeling of Strain-Induced Martensitic Transformation at Shear-band Intersections", Acta Metallurgica, vol.47, 1, pp 219-233, 1999.
15. W B Morrison, " Plastic Instability During Luders Deformation in Ultrafine-Grained Low- Carbon Ferritic Steel", Transaction of the ASM, pp.879-893, 1970,
16. J S Dunning, and L D Thomson. "Development of Smart Solid-State Structural Damage Assessment Systems for Underground Facilities", North-American conference on smart structures and materials, San Diego 1995
17. G B Olson, and M Azrin, "Transformation Behavior of TRIP Steels", Metallurgical Transactions, Vol. 9A, pp 713-721, 1978.
18. E H R Wade and C M Preece, "Cavitation Erosion of Iron and Steel", Met. Trans.A., vol 9A, pp 1299-1309, 1978.
19. E Arnold, "Steels: Microstructures and Properties", Metallurgy and Materials Science Series, R W K Honeycomb, pp 55-56, 1981.
20. W F Smith, "Structure and Properties of Engineering Alloys", McGraw-Hill, New York, 1993
21. A G Pineau, and R M Pelloux, "Influence of Strain-Induced Martensite Transformation on Fatigue Crack Growth Rates in Stainless Steels", Metallurgical Transactions, vol. 5, pp1103-1112, 1974.
22. E R Parker and V F Zackay, "Enhancement of Fracture Toughness in High Strength Steel by Microstructural Control", Engineering fracture mechanics, Vol.5, pp 147-165, 1973.
23. W Gerberich, P L Hemmings, and V F Zackay, 'Fracture and Fractography of MetasTable Austenites", Metallurgical Transactions, vol.2 August,pp 2243-2253, 1971.
24. V F Zackay, D Bhandarkar, and E R Parker, "The Role of Deformation-Induced Phase Transformation in the Plasticity of Some Iron-Base Alloys", Metallurgical Transactions, vol. 3, pp 2619-2631, 1972.
25. Y Tomita, and Y Shibutani, "Estimation of deformation behavior of TRIP Steels", International journal of Plasticity 16 (2000), pp.769-789.
26. F Abrassart, Metallurgical Transactions, vol. 4, pp 2205-2216, 1973.
27. C J Guntner and R P Reed, "The Effect of Experimental Variables Including the Martensitic Transformation on the Low-Temperature Mechanical Properties of Austenitic Stainless Steels", Transactions of ASM, Vol.55, pp.399-419, 1962.
28. Tamura, T Maki, H Hato, Y Tomota and M Okada, "Strength and Ductility of Austenitic Iron Alloys Accompanying Strain- Induced Martensitic Transformation", transaction of the ASM, pp 900-904, 1970.

29. D Goodchild, W T Roberts and D V Wilson, "Plastic Deformation and Phase Transformation in Textured Austenitic Stainless Steel", Acta Metallurgical, vol.18, November pp1137-1144, 1970.
30. J M Drapier, P Viatour, D Contsanradis, and L Habraken, "Hardening Mechanism in Multiphase Alloys", Paper 11.4, PP 830-834, 1970.
31. R D Knutsen, and M Sbanda, " Evaluation of the Formability Properties of Nitrogen Alloyed MeetasTable Austenitic Stainless Steels", Proceedings of Stainless Steels, 93 Processes and Material Innovation, vol. 3, Florence, AIM, pp 3.333-3.342, 1993.
32. T Biggs, and R D Knutsen, Journal de Physique 4, vol. 5, pp C8-515- C8-520, 1995.
33. M Sibanda, S L Vismer, and R D Knutsen, Materials Letters 21, pp 203-207, 1994.
34. R Paton, J S Moema, C J Fletcher and D Adams, "The Use of Smart Bolt Technology to Assess the Condition of Mining Roof Support Systems", 6th International Colloquium, Ageing of Materials and Methods for the Assessment and Extension of Lifetime of Engineering Plant. Cape 2001
35. D S Clark and W R Varney, "Physical Metallurgy for Engineers", New York 1962
36. E W Pages, P Mangamon, G Thomas and V F Zackay, "Structure and Dynamically Strain Aged Fe-Cr-C and Fe-Mo-C Alloys", Transactions of the ASM vol.62, pp 45-54, 1969
37. D J Drobujak, and J G Parr, Metallurgical Transactions, vol. 1 pp 759-765, 1970.
38. T Angel, Journal of the Iron and Steel Institute, pp165-174, May 1954.
39. J Lefevre, R Tricot, A Gueussier, and R Castro, Metallurgical Transactions, vol. 5, pp 2277-2285, 1974.
40. D A Woodford, " Cavitations Erosion-Induced Phase", Metallurgical Transactions, Vol 3, pp 1137-1145, May 1972
41. S O Walter, "Strengthening by Transformation", Transaction of the ASM, pp. 795-814, 1970.
42. W W Gerberich, G. Thomas, E. R. Parker and V F Zackay, "MetasTable Austenite Decomposition and Strength", Paper 13.6, pp 894-899, 1970.
43. J C Shyne, V F Zackay, and D J Schamtz, Transactions of the ASM, vol. 52, pp 347-361, 1960.
44. G Thomas, D Schmatz, and W Gerberich, "Structure and Strength of some Ausformed Steels", MT-74, pp 251-296, 1964.
45. T J Koppenaal, Metallurgical Transactions, vol. 3, pp 1549-1554, 1972.
46. G R Chanani, V F Zachay, and E R Parker, Metallurgical Transactions, vol.2, pp 133-139, 1971.

47. G F Bolling and R H Richman, "The Plastic Deformation – Transformation of Paramagnetic FCC. F-Ni-C Alloys", Acta Metallurgica, vol.18, pp 673-681, June 1970.
48. R G Davies and C L Magee, "On the Occurrence of the Various Martensite Morphologies", paper 11.2, pp 817-821, 1970.
49. C Altstetter and M Rashid, "Defects and Strengthening in Transformed Crystals", paper 11.7, pp 846-849, 1970.
50. H Smith and D R F West, "The Strengthening of Stainless Steels by the Reverse Martensite Transformation", paper 13.5, pp 892-893, 1970.
51. V F Zackay, E R Parker, D Farh, and R Bush, Trans. ASM, vol. 60, pp 252, 1967.
52. B L Verijenko, " Smart Materials for Structural Health Monitoring", PhD Thesis, University of Natal, Durban, January 2003
53. G Krauss, and M Cohen, Trans. TMS-AIME, vol. 224, pp 1212, 1962.
54. G Krauss, Acta Metallurgica, vol.11, pp 499, 1963.
55. D Fahr, "Stress and Strain- Induced Formation of Martensite and it Effect on Strength and Ductility of MetasTable Austenitic Steels", Metallurgical Transactions, Vol. 2, July pp 1883-1892, 1971.
56. V F Zackay and E R Parker, "Some Fundamental considerations in Design of High-Strength Metallic Material", High Strength Design, pp130-153, 1964.
57. A R Marder and G Krauss, "The Effect of Morphology on the Strength of Lath Martensite", paper 11.2, pp-822-829, 1970.
58. D P Roberts, "Testing of Mining Tunnel support Elements and Systems for Hard Rock Mines", M Sc. Thesis, University of Natal, 1995.
59. B G Orson, M Azrin, and H E Band, "AC-permeability measurement of strain-induced martensite during tensile deformation of TRIP steels", AMMRC TR 77-10, Massachusetts, March 1977.
60. L D Thompson, "The FCC to HCP to BCC phase transformation sequence in metasTable Fe-Mn-Cr alloy", Department of Mechanical Engineering San Diego State University, CA 92182-0191.
61. Mr J M Vugampore, "Development of High Strength Material for Smart Aircraft a Bolt", University of Natal, Ph.D. Thesis, October 2005.
62. C Shakeri, M Noori, and Z Hou, "Smart material and structures. A review." Tech. Report of Worcester Polytechnic Institute, 1998.
63. G Mook, J Phol, F Michel, and T Benziger, "Damage Evaluation of Smart CFRP-Piezoelectric Materials Using Non-destructive Methods". Proceeding of the 12th International Conference on Composite Materials, Paris, 1999.
64. B Cina: transitional HCP. Phase in Fe-base alloys: Acta Metallurgica, vol. 6 1958.

65. P C De Vera, and G Guemes, "Embedded Self-sensing Piezoelectric for Damage Detection." J. International Systems and Structures 11, 1999.
66. M Azrin, G B Olson and R A Gagne, "Inhomogeneous Deformation and Strain Rate Effects in High-Strength TRIP Steels", Materials Science and Engineering, vol.23, pp 33-41, 1976.
67. E Gold and T J Koppenaal, "Anomalous Ductility of TRIP Steel", Transactions of the ASM, Vol.62, pp 607- 610, 1969.
68. G W Form and W M Baldwin, "The Influence of Temperature on the Ductility of Austenitic Stainless Steel", Transactions of the ASM, vol. 48, pp 474-485, 1956.
69. R A Lincoln and W H Mather, "Effect of Temperature on Cold Rolling, Temperature of Testing and Rate of Pulling on Tensile Properties of Austenitic Stainless Steels with Low Nickel Content", Regional Technical Meeting, Iron and steel Inst. 57, 1948
70. V N Krivobok and A M Jalbot, "Effect of Temperature on the Mechanical Properties, Characteristics, and Processing of Austenitic Stainless Steel", Proc ASTM, 50, P 895, 1950.
71. J F Waston and J L Christian, "A Study of Austenite Decomposition at Cryogenic Temperature", Transactions AIME, 224, p 998, 1962.
72. K M Carlsen and K C Thomas, "Effect of Composition, Heat Treatment and Cold Rolling on Mechanical Properties of Cr-Ni Stainless Steels", Transactions Quart, 55, pp 462, 1962.
73. G W Powell, E R Marshal and W A Backofen, "Strain Hardening of Austenitic Stainless Steels", Transaction ASM,50, p 478, 1958
74. J F Breedis and W D Roberton, "The Martensitic Transformation in Single Cristals of Iron-Chromium-Nickel Alloys", Acta Metallurgica, 10, p 1077, 1962.
75. J P Bressanelli and A Moskowitz, "Effect of Strain Rate, Temperature, and Composition on Tensile Properties of MetasTable Austenitic Stainless Steel, Transactions of the ASM, volume59, pp 223-235, 1966.
76. D Hennessy, G Steckel and C Alstetter, "Phase Transformation of Stainless Steel during Fatigue", Metallurgical Transactions, Vol.7A, March 1976, pp 415-424.
77. D Jonson "Finite Element Modelling of Smart TRIP Steel Sensors and Systems", University of Natal, Ph.D. Thesis, January 2003.
78. Smart Aircraft Bolt Technology project 1999/2000, School of Mechanical Engineering, University of Natal. Prepared for ARMSCOR.
79. D P Rowlands, "The Secrets of Stainless Steels", SA Stainless Steel Development Association (SASSDA), Stainless Steel Information Series No.18.

80. L D Thompson, B Westermo and M Tominaga, "Monitoring Based Maintenance for Civil Engineering Structures", International conference on structural safety and reliability, Newport Beach, June 2001.

81. V Zackay, E Parker, D Fahr and R Bush, "The Enhancement of Ductility in High-Strength Steels", Transaction of ASM, 60, pp 252-259, 1967.

82. G B Olson, R Chair, M Azrin and R A Gagne, "Fatigue Strength of TRIP Steel", Met. Trans., 11A, pp. 1069-1071, 1980.

83. V F Zakay, M D Bhandarkar, and E R Parker, " The Role of Deformation-Induced phase Transformation in the Plasticity of some Iron Base Alloys", Metallurgical Transactions, vol. 41, pp. 351-403, 1978.

84. D Stephen Antonovich and D Fahr, "An Expermental Investigation of the Fracture Characteristics of TRIP Alloys", Engineering Fracture Mechanics, vol. 4, pp 133-144, 1972.

85. G R Chanani, D Stephen Antolovich and W W Gerberich, " Fatigue Crack propagation In TRIP Steels", Metallurgical Transactions, vol. 3 1972.

86. D Stephen Antolovich and Birindar Singh, "On the Toughness Increment Associated with the Austenite to Martensite Phase Transformation In Trip Steels", vol. 2, pp 2135-2136, 1971.

87. G E Forsythe and W R wasow, "Finite Difference Method for Partial Differential Equations", John Wiley and Sons, New York, 1960.

88. R D Richtmeyer and KW Morton, " Difference Methods For Initial-Value Problems, 2nd Edition", Wiley-Interscience, New York, 1967.

89. J T Oden and J N Reddy, "An Introduction to the Mathematic of Finite Elements", John Wiley and Sons, New York, 1976.

90. F B Hildebrand, "Methods of Applied Mathematics", Prentice-Hall, Englewood Cliffs, New Jersey, 1965.

91. O C Zienkiewicz, "The Finite Element Method, 3rd edition", McGraw-hill Book Company, New York, 1977.

92. C A Felippa and R W Clough, "The Finite Element Method in solid Mechanics", SIAM-AMS Proceedings, vol 2, American Mathematical Society, Providence, R I, pp 210-252, 1970.

93. S S Rao, "The Finite Element Methods in Engineering", 3rd edition, pp 12, pp69-89, pp247-254, 1999.

94. J N Reddy, "An Introduction to The Finite Element methods, 3rd edition, McGraw-Hill Book INT edition, pp97, 2006.

95. J S Dunning and L D Thompson, "Development of Smart Solid Structural Damage Assessment Systems foe Underground facilities", Proc.1995 North American Conf. On Smart Structures And Materials, San Diego, CA, March 1995.
96. L D Thompson and B D westermo, "Development of Smart Structure Attachment fixtures", Proc.19996 North American Conf. On Smart Structures And Materials, San Diego, CA, March 1996.
97. D A lowther, E M Freeman, and B Forghani, "A sparse Matrix Open Boundary for Finite Element Analysis", I EEE Transaction on Magnetics, 25 (4), pp 2810-2812, July 1989.
98. E M Freeman and D A lowther, "Open Boundary Techniques for Axisymmetric and three Dimension Magnetic and Electric Field Problems", I EEE Transaction on Magnetics, 25 (5), pp 4135-4137, September 1989.
99. G Thomas, "Electron Microscopy Investigation of Ferrous Martensites. Met. Trans, 2, 2373, I971.
100. D. Meeker, "Finite Element Methods Magnetics", pp 6-9, pp58-74, 2002.
101. G B olson and M Cohen, "Kinetics of Strain-Induced Martensite Nucleation", Metallurgical Transactions, vol. 6A 1975.
102. L Kuafman and M Cohen, "Thermodynamic and Kinetics of Martensite Transformation", Prog in Metal Physics, 7, 165, 1958.
103. J A vanables ,' Phil. Mag, 7, 35, 1964.
104. Y Tomita and T iwamoto, "investigateion on Deformation mode dependence of Strain-Induced Martensitic Transformation in TRIP steels and Modelling of Transformation kinetics', Int J Mech. Sci, 40 173,1998.
105. R W K Honeycombe, "Steel Microstructures and Properties", Edward Arnold, London, 1981.
106. R C Juvinall and K M Marshek, "Fundamentals of Machine Componet Design", 3rd Ed, pp 311- 322, 411-413, 427-451, 2000
107. L D Thompson and B Westermo, "Application of a New Solid-State Structural Health Monitoring Technology", Proc. 2nd, European Conference on Smart Structures and Material, Glasgow, Scotland, October 1994.
108. L D Thompson and B Westermo, "Design and Evaluation of Passive and Active Structural Health Monitoring Systems for Bridges and Buildings", Proc.1995 North American Conf. On Smart Structures And Materials, San Diego, CA, March 1995.
109. T H H Pian and P Tong, "Basis of Finite Element Methods for Solid Continua", INT j Numer. Method Eng, 1, p 26, 1969.
110. R D Cook, D S Malkus and R J Witt, " Concept nad Application Of Finite Element Analysis", 4th Edition, pp 83-84,2002.

APPENDIX

Appendix: A

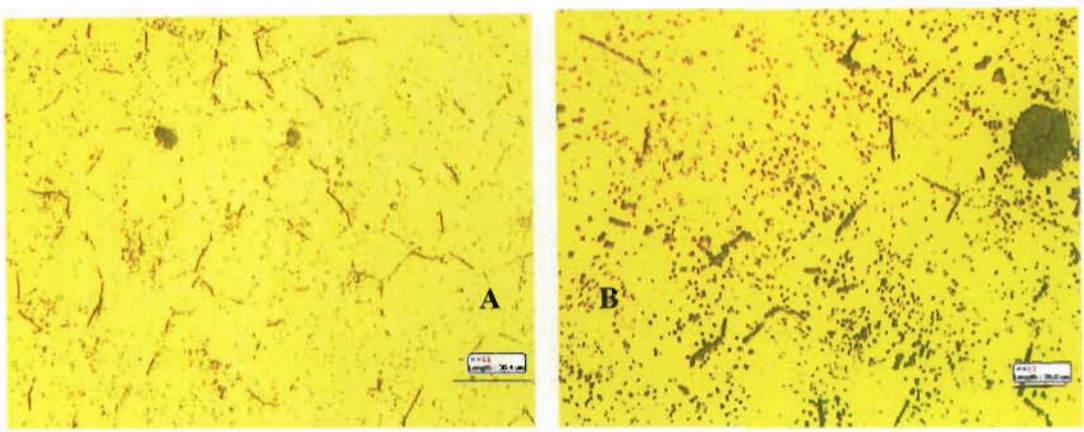

Figure 1: **Shows the microstructure of the Mintek TRIP steel alloy tensile tested to stress level of 0MPa and 70MPa, represented in pictures A and B respectively**

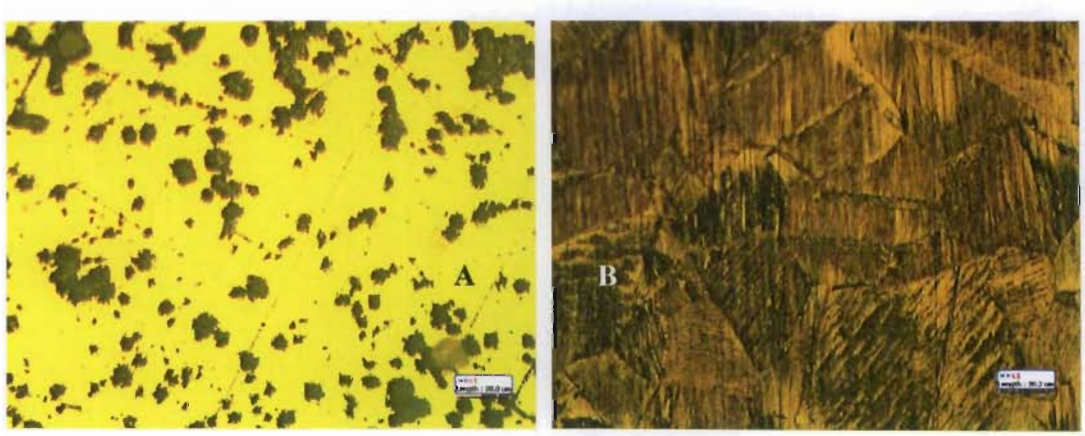

Figure 2: **Shows the microstructure of the Mintek TRIP steel alloy tensile tested to stress level of 140MPa and 210MPa, represented in pictures a and b respectively**

Figure 3: **Microstructure of the MB1 TRIP steel alloy tensile tested to stress level of 280MPa and 350MPa, represented in pictures A and B respectively**

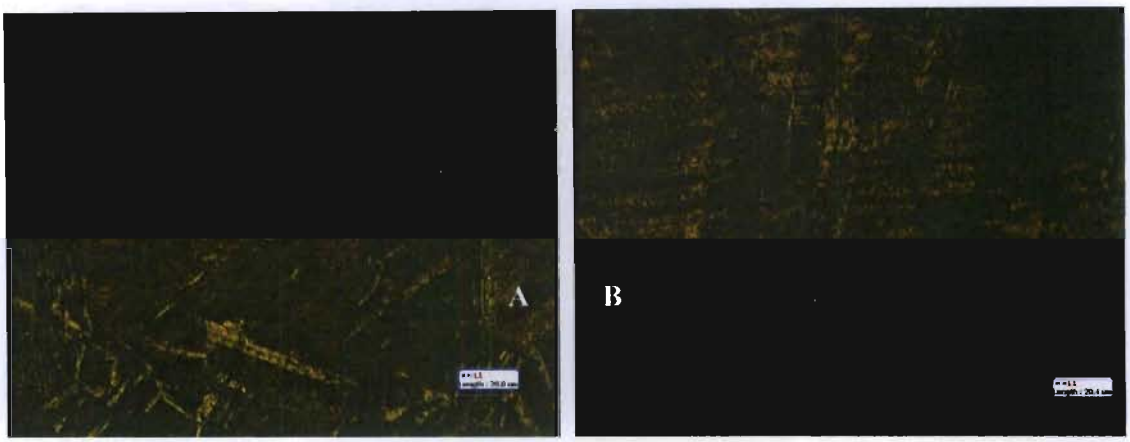

Figure 4: **Microstructure of the MB1 TRIP steel alloy tensile tested to stress level of 420MPa and 490MPa, represented in pictures A and B respectively**

Figure 5: **Microstructure of the MB1 TRIP steel alloy tensile tested to stress level of 560MPa and 618.08MPa, represented in pictures A and B respectively**

Appendix B:

The Below shows the % martenstic derived from the microscopic structures of the tensile specimen loaded at different stress of the Mintek TRIP steel alloy.

0 MPA	Phase 1: 0 - 1338	Area	Total Area	Martensite	Martensite
	μm²	%	μm²	% fraction	fraction
	11276.43	3.63	310282.14	3.63425	0.0363425
70.00721MPA	Phase 1: 0 - 951	Area	Total Area	Martensite	Martensite
	μm²	%	μm²	% fraction	fraction
	4223.12	6.25	67569.94	6.25	0.0625
139.9503 MPA	Phase 1: 0 - 1459	Area	Total Area	Martensite	Martensite
	μm²	%	μm²	% fraction	fraction
	31006.53	7.54	411379.91	7.5372	0.075372
209.8014 MPA	Phase 1: 0 - 500	Area	Total Area	Martensite	Martensite
	μm²	%	μm²	% fraction	fraction
	3817.94	8.80	43386.51	8.8	0.0879984
279.9321MPA	Phase 1: 0 - 846	Area	Total Area	Martensite	Martensite
	μm²	%	μm²	% fraction	fraction
	28809.46	37.97	75879.56	37.96735	0.3796735
349.5641MPA	Phase 1: 0 - 749	Area	Total Area	Martensite	Martensite
	μm²	%	μm²	% fraction	fraction
	38395.60	64.84	59216.67	64.83917	0.6483917
420.0098 MPA	Phase 1: 0 - 741	Area	Total Area	Martensite	Martensite
	μm²	%	μm²	% fraction	fraction
	39305.37	88.90	44213.08	88.89987	0.8889987
489.8825 MPA	Phase 1: 0 - 1410	Area	Total Area	Martensite	Martensite
	μm²	%	μm²	% fraction	fraction
	47034.41	93.32	50399.17	93.32379	0.9332379
559.7713MPA	Phase 1: 0 - 1289	Area	Total Area	Martensite	Martensite
	μm²	%	μm²	% fraction	fraction
	46692.23	94.64	49336.57	94.6402	0.946402
618.0873 MPA	Phase 1: 0 - 1306	Area	Total Area	Martensite	Martensite
	μm²	%	μm²	% fraction	fraction
	59393.13	96.20	61736.50	96.20424	0.9620424

Appendix C

SCROOBY'S LABORATORY SERVICE cc

Spectrographic and Chemical Analysis of Materials

CK 1999/047204/23
21 O'Reilly Merry St
Rynfield Benoni 1501
V.A.T Reg. No: 4390188391

TEL: (011) 425-1074
FAX: (011) 849-3571
CELL: 082-675-4536

P O Box 13401
Northmead
1511

University of Kwazulu - Natal
School of Mechanical Engineering
Private Bag X 54001
DURBAN
4041

17 August 2006

ATTENTION: Ms Oona Chetty

CERTIFICATE of ANALYSIS REFERENCE No: 5591 / 1

	Sample ID - Composition in Mass %			
ELEMENT	A1 Core	A1 Outer	A2 Core	A2 Outer
Carbon	0.22	0.099	0.27	0.12
Manganese	3.13	2.92	1.19	1.20
Sulphur	0.013	0.015	0.007	0.009
Phosphorus	0.016	0.011	0.011	0.013
Silicon	0.62	0.78	0.61	0.62
Chromium	8.34	7.91	12.0	12.3
Molybdenum	2.23	2.49	≤ 0.01	≤ 0.01
Nickel	9.40	9.72	10.3	10.2
Copper	≤ 0.01	≤ 0.01	≤ 0.01	≤ 0.01
Aluminium	0.011	0.033	≤ 0.01	≤ 0.01
Vanadium	0.018	≤ 0.005	≤ 0.005	≤ 0.005
Niobium	0.023	≤ 0.005	0.017	0.019
Boron	≤ 0.005	≤ 0.005	≤ 0.005	≤ 0.005
Titanium	0.010	≤ 0.005	≤ 0.005	≤ 0.005
Iron	Matrix	Matrix	Matrix	Matrix

Description of Sample's

Flat sections identified above

Original Certificate Signed J V Scrooby

Laboratory Manager

Appendix D

SCROOBY'S LABORATORY SERVICE cc

Spectrographic and Chemical Analysis of Materials

CK 1999/047204/23
21 O'Reilly Merry St
Rynfield Benoni 1501
V.A.T Reg. No: 4390188591

TEL: (011) 425 1074
FAX: (011) 849 3871
CELL: 082 678 4536

P O Box 13401
Northmead
1511

University of Kwazulu - Natal
School of Mechanical Engineering
Private Bag X 54001
DURBAN
4041

17 August 2000

ATTENTION: Ms Ooma Chetty

CERTIFICATE of ANALYSIS REFERENCE No: 5591 / 2

Sample ID - Composition in Mass %

ELEMENT	Ki BR	M2 BR
Carbon	0.31	0.32
Manganese	4.09	4.09
Sulphur	≤ 0.005	≤ 0.005
Phosphorus	≤ 0.005	≤ 0.005
Silicon	0.34	0.61
Chromium	8.45	8.41
Molybdenum	≤ 0.01	≤ 0.01
Nickel	8.30	8.40
Copper	≤ 0.01	≤ 0.01
Aluminium	0.024	0.026
Vanadium	0.010	0.011
Niobium	0.021	0.021
Boron	≤ 0.005	≤ 0.005
Titanium	≤ 0.005	≤ 0.005
Iron	Matrix	Matrix

Description of Sample's
Round bar sections
Ki BR – 28.25mm Ø
M2 BR – 23.20mm Ø

Original Certificate Signed J V Scrooby

Laboratory Manager

All information in this document is given in good faith, but without warranty or guarantee of any kind whatsoever, whether implied or expressed
Samples will be retained for three months

Appendix E

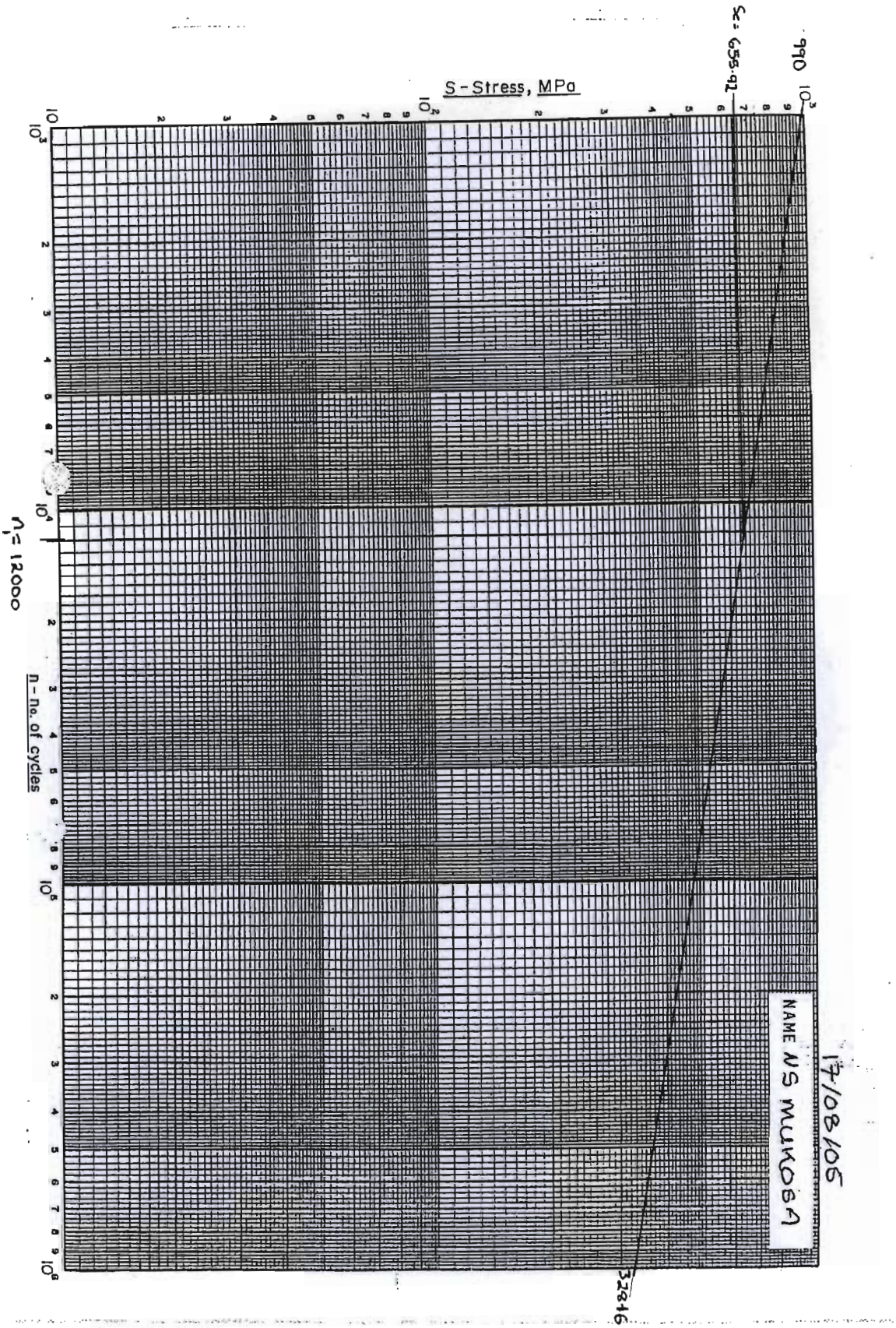
S - Stress, MPa
n - no. of cycles
Sc = 655.92
n1 = 12000
990
32846
17/08/05
NAME NS MUKOSA